



Cape Peninsula  
University of Technology

# **CFD MODELLING OF THE PERFORMANCE OF VARIOUS WIND TURBINE ROTORS WITH EXPERIMENTAL VERIFICATION**

by

**Daniel Rudolph Barnard**

**Thesis submitted in fulfilment of the requirements for the degree**

**Master of Engineering: Mechanical Engineering**

**In the Faculty of Engineering & the Built Environment**

**at the Cape Peninsula University of Technology**

**Supervisor:** Professor G. Oliver

**Co-Supervisor:** Mr. H. Fawkes

**Bellville**

7 September 2021

## **CPUT Copyright Information**

The dissertation/thesis may not be published either in part (in scholarly, scientific or technical journals), or as a whole (as a monograph), unless permission has been obtained from the University

## Declaration

I, Daniel Rudolph Barnard, declare that the contents of this thesis represent my own unaided work, and that the thesis has not previously been submitted for academic examination towards any qualification. Furthermore, it represents my own opinions and not necessarily those of the Cape Peninsula University of Technology.

Signed

A handwritten signature in black ink, appearing to read 'Daniel Barnard', written over a horizontal line.

Date

7 September 2021.

# Abstract

The Blade Element Momentum Method (BEMM) is often used in the initial design of horizontal axis wind turbine (HAWT) rotors. The BEMM has many simplifying assumptions and limitations, therefore simulation and testing are essential for a successful design. Climate change concerns and the depletion of fossil fuels have created a global imperative for increased use of renewable energy. An important source of renewable energy is wind which is mostly harvested by means of large HAWTs.

This research was focussed on performance comparison of two, almost identical, small HAWT rotors. The first rotor was designed using the conventional BEMM. The second was designed using an adapted BEMM which is currently under research at Cape Peninsula University of Technology (CPUT). A particular area of interest was the performance of HAWT rotors at low (off-design) wind speeds. Performance comparison of these two rotors by simulation and physical testing at half the design wind speed was the central objective of this research.

Research included the creation of solid models for Computational Fluid Dynamics (CFD) simulation and manufacturing of the conventional and Adapted (ADP) rotors for physical testing. The vehicle-top mounted test rig and instrumentation were built for physical testing to capture the power output of the rotors. Flow through the rotors and rotor power output were analysed using ANSYS Fluent software. CFD simulation results and physical test result were interpreted and compared. Procedures for the solid modelling and the CFD analysis formed part of the output of this research.

Simulation predicted a 1.06 % increase and physical test results revealed a 6.06 % increase of peak performance for the ADP rotor. Physical results had lower power output than the simulation results due to losses present during field testing. The power output and power coefficient curves of the simulation and field test were compared for each rotor. An unexpected outcome from physical test results was that the ADP rotor power peak occurred at a significantly higher rotational speed than the power peak of the standard (STD) rotor due to the ADP rotor's design change. The field tests produced lower measured power output compared to the CFD predicted power output which was likely due to the oversized generator. Although we were not able to accurately measure the absolute power, we were still able to make use of the relative electrical power output to make the comparison between the ADP and Standard (STD) rotor characteristics.

Simulation and physical results confirmed that the ADP rotor outperformed the STD rotor at peak performance rotational speed. It is recommended that the ADP design approach be considered for rotors that have a hub ratio in the region of 20 %. Further recommendations

were also made for solid modelling, simulation, the vehicle-top mounted test rig and aspects of the methodology.

# Acknowledgements

## I wish to thank:

- Howard Fawkes my supervisor for imparting all the knowledge and assistance.
- Prof Graeme Oliver for all the help and guidance.
- All technical colleagues at CPUT who allowed me to use their workspace.
- Technical staff at Qfinsoft;
- Anvo and Estelle for driving during field testing; and
- My wife, Mirka Barnard for helping all the way.

# Contents

Declaration	ii
Abstract	iii
Acknowledgements	iv
List of figures	vii
List of tables	x
Glossary of terms	xi
Nomenclature	xii
List of symbols	xiv
List of Greek Symbols	xvi
<b>1. Chapter One: Introduction</b>	<b>1</b>
1.1 Renewable resources on earth	1
1.2 Motivation for this work	2
1.3 Research objectives	3
1.3.1 CAD modelling	3
1.3.2 ANSYS Fluent simulation	3
1.3.3 Manufacturing of the rotors	3
1.3.4 Physical testing of the rotors	3
1.4 Outputs	4
1.5 Research design and methodology	4
1.6 Scope of work	4
<b>2. Chapter Two: Literature Review and Theoretical Background</b>	<b>5</b>
2.1 Wind energy	5
2.2 Rotor blade design considerations	8
2.2.1 HAWT blade design software	11
2.3 Blade element momentum method	11
2.4 Solid modelling	15
2.5 Numerical simulation for CFD	16
2.5.1 Fundamental equations	17
2.5.2 Turbulence model	18
2.5.3 Simulation blockage factor	20
2.5.4 Boundary layer	20
2.5.5 Meshing	22
2.6 Physical testing	23

2.6.1	Blade manufacturing.....	23
2.6.2	Testing options.....	23
2.6.3	Instrumentation.....	26
<b>3.</b>	<b>Chapter Three: Methodology and Approach.....</b>	<b>27</b>
3.1	Introduction.....	27
3.2	Solid modelling.....	30
3.3	CFD simulation.....	33
3.3.1	Mesh.....	34
3.3.2	Mesh independence.....	36
3.3.3	Solution solver.....	37
3.3.4	CFD-Post.....	38
3.4	Testing.....	39
3.4.1	Setup.....	39
3.4.2	Instrumentation.....	42
3.4.3	Instrument calibration.....	43
<b>4.</b>	<b>Chapter Four: Results.....</b>	<b>45</b>
4.1	CFD-Post results.....	45
4.1.1	Axial velocity contours.....	45
4.1.2	Power generated.....	47
4.1.3	Interpretation of results.....	49
4.2	Vehicle-top mounted testing results.....	50
4.2.1	Power generated.....	53
4.2.2	Comparative physical results.....	55
4.2.3	Interpretation of results.....	56
<b>5.</b>	<b>Chapter Five: Conclusion and recommendations.....</b>	<b>60</b>
5.1	Conclusion.....	60
5.1.1	Simulation.....	60
5.1.2	Field test.....	60
5.2	Recommendations.....	61
5.2.1	Solid modelling and simulation.....	61
5.2.2	Vehicle-top test rig.....	61
5.2.3	Future rotor research.....	62
<b>6.</b>	<b>References.....</b>	<b>63</b>
<b>7.</b>	<b>Appendices.....</b>	<b>65</b>

# List of Figures

Figure 1. Preliminary growth of global wind energy. (World Wind Energy Association, 2019[2020]).....	1
Figure 2. Graphical representation of small to large scale HAWTS. (McGowan et al., 2009). 2	
Figure 3. Large offshore HAWT (International Energy Agency,n.d. [2019]) and rooftop mounted small HAWT. (Duffy, 2009).....	2
Figure 4. Major components of a HAWT. (McGowan J, Rogers J, 2009).....	6
Figure 5. Rotor configurations. (McGowan J, Rogers J, 2009) .....	6
Figure 6. Small HAWT major components. (Song, 2012) .....	7
Figure 7. Airfoil profile. (McGowan et al. 2009).....	8
Figure 8. Cross section of airfoil showing the pitch angle, $\Theta_p$ . (McGowan et al. 2009).....	9
Figure 9. Airfoil profiles with different pitches to create twist in blade. (Kaya et al., 2018) .....	9
Figure 10. Backward, forward sweeping and symmetrical. (Kaya et al., 2018) .....	10
Figure 11. Blade coning. (Wei Xie Wei et al., 2017) .....	10
Figure 12. Rotor plane used for momentum theory. (Hansen, 2008).....	11
Figure 13. Illustration of blade profile element and blade lift, drag and velocity profile at rotor plane (Hansen, 2008).....	12
Figure 14. Sample of increased surface subdivision from A to D (Antonelli <i>et al.</i> , 2013) .....	16
Figure 15. Illustration of airfoil splines. (Kaya et al., 2018) .....	16
Figure 16. Sample of ANSYS control volume. (ANSYS, 2010).....	17
Figure 17. Turbulent boundary layers. (Tande, 2011).....	21
Figure 18. Illustration of boundary layer development over airfoil. (Hansen, 2008).....	22
Figure 19. Closed and open wind tunnels. (National Aeronautics and Space Administration.n.d. <a href="https://www.grc.nasa.gov">https://www.grc.nasa.gov</a> [2019]).....	24
Figure 20. Low-speed wind tunnel at CSIR. (Council of Scientific and Industrial Research, n.d. <a href="https://www.csir.co.za">https://www.csir.co.za</a> , [2019]).....	24
Figure 21. Sample of vehicle-top test rig (Dawoud, Amer and Gross, 2007) .....	25
Figure 22. Representation of instrument integrated with data acquisition system. (Song, 2012) .....	26
Figure 23. Chord length comparison between STD and ADP.....	29
Figure 24. Blade twist angle comparison between STD and ADP. ....	30
Figure 25. Full geometry for CFD simulation with dimensions in metre. ....	31
Figure 26. Rotor within rotating domain with dimensions of 1 m diameter and length of 0.21 m.....	31
Figure 27. Rotational periodic boundary at 120 degrees. ....	32
Figure 28. Blade section.      Figure 29. Hub base section. ....	32
Figure 30. Hub cap section. ....	32
Figure 31. Flow chart of CFD steps. ....	33
Figure 32. Complete meshed model including rotor, rotating and fluid domain.....	35
Figure 33. Hub with blade with zoomed in section of hub and root of blade (left picture) and zoomed in section of blade root of the trailing edge (right picture).....	35
Figure 34. Rotor with generator, tail and subassembly.....	40
Figure 35. Illustration of test rig on back of LDV.....	40
Figure 36. Side view of test rig with instrumentation positioning.....	41
Figure 37. Resister bank.....	42
Figure 38. LM393 sensor (left), LCD screen (centre) and Arduino Uno (right) ( <i>Electro Peak</i> , no date, <a href="https://electropeak.com/">https://electropeak.com/</a> [2020]) .....	42
Figure 39. Anemometer calibration graph with rotational speed versus wind speed.....	43
Figure 40. Rotor shaft rotational speed calibration graph. ....	44

Figure 41. Sample of axial velocity profile on one annulus cross the rotor.....	45
Figure 42. Axial velocity contours of rotational periodic section of rotor STD on left and ADP on right.....	46
Figure 43. Graphical representation of axial induction factor for STD and ADP rotors.....	47
Figure 44. Rotational speed versus power scatter plot for STD rotor.....	48
Figure 45. Rotational speed versus power scatter plot for ADP rotor. ....	48
Figure 46. Super imposed Power versus Rotational speed for STD and ADP rotors. ....	50
Figure 47. Trailer with complete test rig.....	51
Figure 48. Back view of test rig on trailer.....	51
Figure 49. Anemometer on left and rotor subassembly on right. ....	52
Figure 50. Section of road used on the R44, Betty's Bay. (2713-3466 R44, Betty's Bay, 7141 to 3099 R44, Betty's Bay, 7141 - Google Maps, nd, [2020]).....	52
Figure 51. Power versus rotational speed for STD rotor.....	54
Figure 52. Power versus rotational speed for ADP rotor.....	55
Figure 53. STD and ADP rotor performance curves super imposed.....	56
Figure 54. $C_p$ versus rotational speed for STD rotor simulation and field test. ....	57
Figure 55. Typical generator efficiency versus load percentage. (Wheeler and Southward, 2017) .....	57
Figure 56. $C_p$ versus rotational speed for ADP rotor simulation and field test.....	58
Figure 57. Blade airfoils (Kaya et al., 2018:167).....	65
Figure 58. Sample of airfoil coordinates in excel. ....	66
Figure 59. Sample of airfoil coordinates in note pad.....	67
Figure 60. Curves though xyz points. ....	67
Figure 61. Curves import window. ....	68
Figure 62. Imported splines.....	68
Figure 63. Consecutive splines selected. ....	69
Figure 64. Boundary boss window with green control points aligned.....	70
Figure 65. Hub frontal curve imported. ....	71
Figure 66. Hub profile.....	71
Figure 67. Solid hub.....	72
Figure 68. Combine function window. ....	72
Figure 69. Circular pattern function window. ....	73
Figure 70. Complete rotor model.....	73
Figure 71. Sketch of rotating domain.....	74
Figure 72. Boss extrudes of rotating domain. ....	75
Figure 73. Full geometry for CFD simulation. ....	76
Figure 74. Rotating domain geometry (zoomed in).....	76
Figure 75. Final step in solid works tree for creating full geometry. ....	76
Figure 76. Geometry tab and import geometry steps.....	77
Figure 77. Screenshot of DesignModeler. ....	78
Figure 78. Boolean 1 settings.....	79
Figure 79. Boolean 2 settings.....	79
Figure 80. Renamed solid bodies.....	80
Figure 81. Inlet face. ....	80
Figure 82. Outlet face.....	81
Figure 83. Outer wall face. ....	81
Figure 84. Hub faces selected.....	82
Figure 85. Blade faces selected.....	82
Figure 86. Pie 1 faces selected.....	83
Figure 87. Zoomed in section showing "innerdisc" face included in "Pie 1" selection.....	83
Figure 88. Geometry tree outline after naming all sections.....	83

Figure 89. Fluent opening dialog.....	84
Figure 90. Workflow drop down menu.....	84
Figure 91. Import geometry step.....	85
Figure 92. “Bladecellsize” settings.....	86
Figure 93. “Hubcellsize” settings.....	86
Figure 94. Create surface mesh settings.....	86
Figure 95. Rotational periodic boundaries settings.....	87
Figure 96. Describe geometry settings.....	87
Figure 97. Update boundaries settings.....	88
Figure 98. Update regions settings.....	88
Figure 99. Control volume mesh settings.....	88
Figure 100. Improve volume mesh settings.....	89
Figure 101. Tree outline with task page view.....	89
Figure 102. Viscous model window with settings.....	90
Figure 103. Models heading expanded.....	91
Figure 104. Air window with settings.....	91
Figure 105. “Innerdisc” window with settings.....	92
Figure 106. “Outerdomain” window with settings.....	93
Figure 107. “Blade” window with settings.....	93
Figure 108. “Hub” window with settings.....	94
Figure 109. “Inlet” window with settings.....	95
Figure 110. “Innerdisc-outerdomain” window with settings.....	95
Figure 111. “Interior-innerdisc” window with settings.....	95
Figure 112. “Interior-outerdomain” window with settings.....	96
Figure 113. “Outerwall” window with settings.....	96
Figure 114. “Outlet” window with settings.....	97
Figure 115. “Pie 2” window with settings.....	97
Figure 116. “Pie 1” window with settings.....	98
Figure 117. Methods setting in the task page.....	99
Figure 118. Initialization setting in the task page.....	99
Figure 119. Run calculation last step.....	100
Figure 120. Export window.....	101

# List of Tables

Table 1. Installed wind turbine capacity of top 10 countries. (World Wind Energy Association, 2019 [2020]).....	5
Table 2. Comparison between BEMM, CFD and physical testing.....	28
Table 3. Rotor geometry and physical testing inputs .....	29
Table 4. Mesh independence steps and results. ....	36
Table 5. Final meshing statistics for STD and ADP rotors. ....	37
Table 6. Final meshing quality for STD and ADP rotors. ....	37
Table 7. Solution solver constants.....	38
Table 7. Initial CFD inputs.....	38
Table 8. Power generated by STD and ADP rotors. ....	49
Table 9. Range of deviation for STD rotor field test.....	54
Table 10. Range of deviation for ADP rotor field test.....	55
Table 11. Simulation and field test results and performance increase. ....	59

## Glossary of Terms

Angle of attack	Angle between the chord line and the direction of relative wind velocity.
Airfoil	Curved profile shape of blade on 2D plane.
Axial velocity	Velocity parallel to axis of rotor rotation.
Blade	Wing-shaped component of rotor that converts wind energy to rotational energy.
Boundary streamline	The streamline that coincides with the tip of the blade.
Blockage ratio	Ratio between the frontal area of the rotor and the cross-sectional area of the wind tunnel test section.
Boundary layer	Slower-moving layer of fluid close to the surface of a solid body in a fluid stream.
Blade Element Momentum Method	An iterative method used to design and predict performance of wind turbine rotors.
Camber line	Locus of midpoints between the lower and upper surfaces of the airfoil.
Chord line	Straight line connecting the leading and trailing edges of an airfoil.
Controls	Hardware and software interconnected to control a system.
Drivetrain	Gearbox and shafts connecting rotor to generator.
Generator	Electrical device used to convert mechanical rotational energy into electrical energy.
Hub	Component that connects the blades to the drive shaft of a wind turbine.
Leading edge	The front edge of the blade (facing the oncoming fluid).
Nacelle	Aerodynamic cover for drivetrain, generator and controls of a wind turbine.
Rotor	Combination of blades and hub as one unit.
Rotor coning	Blade is tilted either upwind or downwind of the hub.
Solidity	The solid blade area compared to the rotor area in a plane.

Swept backward	In the plane of rotor rotation, the blade is swept in opposite direction of rotation from the radial reference from the centre of the hub.
Swept forward	In the plane of rotor rotation, the blade is swept in direction of rotation from the radial reference from the centre of the hub.
Transport equation	Differential equation describing the flow of a fluid.
Twist of blade	The change in pitch angle along the blade from root to tip.
Tip speed ratio	Ratio between the tangential speed of tip of blade and the actual wind speed.
Tailfin	Fin used in small HAWT'S to keep the rotor perpendicular to the freestream wind velocity.
Tail boom	The boom connecting the tailfin to the wind turbine body.
Trailing edge	The rearmost edge of a rotor blade where the airflow leaves the blade.

## Nomenclature

ADP	Adapted
CAD	Computer Aided Design
CFD	Computational Fluid Dynamics
CPUT	Cape Peninsula University of Technology
CSIR	Council of Scientific and Industrial Research
DC	Direct Current
BEMM	Blade Element Momentum Method
HAWT	Horizontal Axis Wind Turbine
LCD	Liquid Crystal Display
LDV	Light Delivery Vehicle
TSR	Tip Speed Ratio
WWEA	World Wind Energy Association
RANS	Reynolds Averaged Navier-Stokes
SAWEA	South African Wind Energy Association
STD	Standard
2D	Two-Dimensional
3D	Three-Dimensional

## List of Symbols

$B$	Number of blades [-]
$c$	Chord length of airfoil [m]
$C_l$	Lift coefficient [-]
$C_d$	Drag coefficient [-]
$C_n$	Normal load coefficient [-]
$C_t$	Tangential load coefficient [-]
$C_\mu$	k- $\epsilon$ model dimensionless constant [-]
$c(r)$	Chord at radial position of control volume [m]
$D$	Drag [N]
$dr$	Stream tube heights [m]
$F$	Prandtl's tip loss factor [-]
$F_e$	External force [-]
$I$	Identity tensor [-]
$k$	Turbulent kinetic energy [J/kg]
$L$	Lift [N]
$N$	Number of tubes [-]
$p$	Fluid pressure [Pa]
$P$	Average Fluid Pressure [Pa]
$P_n$	Load normal to rotor plane [N]
$P_t$	Load tangential to rotor plane [N]
$R$	Total rotor radius [m]
$r$	Blade local radius [m]
$r_r$	Measured resistance [N]
$t$	Time [s]

$U$	Average fluid velocity [m/s]
$U_{ax}$	Average axial fluid velocity [m/s]
$u$	Fluid velocity [m/s]
$u^*$	Reference velocity [m/s]
$V_{rel}$	Relative velocity to airfoil [m/s]
$V_o$	Wind speed [m/s]
$\mathcal{V}_v$	Measured Voltage [V]
$X$	Viscous sublayer thickness [m]
$X_{trans}$	Buffer layer thickness [m]
$X_\tau$	Thickness layer with full turbulent flow [m]
$y^+$	Distance from wall to element centroid [m]
$y$	Distance from wall to wall-cell [m]

## List of Greek Symbols

$a$	Axial induction factor [N/m]
$a'$	Tangential induction factor [N/m]
$\alpha$	Local angle of attack [deg]
$\phi$	Flow angle [deg]
$\Theta, \Theta_p$	Pitch angle [deg]
$\omega$	Angular velocity of rotor [rad/s]
$\rho$	Density [kg/m <sup>3</sup> ]
$\sigma(r)$	Solidity fraction at radial position $r$ [-]
$\sigma$	Solidity fraction [-]
$\varepsilon$	Turbulent dissipation rate [-]
$\mu_t$	Turbulent viscosity [N s/m <sup>2</sup> ]
$\mu$	Fluid viscosity [N s/m <sup>2</sup> ]
$\nu$	Kinematic viscosity [m <sup>2</sup> /s]
$\omega$	Specific turbulence dissipation rate [-]
$\pi$	Pi [-]

# 1. Chapter One: Introduction

## 1.1 Renewable resources on earth

Concerns around climate change and the depletion of fossil fuels have created a global imperative for increased use of renewable energy. According to the World Wind Energy Association (WWEA) there has been a steady increase of wind power generation globally. (World Wind Energy Association, 2019[2020]) Figure 1 shows the steady and significant global increase of power generated by wind energy – particularly since the mid-2000s.

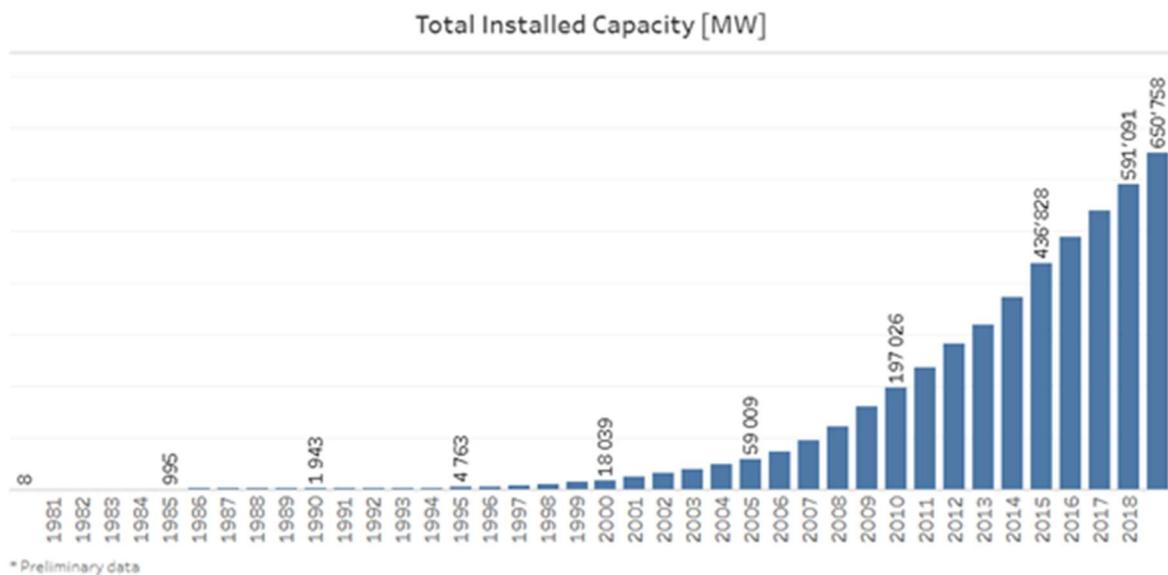


Figure 1. Preliminary growth of global wind energy. (World Wind Energy Association, 2019[2020])

Wind energy is an important source of renewable energy and is mostly harvested by means of large-scale on-shore and off-shore horizontal axis wind turbines (HAWTs). Small-scale HAWTs are used on boats, in remote areas where the electrical supply grid is not available, and in street lighting.

Figure 2 shows the scale – power relationship for some small to large HAWTs and Figure 3 shows the huge range in scale of HAWTs.

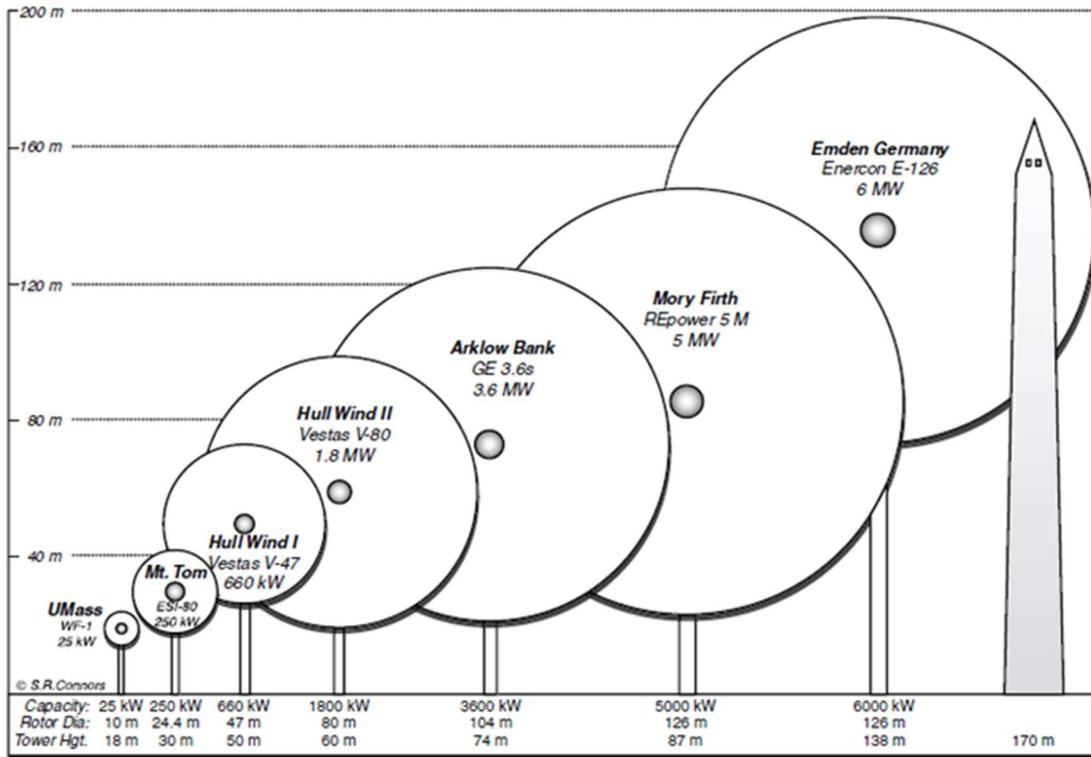


Figure 2. Graphical representation of small to large scale HAWTS. (McGowan et al., 2009)



Figure 3. Large offshore HAWT (International Energy Agency, n.d. [2019]) and rooftop mounted small HAWT. (Duffy, 2009)

## 1.2 Motivation for this work

Current research in the department of Mechanical Engineering at CPUT revealed a possible improvement to the conventional Blade Element Momentum Method (BEMM) for rotor designs that require relatively large hubs. This research interest was the analysis of the flow and

comparison of power output for conventional and adapted (ADP) BEMM designed rotors at lower wind speed. This research was focused on the evaluation of wind turbine rotors on half the design wind speed. This was to investigate the expected adapted rotor performance increase at lower operational wind speeds.

### **1.3 Research objectives**

The objective of this thesis is to compare the power generated, velocity profiles and wind boundary streamlines of a rotor that has been designed using the conventional BEMM against a rotor with same specifications designed using the 'ADP' BEMM.

#### **1.3.1 CAD modelling**

Three-dimensional blade and hub geometry data was provided and was transformed into solid models using Solid Works. The solid model needed to be compatible with ANSYS software for simulation purposes and with CNC/CAM software for manufacturing.

#### **1.3.2 ANSYS Fluent simulation**

ANSYS Fluent software was used to simulate the conventional and ADP rotors at a wind speed of 6 m/s and tip speed ratio (TSR) of 4. The purpose of the ANSYS CFD simulation was to compare the flow through and the power produced by the conventional and ADP rotors.

The scope of the simulation is the comparison of power generated by the rotors and comparison of axial velocities at the rotor plane - which is significant for axial induction and rotor efficiency.

#### **1.3.3 Manufacturing of the rotors**

Manufacturing of both the conventional and ADP rotors was done at CPUT, Bellville. The manufacturing process included three-dimensional (3D) printing of plugs, creation of moulds from the plugs and casting of the blades and hubs to complete the rotor sets. The design of the test rig was outside the scope of this thesis.

#### **1.3.4 Physical testing of the rotors**

Physical testing required the simultaneous recording of rotor output power, rotor angular velocity and wind speed. This was achieved using a vehicle-mounted wind turbine test rig. This stage required placement of instruments to capture accurate measurements so that the rotors could be compared.

## **1.4 Outputs**

This research project showed the performance of a HAWT rotor designed using a new ADP BEMM approach compared to a rotor design using the conventional BEMM. The new ADP BEMM is currently under research in the Department of Mechanical Engineering at CPUT. Further outputs were the solid modelling and manufacturing of the conventional and ADP rotors. The test rig and instrumentation were built for physical testing to capture the power output of the rotors. Flow analysis of the rotors was done using ANSYS Fluent to predict the flow through the rotors and their power outputs. Procedures for the solid modelling and the CFD analysis formed part of the output of this research.

## **1.5 Research design and methodology**

The study was conducted in the following stages:

1. Produced 'solid models' of 'conventional' and 'ADP' rotors from blade and hub geometrical data (provided by co-supervisor).
2. Simulated the performance and flow in CFD simulation.
3. Manufactured the rotors using 3-D printing, moulding and casting.
4. Tested the manufactured rotors on a vehicle-top mounted test rig to measure comparative power output.
5. Analysed CFD modelling results and compare power prediction with actual physical test results.
6. Created procedures for computer aided design (CAD) rotor modelling and CFD rotor simulation.

## **1.6 Scope of work**

This research investigated the performance of small HAWT rotors at off-design wind speed. All CFD simulations and physical tests were done at half the design wind speed. All blades in this study were radially symmetrical and the rotors had no coning. Excluded from this study were any comparisons to market related products. The purpose of the study was to compare rotor performance only, therefore the effect of tower, tail, near ground effects and generator losses were not included.

The scope included the development of procedures for the solid modelling and CFD simulation. These procedures were specific to this research to enable reproduction of CFD results and act as guide for similar future CFD analyses. Results from the physical testing of the rotors were included, but the manufacturing procedure of the rotors and test rig design with instrumentation were omitted from scope.

## 2. Chapter Two: Literature Review and Theoretical Background

### 2.1 Wind energy

Wind energy has been harnessed for windmills since the early 7th century. It was only in later centuries that wind energy was used to generate electricity by use of wind turbines. Fluctuation of fossil fuel prices determined popularity of wind turbines in the 19th century. The advantages of wind energy are that it is clean and free and can provide a stable long-term price for energy compared to fossil fuel energy plants. Wind energy is globally available on-shore and off-shore. The main disadvantage of wind energy is the wind fluctuations and therefore cannot be used directly for base load power. (Tande, 2011)

According to the WWEA report released end of 2019 the preliminary statistics on total installed wind turbine capacity reached 650.735 Gigawatt. This installed capacity can cover more than 5% of the global electricity demand. The growth rate at end of 2019 for wind turbines was 10.1% with China as the global leader in installed capacity with United States following in second. (World Wind Energy Association, 2019 [2020]) Table 1 shows the installed wind turbine capacity of the top 10 countries worldwide.

Table 1. Installed wind turbine capacity of top 10 countries. (World Wind Energy Association, 2019 [2020])

<b>Installed Capacity by the end of 2019 (MW)</b>					
<b>Country/Region</b>	<b>2019</b>	<b>2018</b>	<b>2017</b>	<b>2016</b>	<b>2015</b>
China	237 029	209 529	188 390	168 730	148 000
United States	105 433	96 363	88 775	82 033	73 867
Germany	61 357	59 313	56 190	50 019	45 192
India	37 529	35 129	32 879	28 279	24 759
Spain	25 808	23 494	23 026	23 020	22 987
United Kingdom	23 515	20 743	17 852	14 512	13 614
France	16 646	15 313	13 760	12 065	10 293
Brazil	15 452	14 707	12 763	10 800	8 715
Rest of the World	127 989	116 501	107 204	99 050	89 402
<b>Grand Total</b>	<b>652 777</b>	<b>593 110</b>	<b>542 856</b>	<b>490 524</b>	<b>438 844</b>

South Africa currently has an installed capacity of 2.078 Gigawatt according to the South African Wind Energy Association (SAWEA) which is about 0.31 % of the global installed capacity. (South African Wind Energy Association. n.d. Stats and Facts. <https://sawea.org.za> [2019])

### 2.1.1 Horizontal axis wind turbines

Wind turbines are machines that convert wind power into electrical power. HAWTs have their axis of rotation horizontal to the ground. The major components of a large HAWT are shown in Figure 4.

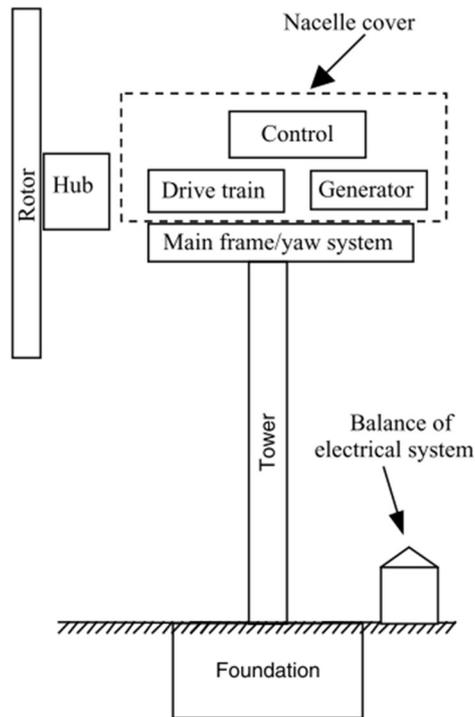


Figure 4. Major components of a HAWT. (McGowan J, Rogers J, 2009)

The *rotor* consists of the *blades* and *hub* of the wind turbine. In most large and medium HAWTs, rotors have three blades. *Rotors* may be installed upwind or downwind of the nacelle as illustrated in Figure 5. (McGowan J, Rogers J, 2009)

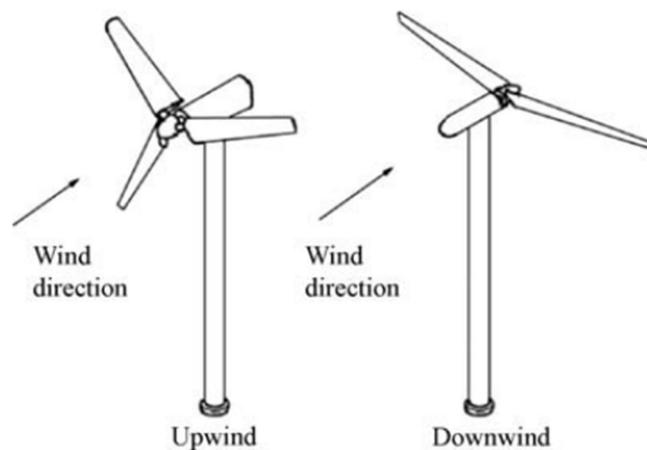


Figure 5. Rotor configurations. (McGowan J, Rogers J, 2009)

In most large HAWTs, the *drivetrain* includes a gear box to connect the *rotor's* low-speed input shaft to the generator's high-speed output shaft. The purpose of the gearbox is to increase the rotational speed from low to high speed. Other parts in the drivetrain are the bearings and a braking system for larger turbines to ensure the rotor does not rotate above maximum operation speeds. The function of the generator is to convert mechanical power to electrical power. *Controls* for a wind turbine may include sensors, controllers, power amplifiers and intelligence (computers). Controls are used to control operation and maximize power generation. The *nacelle* is an aerodynamic protection cover for the drivetrain, controls and generator. The *yaw system* keeps the rotor shaft in line with the wind. Yaw systems for large wind turbines are operated by means of a yaw motor with pinion and gear with a wind direction sensor mounted on the nacelle. Downwind rotor configuration sometimes uses a free yaw system. (McGowan J, Rogers J, 2009)

Small HAWT construction is slightly different to large HAWTs. In small HAWTs the *rotor* is usually connected directly to the *generator* and uses a free *yaw system* which is controlled by a *tailfin* to keep the rotor shaft in line with the wind. The main components of a small HAWT are shown in Figure 6. The *tail assembly* consists of the *tailfin* and *tail boom*. (Song, 2012)

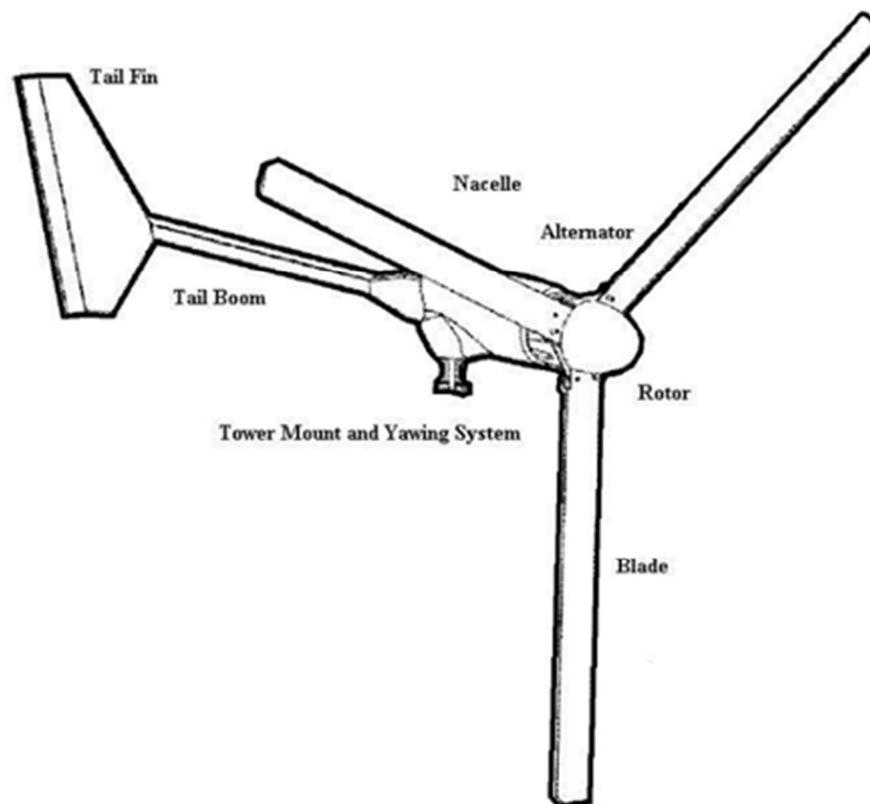


Figure 6. Small HAWT major components. (Song, 2012)

## 2.2 Rotor blade design considerations

Certain terms need to be defined in order to discuss blade design– as shown in Figure 7.

The *camber line* is the line halfway between the upper and lower surface airfoil surfaces. The front and the back endpoints of the *camber line* over the length of the blade respectively form the *leading edge* and the *trailing edge*. The straight line connecting the *leading* and *trailing* edges is the *chord line*. The *chord* of the airfoil is the length of the *chord line* from the *leading edge* to *trailing edge*. The angle created between the *chord line* and the relative wind or *freestream* velocity is the *angle of attack*. *Thickness* of the airfoil is measured between the upper and lower surfaces perpendicular to the *chord line*.

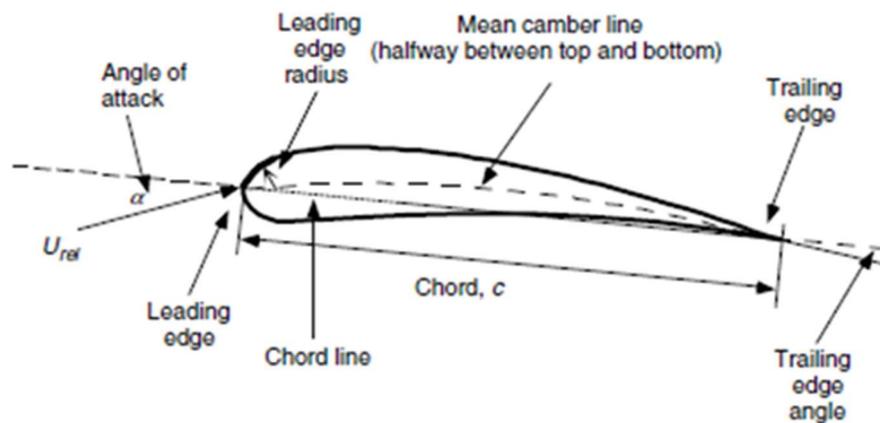


Figure 7. Airfoil profile. (McGowan et al. 2009)

The *pitch angle*,  $\Theta_p$  in Figure 8 is the angle between the blade's *chord line* and the plane of rotation looking at the cross section of the airfoil. *Twist* of the blade is created by the change of the *pitch angle* across the blade from root to tip illustrated in Figure 9 (McGowan et al. 2009)

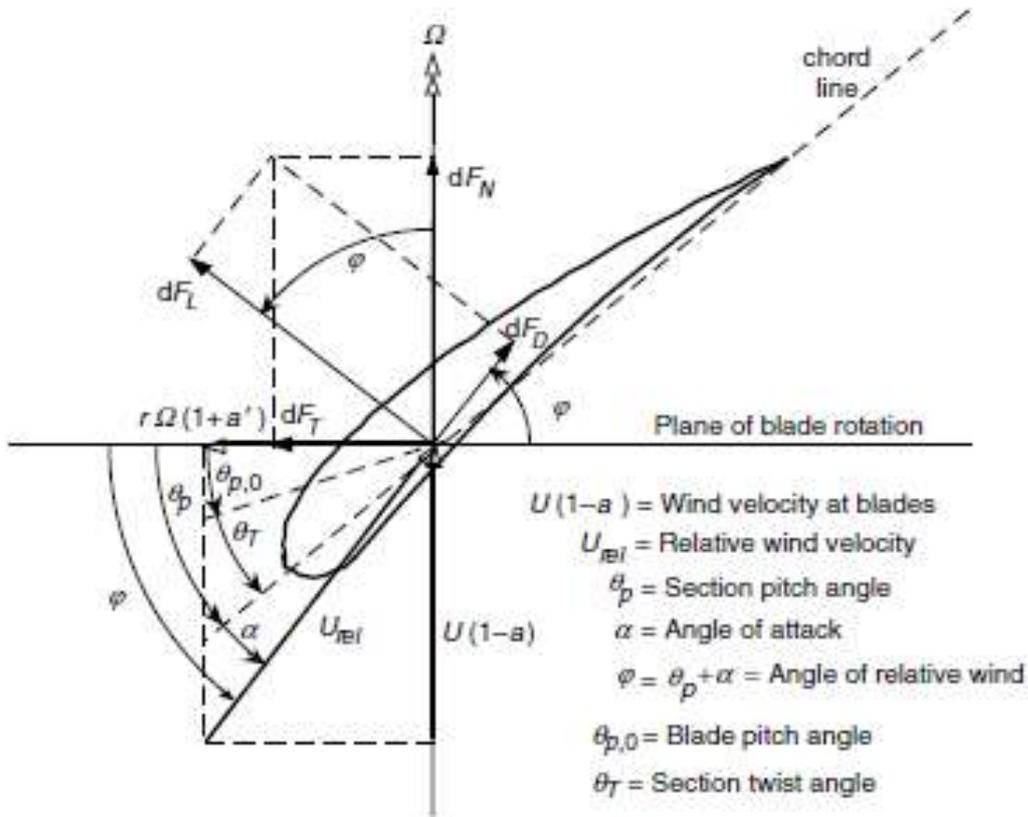


Figure 8. Cross section of airfoil showing the pitch angle,  $\theta_p$ . (McGowan et al. 2009)

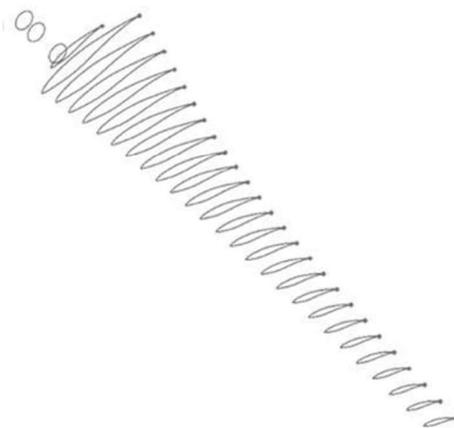


Figure 9. Airfoil profiles with different pitches to create twist in blade. (Kaya et al., 2018)

Further design consideration must take the blade position, relative to the hub, into account. Blades can be *swept backward* or *swept forward* from a radial reference taken from the centre of hub or can be symmetrical as shown in Figure 10. .

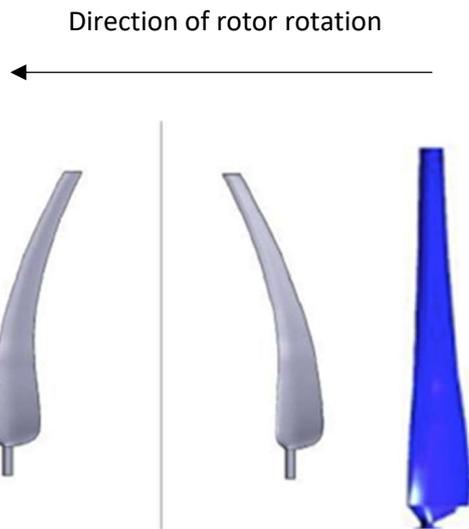


Figure 10. Backward, forward sweeping and symmetrical. (Kaya et al., 2018)

*Coning* of wind turbine rotors is when the blades are angled from the plane of rotation as in Figure 11. Coning of blades may be done to keep blade tips away from the tower or to reduce the effect of bending moments. (McGowan et al., 2009)

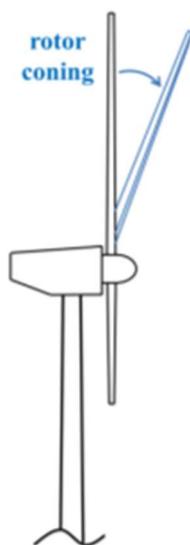


Figure 11. Blade coning. (Wei Xie Wei et al., 2017)

Airfoil and blade considerations such as *sweep* and *coning* influence the ability of the rotor to convert the wind kinetic energy into power. *Sweeping* and *coning* of blades were excluded in this study.

### 2.2.1 HAWT blade design software

Blade design software in industry makes use of the BEMM and below is a list of established software packages.

- Smart Blade (*Smart Blade.n.d.* <https://www.smart-blade.com> [2019])
- QBlade (Marten, 2012)
- Bladed (*Det Norske Veritas, n.d.* <http://www.dnvgl.com> [2019])
- AeroDyn (Jonkman *et al.*, 2015)

### 2.3 Blade element momentum method

The current or conventional method to design blades for wind turbines is the BEMM theory. This is the combination of two theories – momentum theory and blade-element theory.

Momentum theory refers to the analysis of forces on the blade in a control volume based on linear and angular momentum conservation. Momentum theory assumes that the loss of pressure or momentum is caused by the work done. (Moriarty and Hansen, 2005) Figure 12 shows the rotor plane used in momentum theory. Momentum theory applies to local events on the actual blades. Stream tubes with height  $dr$  with a number of tubes are introduced across the rotor as shown below in Figure 12.

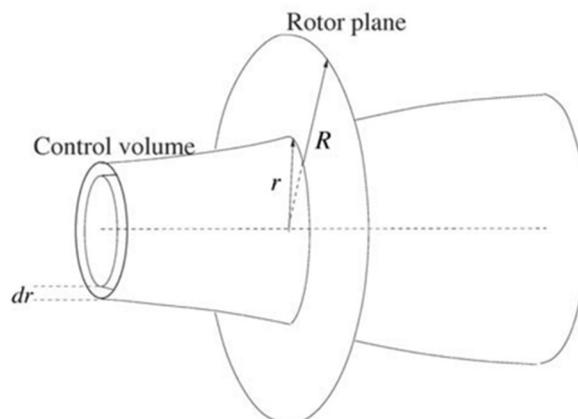


Figure 12. Rotor plane used for momentum theory. (Hansen, 2008)

Using the momentum theory, *thrust* is calculate by the integral momentum equation over the control volume with the rotor cross sectional area. *Torque* is calculated by the integral moment of momentum on the control volume. The equations derived from the integral momentum and integral moment of momentum are used to derive equations used by the BEMM. (Hansen, 2008)

Blade element theory refers to the analysis of forces on 2D sections of the blade based on the geometry of the blade. Blade element theory is used to relate the ability of the blade profile to extract power from the wind. (McGowan et al., 2009) An illustration of the 2D blade lift, drag and velocity profile of one element is shown in Figure 13.

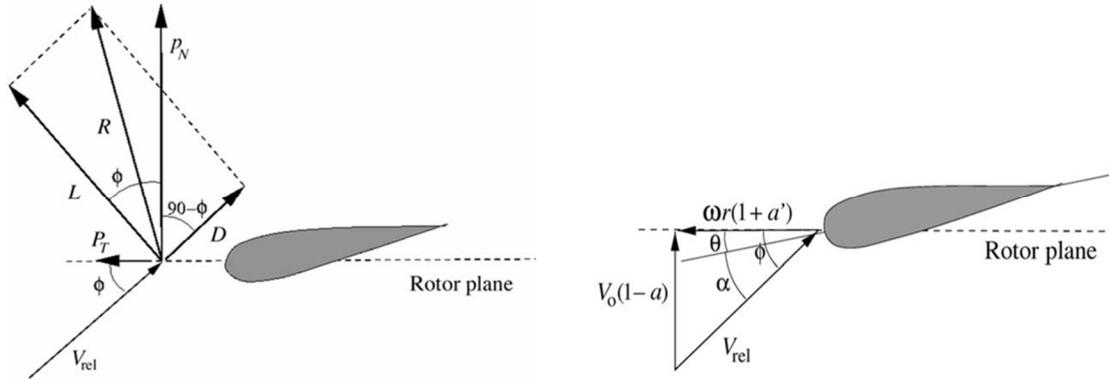


Figure 13. Illustration of blade profile element and blade lift, drag and velocity profile at rotor plane (Hansen, 2008)

In the velocity vector diagram, the local angle attack is:

$$\alpha = \phi - \Theta \quad (1)$$

$\alpha$  – Local angle of attack

$\phi$  – Flow angle

$\Theta$  – Pitch angle

Local angle of attack is the angle between the relative velocity  $V_{rel}$  and plane of rotation or so-called rotor plane. It is further seen that:

$$\tan \phi = \frac{(1-a)V_0}{(1-a')\omega r} \quad \text{From velocity diagram in Figure 13.} \quad (2)$$

$\phi$  – Flow angle

$r$  – Radius

$V_0$  – Wind speed

$a$  – Axial induction factor

$\omega$  - Angular velocity of rotor

$a'$  - Tangential induction factor

Equations (1) and (2) are used directly by the BEMM whereas the *thrust* and *torque* equations using the momentum theory are used to derive equations used by the BEMM. (Hansen, 2008)

In the forces vector diagram in Figure 13 the following equations are derived which are used in the BEMM:

$$C_n = P_n / 1/2 \rho V_{rel}^2 c \quad (3)$$

$$C_t = P_t / 1/2 \rho V_{rel}^2 c \quad (4)$$

$C_n$  – Normal load coefficient

$C_t$  – Tangential load coefficient

$P_n$  – Load normal to rotor plane

$P_t$  – Load tangential to rotor plane

$c$  – Chord length of airfoil

$V_{rel}$  – relative velocity to airfoil

$\rho$  – Density

The normal and tangential loads  $P_n$  and  $P_t$  are calculated by determining the lift and drag with:

$$L = 1/2 \rho V_{rel}^2 c C_l \quad (5)$$

$$D = 1/2 \rho V_{rel}^2 c C_d \quad (6)$$

$L$  – Lift

$D$  – drag

$V_{rel}$  – relative velocity to airfoil

$c$  – Chord length of airfoil

$C_l$  – Lift coefficient

$C_d$  – Drag coefficient

The lift and drag forces are projected into the normal and tangential plane as seen in the force vector diagram:

$$P_n = L \cos \phi + D \sin \phi \quad (7)$$

$$P_t = L \sin \phi - D \cos \phi \quad (8)$$

$P_n$  – load normal to rotor plane

$P_t$  – Load tangential to rotor plane

$L$  – Lift

$D$  – Drag

$\phi$  – Flow angle

A further two equations are derived combining momentum and element equations to express the variation of axial and tangential forces on the blade by the axial induction and tangential induction factor:

$$a = \frac{1}{\frac{4 \sin^2 \phi}{\sigma C_n} + 1} \quad (9)$$

$$a' = \frac{1}{\frac{4 \sin \phi \cos \phi}{\sigma C_t} - 1} \quad (10)$$

$a$  – Axial induction factor

$a'$  - Tangential induction factor

$C_n$  – Normal load coefficient

$C_t$  – Tangential load coefficient

$\phi$  – Flow angle

$\sigma$ – Solidity fraction

The Solidity fraction  $\sigma$  is the blade area compared to the rotor area on the plane or annular area in the control area and is expressed by: (Hansen, 2008)

$$\sigma(r) = c(r)B / 2\pi r \quad (11)$$

$\sigma(r)$  – Solidity fraction at radial position  $r$

$c(r)$  – chord radial position of the control volume

$B$  – number of blades

$r$  - Radius

The BEMM model makes it possible to calculate *thrust*, *torque* and *power* for various values of *wind speed*, *pitch angle* and *rotational speed*. The BEMM model makes two assumptions namely:

1. Assumes no dependencies meaning that what happens at one location cannot be felt by another location.
2. Forces of the blade are constant on the flow in each annular element. This is for a rotor with infinite number of blades.

The BEMM model makes use of an iterative method with the following steps.

- Step 1. Assume initial  $a$  and  $a'$ . Normally close to zero.
- Step 2. Determine the flow angle  $\phi$  using equation (2).
- Step 3. Determine local angle of attack  $\alpha$  using Equation (1).
- Step 4. Use  $C_l(\alpha)$  and  $C_d(\alpha)$  from airfoil information table.
- Step 5. Determine  $C_n$  and  $C_t$  with equations (3) and (4).

- Step 6. Determine  $a$  and  $a'$  using equations (9) and (10).  
 Step 7. If  $a$  and  $a'$  change significantly, repeat from step 2 otherwise finish.  
 Step 8. Calculate local loads on blades.

The Prandtl's tip loss factor  $F$  is used to correct the design and performance prediction for a rotor with finite number of blades.  $F$  is determined by:

$$F = \frac{2}{\pi} \cos^{-1}(e^{-f}) \quad (12)$$

Where:

$$f = \frac{B}{2} \frac{R-r}{r \sin \phi} \quad (13)$$

$B$  – Number of blades

$f$  – Ratio

$R$  – Total rotor radius

$r$  – Local radius

$\phi$  – Flow angle

Introducing the Prandtl's tip loss factor to equations (9) and (10) it becomes:

$$a = \frac{1}{\frac{4F \sin^2 \phi}{\sigma C_n} + 1} \quad (14)$$

$$a' = \frac{1}{\frac{4F \sin \phi \cos \phi}{\sigma C_t} - 1} \quad (15)$$

Equations (14) and (15) must be used in the BEMM iteration step 6 instead of (9) and (10) and the Prandtl's tip loss factor  $F$  must be determined after step 2. (Hansen, 2008). This chapter has shown the basic BEMM that was used to create the rotor geometry data that was provided as the starting point for this research.

## 2.4 Solid modelling

A key factor for the 3D modelling was the subdivision of the blade surface which increases the surface elements near the edges of the blade. Antonelli *et al.*, (2013) mentioned that testing of different subdivision of surfaces was done in certain software with built-in capabilities such as Creo and other software such as Solid Works which introduced plug-in modules for this purpose. It was mentioned that the tested built-in modules and plug-in modules did not treat the generated subdivision of surfaces in a way that truly reflected the geometry of the model.

Figure 14 illustrates the rounding of a surface by increasing the subdivision of surfaces. (Antonelli *et al.*, 2013)

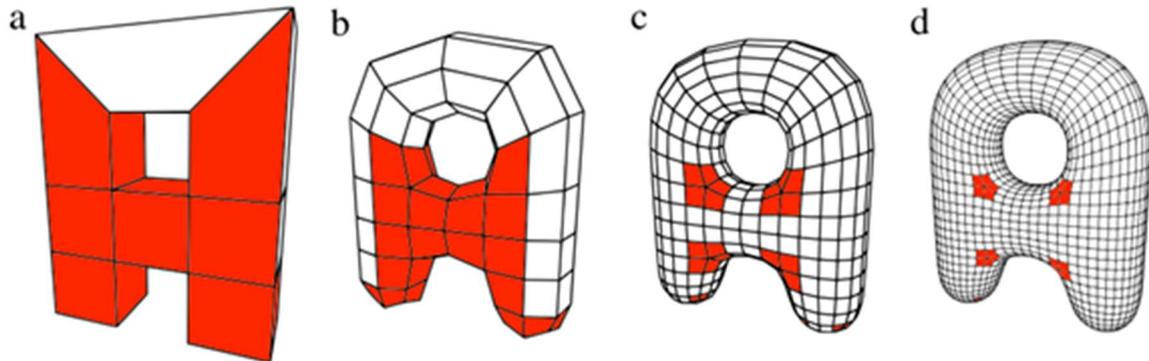


Figure 14. Sample of increased surface subdivision from A to D (Antonelli *et al.*, 2013)

A new approach for the modelling of surfaces which did not make use of built-in software or plug-in modules was mentioned by Cong and Song, (2014) to overcome this problem. The approach was to create closed spline elements for the blade using the coordinates of the airfoil per element. Each element's airfoil coordinates were imported individually. The airfoil coordinates were transformed into closed splines. The surface of the blade was created by lofting the closed splines. (Cong & Song, 2014) This methodology provided simple parametric updates to airfoil geometry and the correct surface finish for this research. Figure 15 is an illustration of airfoil coordinates converted into splines along the blade. (Kaya *et al.*, 2018)

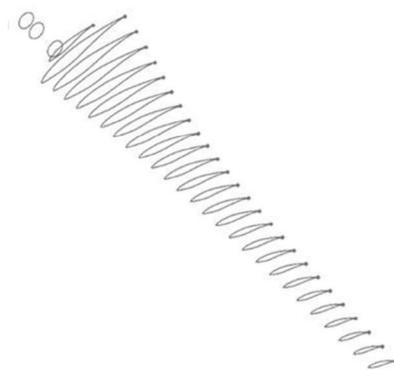


Figure 15. Illustration of airfoil splines. (Kaya *et al.*, 2018)

## 2.5 Numerical simulation for CFD

The numerical method to predict fluid flow in systems or CFD are based on three fundamental equations. These partial differential equations for the conservation of mass, momentum and energy are used to describe the behaviour of flow-based on the assumption that the fluid is a continuous medium. The CFD divides the physical system or domain being modelled into

smaller control volumes or elements as shown in Figure 16. This approach allows the partial differential equations to be replaced by algebraic equations. The relationship of these algebraic equation within the control volumes predicts and describes the flow variables.(Tande, 2011) The integration of equations over each finite volume is based on the element average value which has the advantage that conservation equations of mass, momentum and energy are conserved at local scales. This allows for complex meshed geometries. (Namiranian, 2011)

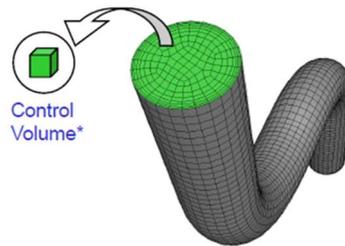


Figure 16. Sample of ANSYS control volume. (ANSYS, 2010)

### 2.5.1 Fundamental equations

The fundamental governing equations for CFD are based on fluid dynamic physical principles namely:

1. Mass conservation which states that the rate of mass flow in equals the rate of mass out flow.
2. Momentum conservation (Newton's second law) - the rate of momentum change equals the sum of forces on the fluid particles.
3. Energy conservation which is the rate of change of energy of a fluid particle and equals the rate of heat gained plus rate of work done on the fluid particle which is only applicable to simulation when temperature changes occur which is therefore, excluded here.

The Navier-Stokes equations for the two applicable conservation laws were applied to the control volumes for this study. (Tande, 2011)

Conservation of momentum:

$$\rho \left( \frac{\partial u}{\partial t} + u \cdot \nabla u \right) = -\nabla p + \nabla \cdot \left( \mu (\nabla u + (\nabla u)^T) - \frac{2}{3} \mu (\nabla \cdot u) I \right) + F_e \quad (16)$$



$u$  – Fluid velocity

$F_e$  – External force

$t$  – Time

$I$  – Identity tensor

$p$  – Fluid pressure

$\rho$  – Fluid density

$\mu$  – Fluid viscosity

The terms in the conservation of momentum equation relates to inertial forces (1), pressure forces (2), viscous forces (3) and external forces (4). The conservation of momentum equation is solved together with the equation of continuity or conservation of mass: (SimScale, 2017 [2020])

$$\frac{\partial \rho}{\partial t} + \nabla \cdot (\rho u) = 0 \quad (17)$$

$u$  – Fluid velocity

$\rho$  – Fluid density

The Navier-Stokes equations are further adapted to specific flow regimes for example flow with high or low Reynolds numbers.

## 2.5.2 Turbulence model

It was mentioned by Tande (2011) that fluid flow becomes unstable above certain Reynolds numbers and became turbulent flow. In turbulent flow the velocity and pressure changed randomly over time. This random flow created velocity and pressure eddies or so-called turbulent eddies in three dimensions with different length scales. When the Reynolds number was high, the inertial forces in term (1) were larger than the viscous forces in term (3) in equation (15). To solve such turbulent flow, the control volume had to be fine enough to incorporate the smallest turbulent eddies. Simulations with this type of flow regime required large amount of computer resources. (SimScale, 2020)

An alternative method is the Reynold Averaged Navier-Stokes equations (RANS). The RANS method averages the pressure and velocity in time. The RANS equation is:

$$\underbrace{\rho(\mathbf{u} \cdot \nabla \mathbf{u}) + \nabla \cdot \left( \mu_T (\nabla \mathbf{u} + (\nabla \mathbf{u})^T) - \frac{2}{3} \mu_T (\nabla \cdot \mathbf{u}) \mathbf{I} \right)}_{(1)}$$

$$= \underbrace{-\nabla p}_{(2)} + \underbrace{\nabla \cdot \left( \mu (\nabla \mathbf{u} + (\nabla \mathbf{u})^T) - \frac{2}{3} \mu (\nabla \cdot \mathbf{u}) \mathbf{I} \right)}_{(3)} + \underbrace{Fe}_{(4)} \quad (18)$$

$\mathbf{U}$  – Average fluid velocity

$P$  – Average fluid pressure

$\rho$  – Fluid density

$Fe$  – External force

$I$  – Identity tensor

$\mathbf{u}$  – Fluid viscosity

$\mu_T$  – Turbulent fluid viscosity

The terms (1) to (4) descriptions remains as is in equation (16)

Namiranian (2011) explained that the shear stress transport (SST) turbulence model is a combination of the k- $\epsilon$  turbulence model and the k- $\omega$  model. By combining the two models the CFD simulation uses k- $\epsilon$  modelling for freestream fluid and the k- $\omega$  model which is suitable for near-wall turbulent flow. The two transport equations to be solved for each control volume were:

k- $\epsilon$  turbulence model:

$$\mu_t = \rho C_\mu \frac{k^2}{\epsilon} \quad (19)$$

$\mu_t$  - Turbulent viscosity

$\rho$  - Density

$C_\mu$  – k- $\epsilon$  model dimensionless constant

$k$  – Turbulent kinetic energy

$\varepsilon$  – Turbulent dissipation rate

k- $\omega$  turbulence model:

$$\mu_t = \rho \frac{k}{\omega} \quad (20)$$

$\mu_t$  - Turbulent viscosity

$\rho$  – Density

$k$  – Turbulent kinetic energy

$\omega$  – Specific turbulence dispensation rate

### 2.5.3 Simulation blockage factor

Wind turbine rotor CFD simulation required consideration of the *blockage factor*. The blockage factor is the ratio between the 2D frontal area of the rotor and the 2D plane of the fluid domain test area in the freestream direction. Research done by Chen and Liou, (2011) showed that a blockage ratio of 10% requires a blockage correction factor. Chen and Liou (2011) stated that it is acceptable to have no blockage correction for a blockage ratio less than 10%. Thus, it was important to design the fluid domain to have a blockage ratio of less than 10%.

### 2.5.4 Boundary layer

A boundary layer occurs in the area close to solid boundary walls. In this analysis, a boundary layer occurred on the walls of the blades and hub and on the inside wall of the fluid domain. In the boundary layer the velocity variables of the working fluid have strong gradients and are greatly influenced by viscous effects. Modelling that includes the boundary layer for in a CFD calculation is important. Figure 17 shows a detailed illustration of the three layers for turbulent boundary condition.

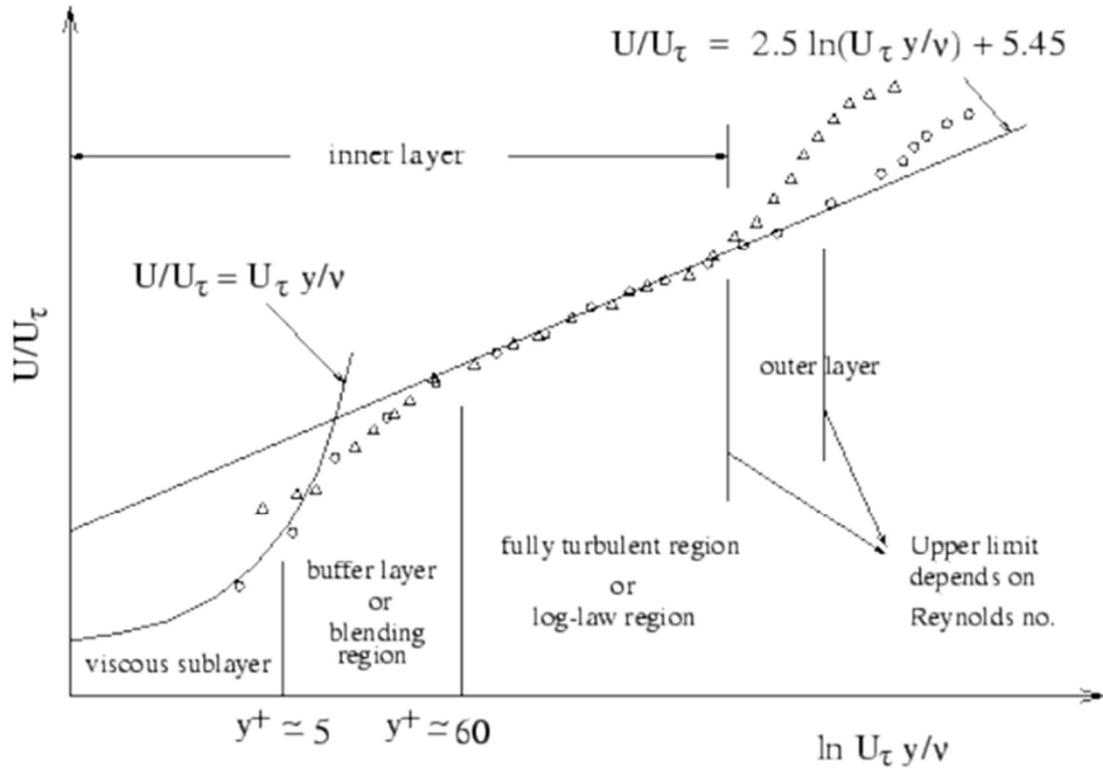


Figure 17. Turbulent boundary layers. (Tande, 2011)

The first layer is the viscous sublayer where viscosity and shear stress are dominant, similar to laminar flow. The second stage is the buffer layer where laminar flow starts changing to turbulent flow, but the turbulent flow is not yet fully developed. The turbulent effects and molecular viscosity are of equal importance in this layer. Lastly the outer layer is where the flow has developed into full turbulent flow. The three layers' magnitude and time variance are mainly determined by the Reynolds number (Tande, 2011). As mentioned in section 2.5.2 the SST turbulence model use the  $k-\epsilon$  model for flow outside the boundary layer and  $k-\omega$  model within the boundary layer. (Namiranian, 2011) The development of boundary layers over an airfoil is illustrated in Figure 18 where  $X$  is the viscous sublayer,  $X_{trans}$  the buffer layer and  $X_T$  the layer with full turbulent flow.

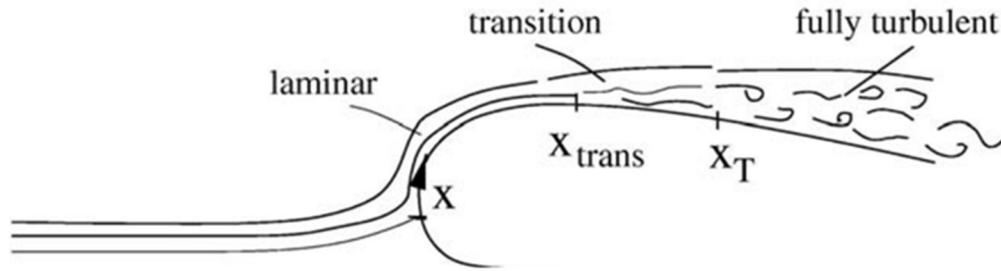


Figure 18. Illustration of boundary layer development over airfoil. (Hansen, 2008)

### 2.5.5 Meshing

Meshing refers to the discretization of the flow domain or geometry into smaller control volumes. Near-wall, control volumes or elements need to be smaller or finer than expected boundary layers for the CFD solver to resolve the boundary layer complexity correctly according to the turbulence model chosen. (Namiranian, 2011) The height of the first element referred to as  $y^+$  which is from the surface of the wall to centroid of the element adjacent to the wall may be estimated by equation (21). In Figure 17 the x-axis represents the  $y^+$  approximate values with the three boundary layers for turbulent flow and in this case the  $y^+$  value for laminar boundary layer is for  $y^+$  below 5. In order for CFD to resolve for the laminar boundary layer correctly, multiple mesh layers need to be present below the value of 5 therefore the  $y^+$  value has to be significantly smaller than 5. The  $y^+$  value may be estimated from equation 21. (Tande, 2011)

$$y^+ = \frac{yu^*}{\nu} \quad (21)$$

$y^+$  - Distance from wall to element centroid

$y$  - Distance from wall to wall-cell

$u^*$  - Reference velocity

$\nu$  - Kinematic viscosity

CFD meshing makes use of mesh shapes including pyramids, tetrahedrons and prisms for example. The goal was to have a fine mesh to resolve the boundary layer correctly and because the meshing influences results, we therefore need to have sufficient computational resources to solve a problem of this size correctly. (Namiranian, 2011) ANSYS offers boundary-meshing options namely: smooth transition, first layer thickness and first aspect ratio. The three options define the boundary meshing with different parameters. Choosing the correct option largely depends on the turbulent flow model. The number of boundary layers in

all three options is the most important parameter in order to capture the turbulent flow field. The quantity of control volumes or elements should be sufficient for mesh independence to be reached. (Mara *et al.*, 2014) Mesh independence was taken to be when we reached a state where the output torque remained unchanged as the mesh was refined following Khlaifat *et al.*, (2020) The obvious trade-off for a high quality mesh with low residual error is the increased computer resources required to simulate results. (Bouhelal *et al.*, 2018)

## **2.6 Physical testing**

Physical testing was used as a way to validate the BEMM and CFD results and to test the validity of assumptions and simplifications made. This chapter elaborates on physical testing, the requirements and possible measuring errors.

### **2.6.1 Blade manufacturing**

Wind turbine blades are continuously exposed to loads from the wind and the two main requirements for blade materials are high stiffness and low density. Stiffness of the blade ensures the aerodynamic performance and low density to minimise the weight and centrifugal forces. In industry, many different materials are used for manufacturing – taking into consideration the lifetime cycle and size. Small wind turbines for simulation validation do not need to consider long lifetime cycle and the option for manufacturing materials may be limited by resources available. Materials may include steel, wood or composites. (Song, 2012)

### **2.6.2 Testing options**

There were three methods available for physical testing. The first method was wind tunnel testing. This provides a more easily controlled environment, however a large wind tunnel was required to avoid high blockage ratios as mentioned in section 2.5.3.

In most cases for wind tunnel testing the rotors would be scaled to have an acceptable blockage ratio. In this study the rotors may not be scaled as they were already at the lower size limit - owing to the Reynolds number requirement for turbulent flow over the blades.

Instead, available wind tunnels have been considered for optimal testing. Wind tunnels fall into two categories namely open circuit and closed circuit. The advantages of using an open circuit are the good quality of propulsion and smoke visualization compared to the superior uniform flow quality and low operating cost of a closed circuit. (National Aeronautics and Space Administration. *n.d.* <https://www.grc.nasa.gov> [2019]) Figure 19 shows both open and close wind tunnels.

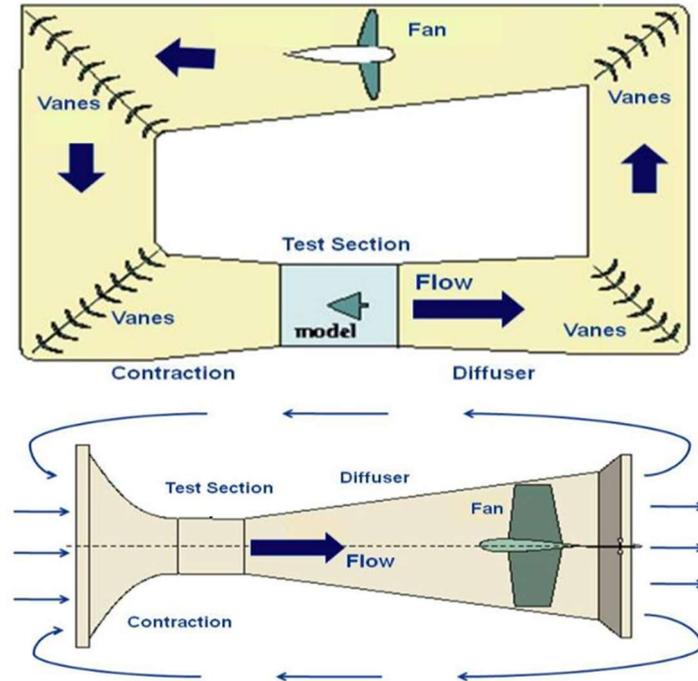


Figure 19. Closed and open wind tunnels. (National Aeronautics and Space Administration.n.d. <https://www.grc.nasa.gov> [2019])

The Council of Scientific and Industrial Research (CSIR), Pretoria has a wind tunnel suite for engineering tests. The suite includes a low-speed tunnel, seven-metre tunnel, and medium and high-speed tunnels. The largest wind tunnel at CSIR is too small for the testing requirements, is expensive to use and the wind velocity can only be adjusted in steps by the number of fans used. (CSIR, 2018). Figure 20 shows the low-speed wind tunnel at CSIR, Pretoria.

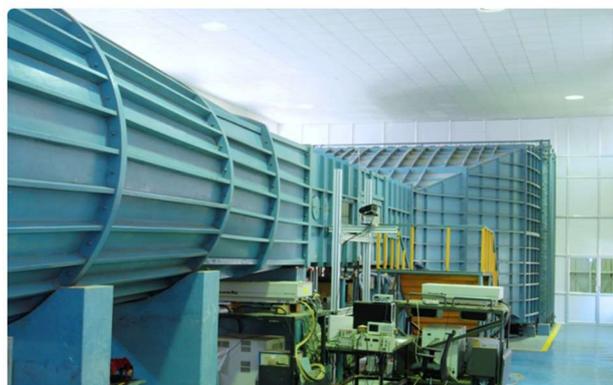


Figure 20. Low-speed wind tunnel at CSIR. (Council of Scientific and Industrial Research, n.d. <https://www.csir.co.za>, [2019])

Research by Refan and Hangan,(2012) showed a good relationship between prediction and wind tunnel testing results. They reported that wind tunnel testing was limited due to size, availability and cost efficiency and blockage factor correction on test data produced satisfactory result when applied to HAWTs. As a finding of their research they also recommended that HAWT rotor testing be complemented by field testing due to the blockage limitation of wind tunnels.

The second method to test a small wind turbine rotor was to install the wind turbine on a tower at a suitable area with expected wind speeds used in the BEMM and CFD simulation. This method of field testing takes months to gather enough data for performance evaluation at the correct wind speed. This method Song, (2012) claimed to be the best option.

The third method considered, was to mount the wind turbine on the back of a moving vehicle. The relative velocity of the vehicle simulates the wind tunnel environment. This method of testing was a cheaper method compared to wind tunnel testing and was more suited to testing with a shorter duration. Studies by Dawoud et al., (2007) compared vehicle-top testing of a small HAWT to BEMM prediction and found that there was an excellent agreement. Successful agreement and accuracy of vehicle-top field testing was mostly dependent on the accuracy of the BEMM model or CFD simulation according to Dawoud et al., (2007).



Figure 21. Sample of vehicle-top test rig (Dawoud, Amer and Gross, 2007)

A vehicle-top test rig is shown in Figure 21. This test method allows for easy rotor change and instrumentation placing compared to wind tunnel testing. (Song, 2012)

### 2.6.3 Instrumentation

Selection of instrumentation required for the physical testing was guided by the BEMM and CFD results. The accuracy of instrumentation used during the physical test - whether in a wind tunnel or on car top rig - was essential for meaningful results. The trade-off for accuracy in instrumentation was their expense. A data acquisition system connected to a computer was necessary to collect the measured data from the instruments. The orientation of instrumentation during the physical test was important and the position of sensors needed to exclude effects of vehicle wake and structural interference that could have caused error readings. Instruments required for testing are: (Song, 2012)

- Cup anemometer for wind speed.
- Multimeters (x2) for display plus step-down circuit for voltage logger signal and shunt resistor circuit for current logger signal.
- Speed sensor for rotational speed.
- Data logger.

Figure 22 is a representation of typical instruments integrated with a data acquisition system.

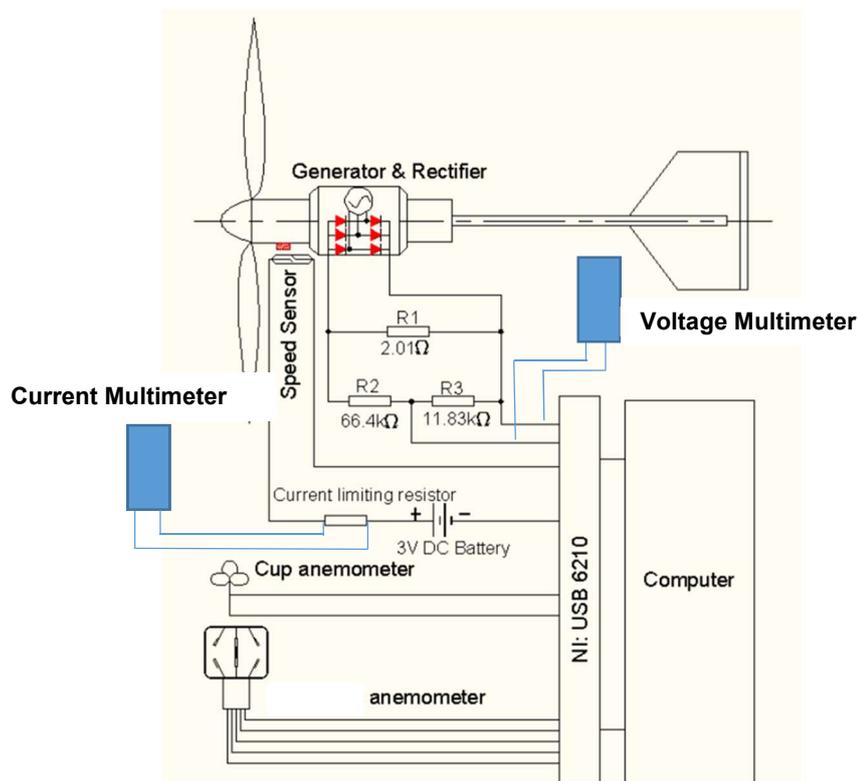


Figure 22. Representation of instrument integrated with data acquisition system. (Song, 2012)

## **3. Chapter Three: Methodology and Approach**

### **3.1 Introduction**

The geometrical data for a rotor designed using the 'conventional' BEMM referred to as standard (STD) and a rotor designed using an 'adapted' BEMM referred to as ADP were provided as the starting point for this research.

The goal of this research was to compare the results from CFD simulation and physical testing of a STD and ADP rotor. Differences between BEMM prediction, CFD simulation and physical testing were expected and Table 2 below compares BEMM, CFD and physical testing and methods.

Table 2. Comparison between BEMM, CFD and physical testing.

<b>Blade Element Momentum Method</b>	
<b>Assumptions</b>	
No dependencies meaning that what happens at one location cannot be felt by another location	
Forces of the blade is constant on the flow in each annular element. This is for a rotor with infinite number of blades	
Fully turbulent flow	
<b>Method</b>	
Momentum theory: assumes that the loss of pressure or momentum is caused by the work done	
Blade element theory: refers to the analysis of forces on 2 dimensional (2D) sections of the blade based on geometry of the blade	
<b>CFD Simulation</b>	
<b>Assumptions</b>	
Dependencies where CFD assumes 3D flow. What happens at one location can be felt by another	
Fully turbulent flow	
Steady state flow with fluid properties at single point not changing over time	
<b>Method</b>	
RANS equations used on discretization of flow system	
SST k- $\omega$ Turbulent model used as transport equations	
<b>Possible Errors</b>	
Rounding off of values during solution iteration	
Meshing limitations	
<b>Physical Testing</b>	
<b>Assumptions</b>	
Dependencies with 3D flow present. What happens at one location can be felt by another	
Fully turbulent flow	
Steady state flow with fluid properties at single point not changing over time	
<b>Method</b>	
Vehicle test rig with instrumentation to capture expected results	
<b>Possible Errors</b>	
Instrumentation accuracy	

The basic geometry and simulation inputs for the two rotors are shown in Table 3. The STD and ADP rotors had the same basic geometry.

Table 3. Rotor geometry and physical testing inputs

Hub ratio of 20%	
<b>Rotor geometry</b>	
Rotor diameter	940 mm
Hub diameter	188 mm
Blade length	376 mm
<b>Inputs for CFD simulation</b>	
Tip speed ratio	4
Rotational speed	794.59 rpm
Wind speed	6 m/s
Blockage factor	0.06%

The main difference between the STD and ADP rotors were the twist and chord lengths of the airfoil profiles. The graphs in Figure 23 and Figure 24 are the comparison of the cord length and twist of blade for the STD and ADP rotors respectively. The x-axis for both graphs is the ratio of local radius  $r$  and total blade radius  $R$ . The chord length on the y-axis is in metres and the twist angle in degrees.

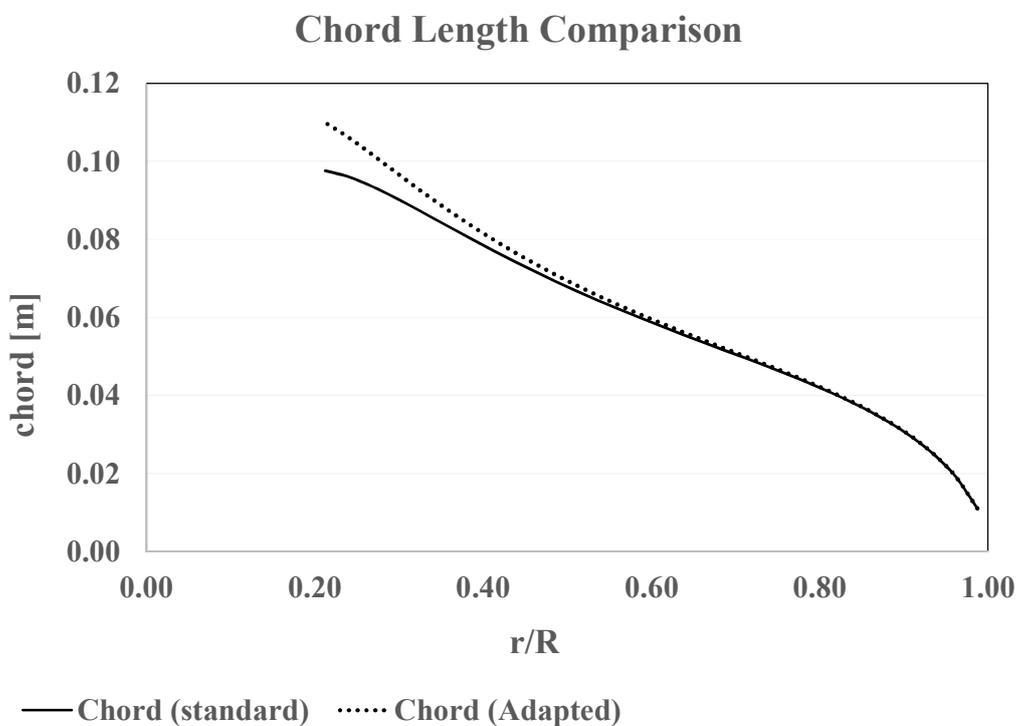


Figure 23. Chord length comparison between STD and ADP.

## Twist Angle Comparison

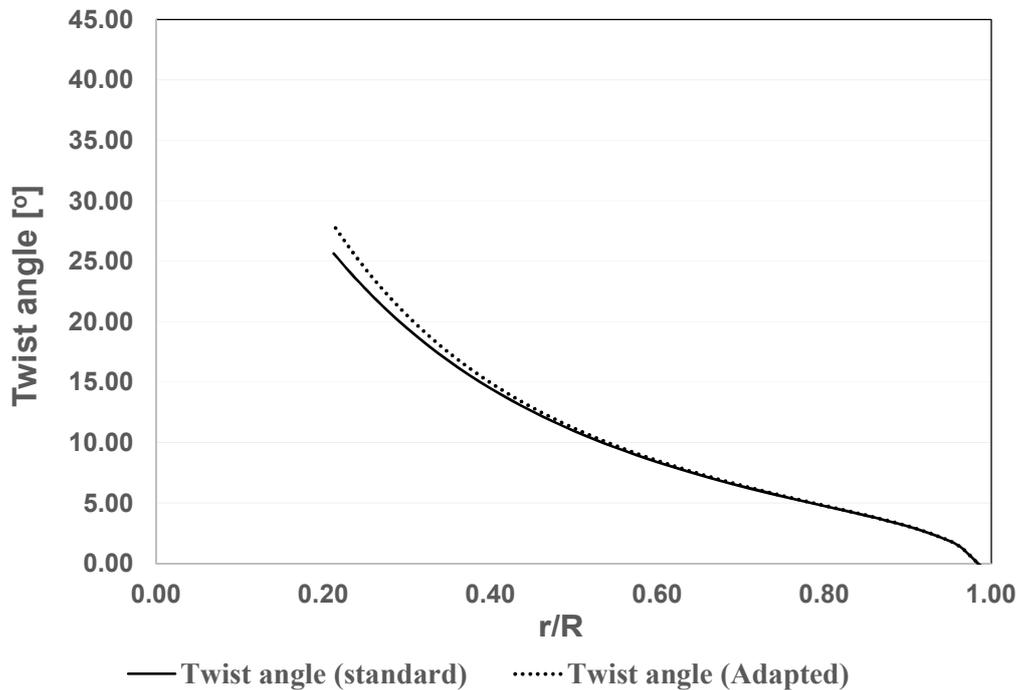


Figure 24. Blade twist angle comparison between STD and ADP.

Chord length and twist angle graphs indicated that the ADP rotor had a longer chord length and an increased twist angle near the root of the blade. Towards the tip of the blade, the chord length and twist of the ADP rotor blends into the chord length and twist of the STD rotor. The subtle change in blade geometry near the hub of the ADP rotor was expected to make better use of the axial velocity gradient around the relatively large hub. (Sant, 2007)

### 3.2 Solid modelling

An identical procedure was followed for solid modelling of both the STD and ADP models. Solid Works was used to create the rotors and domains necessary for the CFD simulations. A detailed procedural guide is provided in Appendix 7.1. The geometric coordinates of the element airfoils (profiles) that make up the blade were provided as the starting point. The only differences between the STD and ADP blades were the twist and chord lengths of the blade. During the modelling of the rotors with the domains it was important to have adequate space between the rotor and rotating domain boundaries for full flow development during simulation. This reduced the probability of any reverse flow or stagnation development between the boundaries of the rotating domain and the rotor. A complete solid model is shown in Figure 25. The rotor is enclosed within a domain shown in Figure 26 that has a 1 m diameter and 0.21 m length. This domain was rotated in the simulation and the rotating

domain was enclosed in the fluid domain in the CFD software. The fluid domain had a diameter of 7 m and length of 18 m.

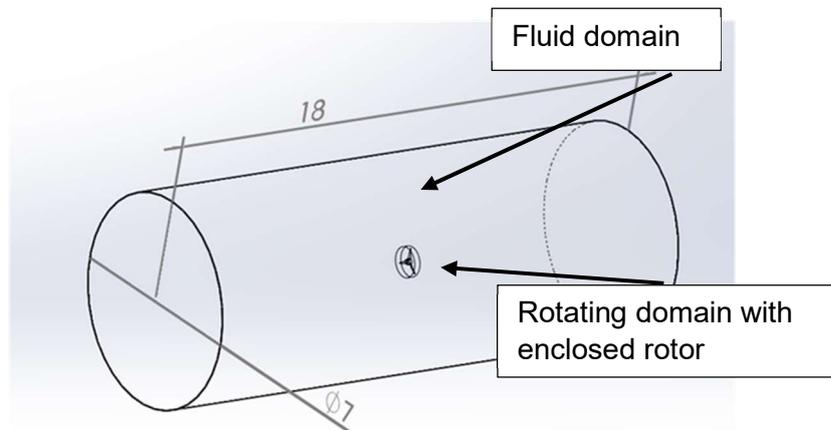


Figure 25. Full geometry for CFD simulation with dimensions in metre.

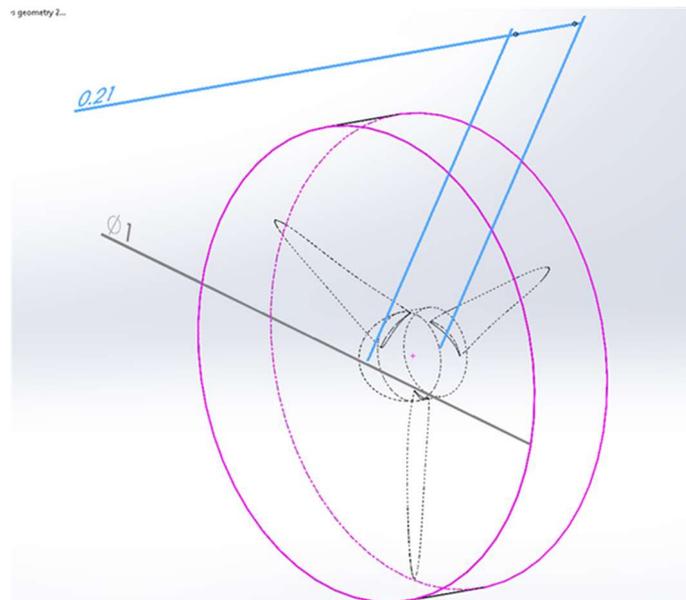


Figure 26. Rotor within rotating domain with dimensions of 1 m diameter and length of 0.21 m.

Rotational periodic boundaries were used for CFD simulation, which greatly reduces the computational resources required for CFD analysis. The solid model was split longitudinally into three identical 120-degree 'slices' and only one of the slices was imported into ANSYS for the flow simulation. Figure 27 displays the model after the 120-degree cut.

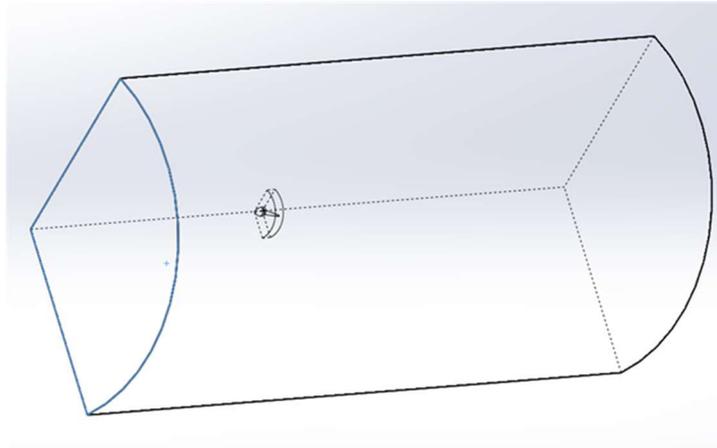


Figure 27. Rotational periodic boundary at 120 degrees.

Solid modelling for manufacturing purposes for all rotors followed similar procedure, but modelling excluded the rotating domain and fluid domain. The blade and hub modelling followed the same method as for the simulation model. Additional cuts, extrusion and location geometry were modelled on the blade and hub for the manufacturing of the rotors. Solid models for manufacturing were done with three parts namely the blade, hub and hub cap. The three solid parts for assembly are shown in Figure 28 to Figure 30.

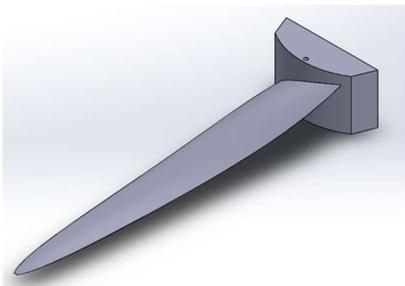


Figure 28. Blade section.

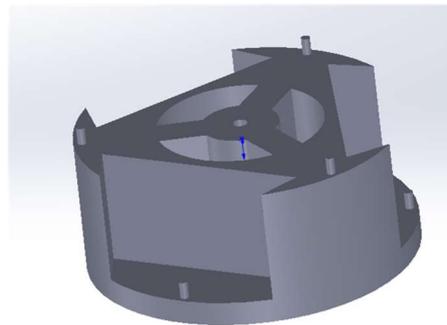


Figure 29. Hub base section.

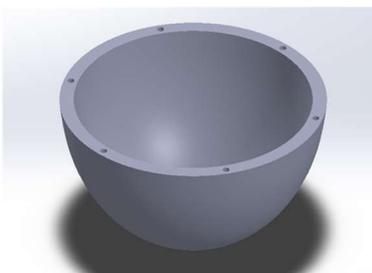


Figure 30. Hub cap section.

### 3.3 CFD simulation

CFD simulation was done with ANSYS Fluent R1 software. Each rotor was simulated separately. Fluent has six basic steps as shown in Figure 31.

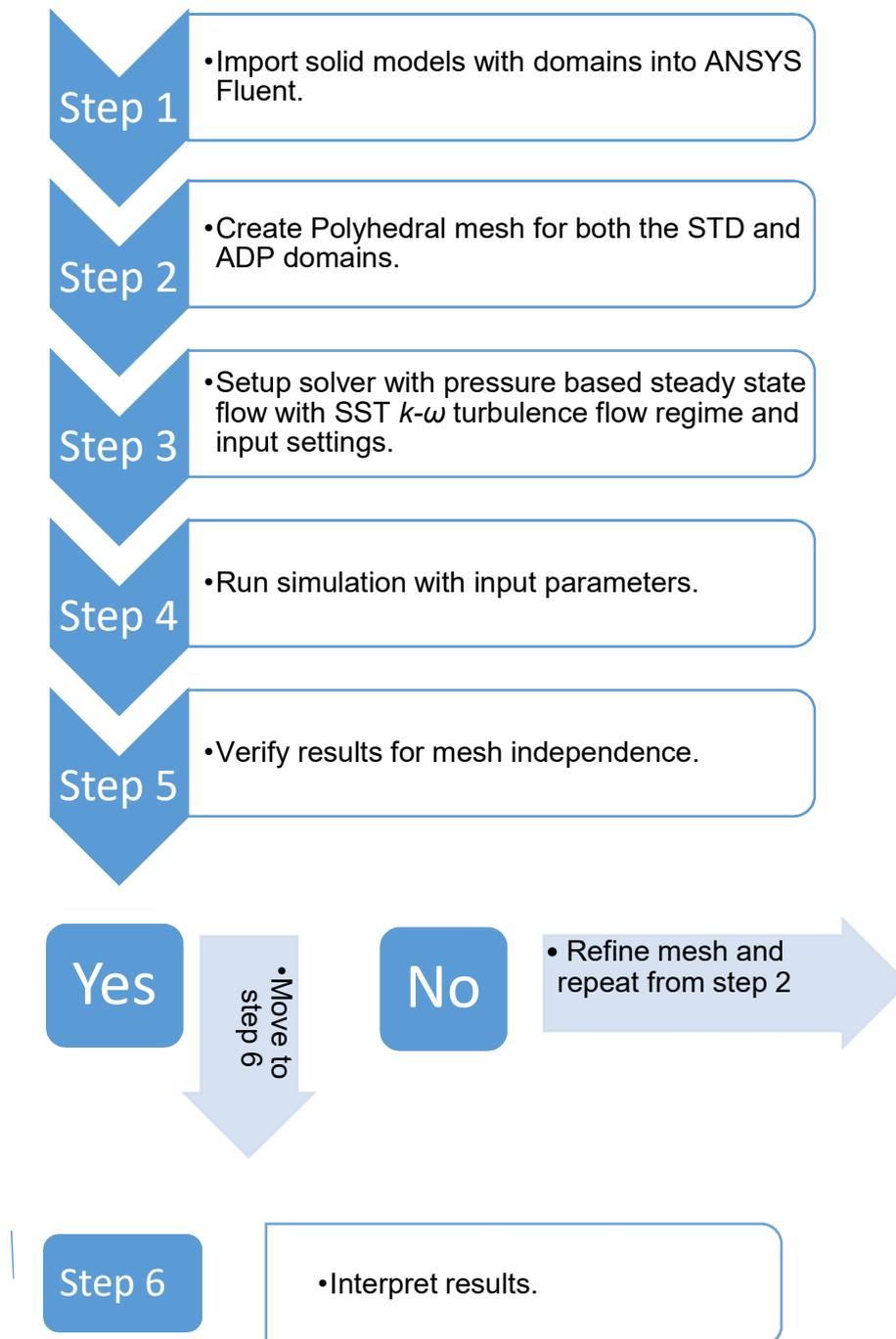


Figure 31. Flow chart of CFD steps.

The solid model was first converted to an importable format for Fluent software. After import, the solid model was meshed into smaller control volumes. Solver settings were chosen, including a pressure-based steady state flow and the SST  $k-\omega$  turbulence flow regime. The simulation was initiated, and results were verified for mesh independence. If mesh independence was not reached the mesh was refined and the simulation was repeated from Step 2. If mesh independence was reached the results of the simulation were interpreted. A complete step by step procedure, including all mesh and solver settings for this study, was developed and is attached in Appendix 7.2. The purpose of the CFD procedure was to enable reproduction of results and act as a guide for similar future simulations.

### **3.3.1 Mesh**

Once the rotor solid model was imported into the simulation software the model had to undergo the meshing process. How meshing was done was of importance in order to capture the boundary layer - including the laminar sublayer created at near-wall conditions. As previously mentioned in section 2.5.5 the mesh or control volumes had to be finer or smaller than the present laminar sublayer in the flow system. The Polyhedral mesh was chosen for the solid models. Oaks and Paoletti (2000) recommend the use of a polyhedral mesh for complex models resulting with significant details of the model being preserved. They also recommended quality improvement-based smoothing during volume meshing. Three mesh regions were created namely: the fluid domain, the rotating domain and the rotor domain. Each mesh region had different mesh sizes due to the nature of the region. The fluid domain boundary was wall type with a velocity inlet upstream of the rotating domain and a pressure outlet downstream of the rotating domain. The boundary condition for the rotating disc was selected as interior to enable fluid flow through the domain with the rotor as wall type boundary. The rotor domain had surface mesh only as no heat transfer or deformation of the rotor were included in this study.

Regions with large volumes like the fluid domain used larger elements compared to the regions which were crucial for capturing the boundary layer and complex geometry - for example where the root of the blade intersects with the hub. Meshing sizes and the quantity of total elements influenced the simulation results, the simulation time and the computational power required. The available computational power influenced the choice in meshing. Figure 32 shows the meshed model including the fluid domain. A zoomed-in section of the hub and root of the blade in Figure 33 shows that the element sizes around them are much smaller than elements elsewhere in the fluid domain. A further zoomed in section at the root of the blade with trailing edge, displays even finer mesh where the geometry had significant details and where the laminar sublayers needed to be solved correctly.

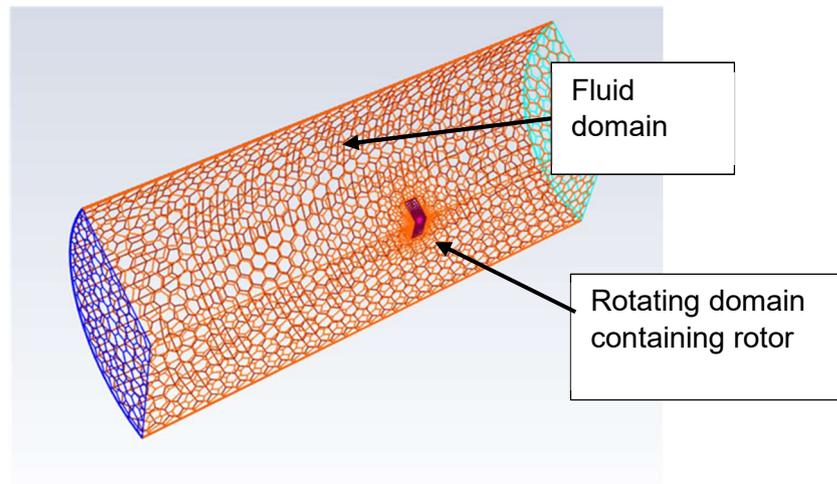


Figure 32. Complete meshed model including rotor, rotating and fluid domain.

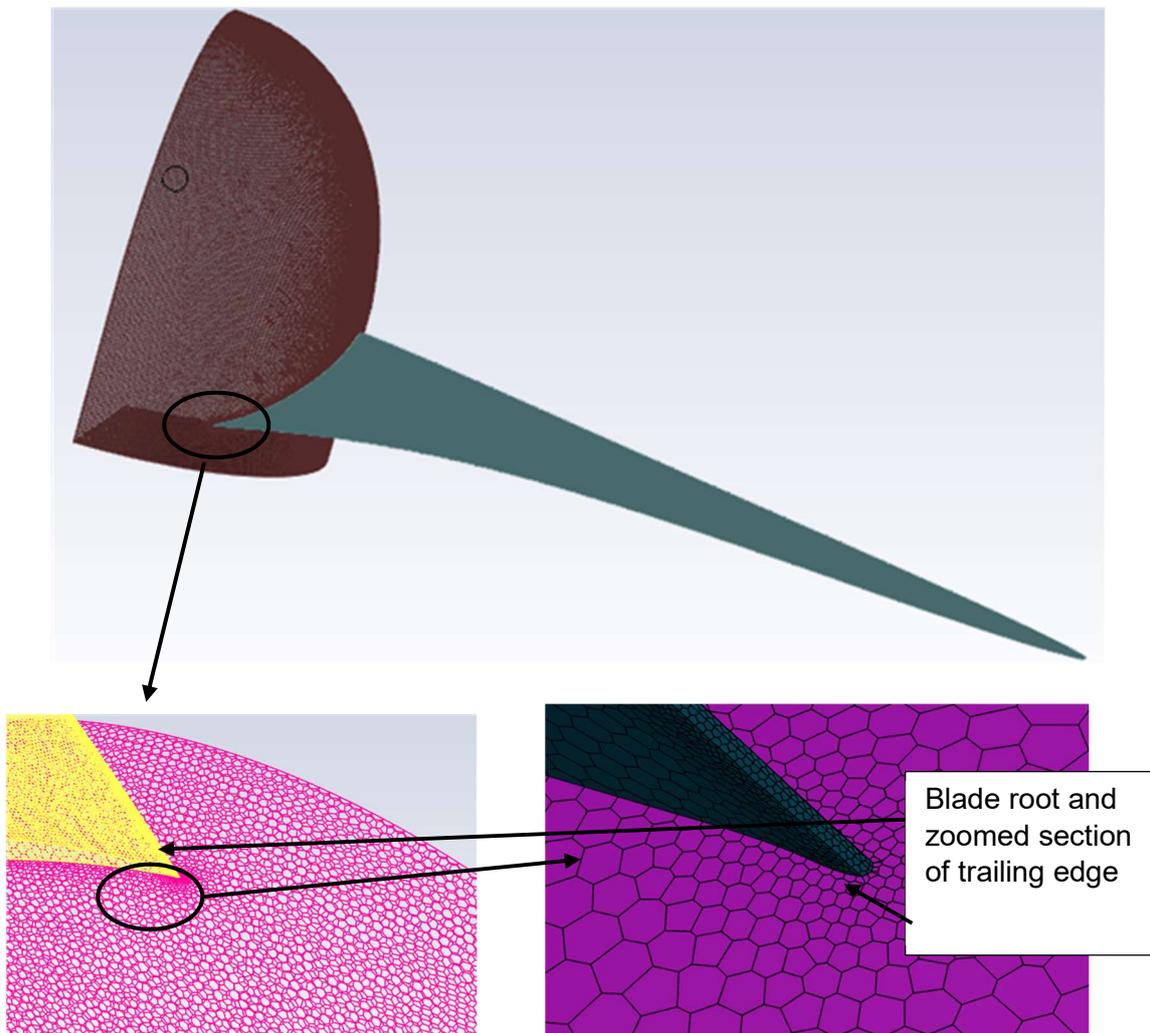


Figure 33. Hub with blade with zoomed in section of hub and root of blade (left picture) and zoomed in section of blade root of the trailing edge (right picture).

### 3.3.2 Mesh independence

The model that was simulated had to satisfy mesh independence with small residuals during convergence. An acceptable residual for this study was a value that was within the measuring precision of physical testing. Table 4 shows the steps and final mesh information for mesh independence. The mechanical torque generated by the rotor was used as the independence factor as previously outlined.

Table 4. Mesh independence steps and results.

<b>Step 1 Mesh information</b>	
Mesh Shape	Polyhedral
Number of Nodes	11 970 693
Number of Elements	4 770 993
N-m	<b>0.28</b>

<b>Step 2 Mesh information</b>	
Mesh Shape	Polyhedral
Number of Nodes	12 758 773
Number of Elements	5 058 260
N-m	<b>0.27</b>

<b>Final Mesh information</b>	
Mesh Shape	Polyhedral
Number of Nodes	12 955 303
Number of Elements	5 129 603
N-m	<b>0.27</b>

Final mesh type and quantity for both the STD and ADP rotors are tabulated in Table 5. Both rotor models were meshed with the blade local target mesh size of 0.42 mm, hub target mesh size of 1.42 mm with 0.1 mm as minimum mesh size restriction. The maximum mesh size restriction was 425 mm which was mainly applicable for the large fluid domain volume. To create mesh within the boundary layer, mesh inflation using aspect ratio was used. Boundary layer mesh included 4 layers at an aspect ratio of 1.2. The difference in quantities in the element count and nodes were due to the blade geometry differences.

Table 5. Final meshing statistics for STD and ADP rotors.

<b>Mesh information for STD rotor</b>	
Mesh Shape	Polyhedral
Number of Nodes	12 955 303
Number of Elements	5 129 603
<b>Mesh information for ADP rotor</b>	
Mesh Shape	Polyhedral
Number of Nodes	13 396 619
Number of Elements	5 299 443

The mesh independence for this study was reached at element quantities of 5 129 603 for the STD and 5 299 443 for the ADP. The increased number of elements was influenced by the slight geometry differences of the rotors. Table 6 displays the final mesh quality for both the STD and ADP simulation models.

Table 6. Final meshing quality for STD and ADP rotors.

<b>Mesh quality for STD mesh</b>			
		At cell number	On Zone
Minimum orthogonal quality	0.07	4 914 939	361
Maximum aspect ratio	230	3 318 400	361
<b>Mesh quality for ADP mesh</b>			
		At cell number	On Zone
Minimum orthogonal quality	0.04	5 092 898	198
Maximum aspect ratio	235	5 091 025	198

### 3.3.3 Solution solver

The solution solver requires input for the simulation. The simulation for this research used a pressure-based solver with absolute velocity formulation and steady state. Pressure-based was chosen as the density remained constant for the working fluid which was air. Table 7 shows the working fluid constants used in the simulation.

Table 7. Solution solver constants.

<b>Solution Solver Constants</b>	
Air Density kg/m <sup>3</sup>	1.225
Air Viscosity kg/m-s	1.79E-05
Operating Pressure kPa	101.325

The turbulence model chosen for simulation was the SST  $k-\omega$  with low Reynolds number correction. The SST  $k-\omega$  model allowed the simulation to use the  $k-\epsilon$  transport equation in the freestream section and the  $k-\omega$  transport equations for near-wall sections where small turbulent eddy currents were present. The low Reynolds number correction allowed the damping of turbulent kinetic energy where the Reynolds number is very low. Both these transport equation were solved with RANS equation number (18) by the solver. Initial inputs provided for this research are in Table 8 below.

Table 8. Initial CFD inputs.

<b>Initial inputs for CFD simulation</b>	
Tip Speed Ratio	4
Rotational speed	800 rpm
Wind Speed	6 m/s
Blockage Factor	0.06%

The low blockage factor meant that no blockage correction was necessary. Simulations were performed over a range of rotor rotational speeds. The simulations and physical tests assumed 3D flow where the BEMM did not. The incremental rotational speed and power outputs were plotted against each other for both the STD and ADP rotors. A third-degree polynomial best fit line was fitted to the simulation results. The equation of the polynomial was used to determine the rotational speed corresponding to the peak power output. The outcome of simulations was mainly focussed on the power generated to compare the performance increase of the ADP rotor versus the STD rotor. Axial velocity contours were also visualised.

### **3.3.4 CFD-Post**

ANSYS, CFD-Post 2019 R1 software was used to interpret the simulation results. The software allows visualization of velocity contours, which were exported to spreadsheet software for further processing and presentation.

Visualization of velocity contours provided a better understanding of flow through the rotors and confirmed simulation correctness and acceptability. CFD simulation and physical test results were compared. The simulation peak power output was compared with peak power

measured during physical testing. Simulation power output was calculated from simulation torque output and rotational speed using Equation 22 (noting that the multiplier of three is required due to the use of rotational periodic boundaries).

$$P_{tor} = 3 \times T \times rpm \times 2 \pi / 60 \quad (22)$$

$P_{tor}$  – Power generated by torque

$T$  – Torque

$rpm$  – Revolutions per minute

### 3.4 Testing

Physical testing was done to validate the simulation models for both the STD and ADP rotors. Each rotor was tested individually at a constant wind speed of 6 m/s. At different loads, the rotational speed and output power were recorded. The power output of the rotors was converted to power coefficients using Equation 23.

$$C_p = \frac{P_o}{0.5 \rho V_o^3 A} \quad (23)$$

$C_p$  – Power coefficient

$P_o$  – Power output

$\rho$  – Density

$A$  – Rotor area

$V_o$  – Wind speed

Power coefficients versus rotational speed curves were plotted for each rotor. The simulation power outputs were also converted to power coefficients to compare the results as the simulation and physical testing were done at different temperatures influencing the density of air. The setup and instrumentation for the physical test were important to get the best agreement between the tests and simulation by minimising accuracy errors. The test rig was designed to minimise flow interference from the ground and vehicle flow displacement. The mounting pole and tail of the test rig were designed to be as far away as possible from the rotor plane to minimize tower and wake' interference.

#### 3.4.1 Setup

The test rig was designed to be used on the back of a light delivery vehicle (LDV) or on a trailer. Figure 34 shows the rotor assembly with generator and tail. This assembly was manufactured from aluminium to reduce total weight and fits on top of the mounting pole with a yaw bearing. As shown, the rotor was placed as far as possible from the tail and mounting pole to minimize interference with the wake formed behind the rotor. The rotor was placed 800

mm in front of the mounting pole and with 2 m high clearance from the vehicle for minimum interference from pole and vehicle.

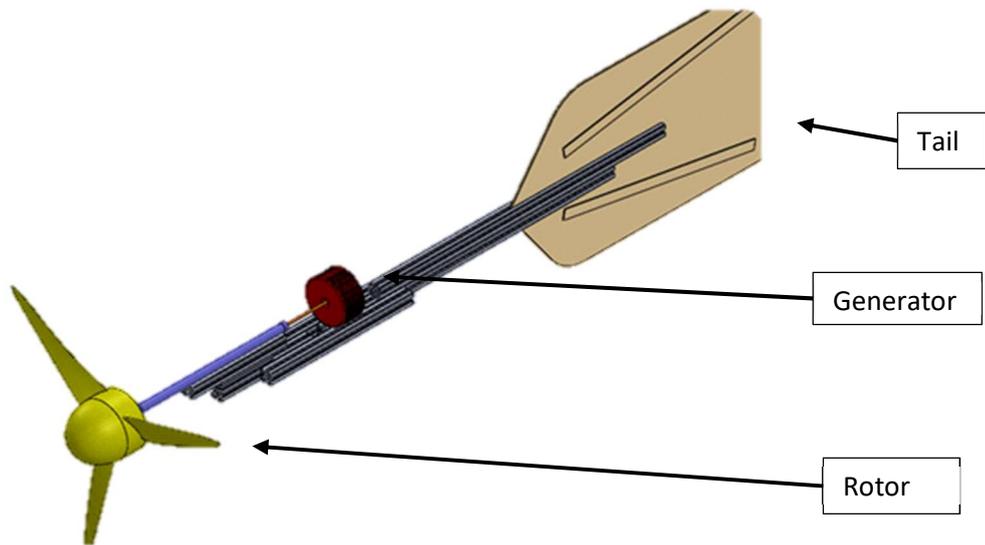


Figure 34. Rotor with generator, tail and subassembly.

Figure 35 shows the complete test rig with mounting poles, base frame, rotor subassembly and additional mounting pole for the anemometer.

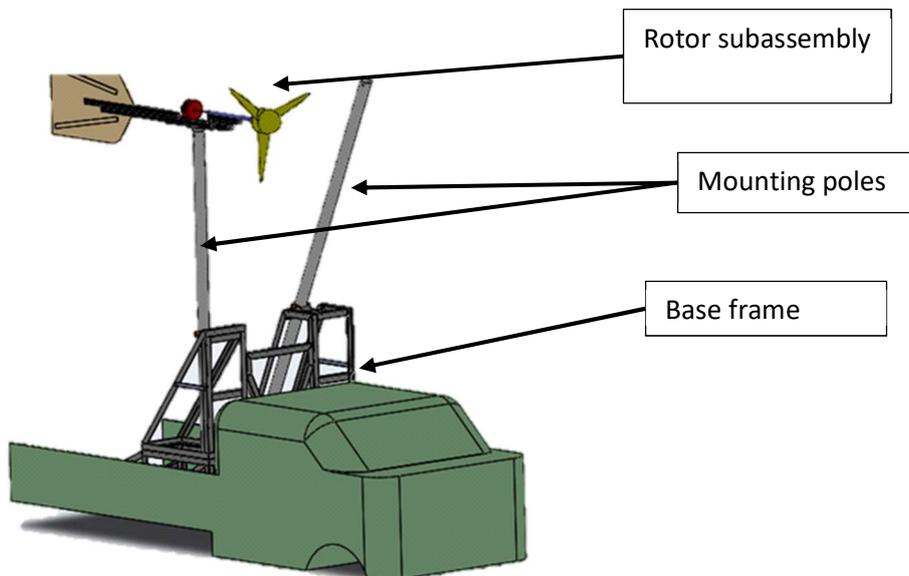


Figure 35. Illustration of test rig on back of LDV.

The test rig consisted of:

- Rotor subassembly.
  - Rotor
  - 400 Watt rated 3-phase generators
  - Aluminium frame
  - tail
  - Yaw bearing
- Mounting pole for rotor subassembly.
- Mounting pole for anemometer.
- Base frame.

The placement of the instrumentation is shown in Figure 36. The list of instrumentation used during the field test was:

- Anemometer to measure wind speed.
- Resistor bank with resistors connected in parallel for generator loading. Figure 37;
- Two Arduino Uno boards with LM393 infrared sensor modules and LCD displays. Figure 38;
- 3-phase rectifier for DC power delivery from 3-phase permanent magnet generator.
- DT80 Data taker logger.
- Laptop.

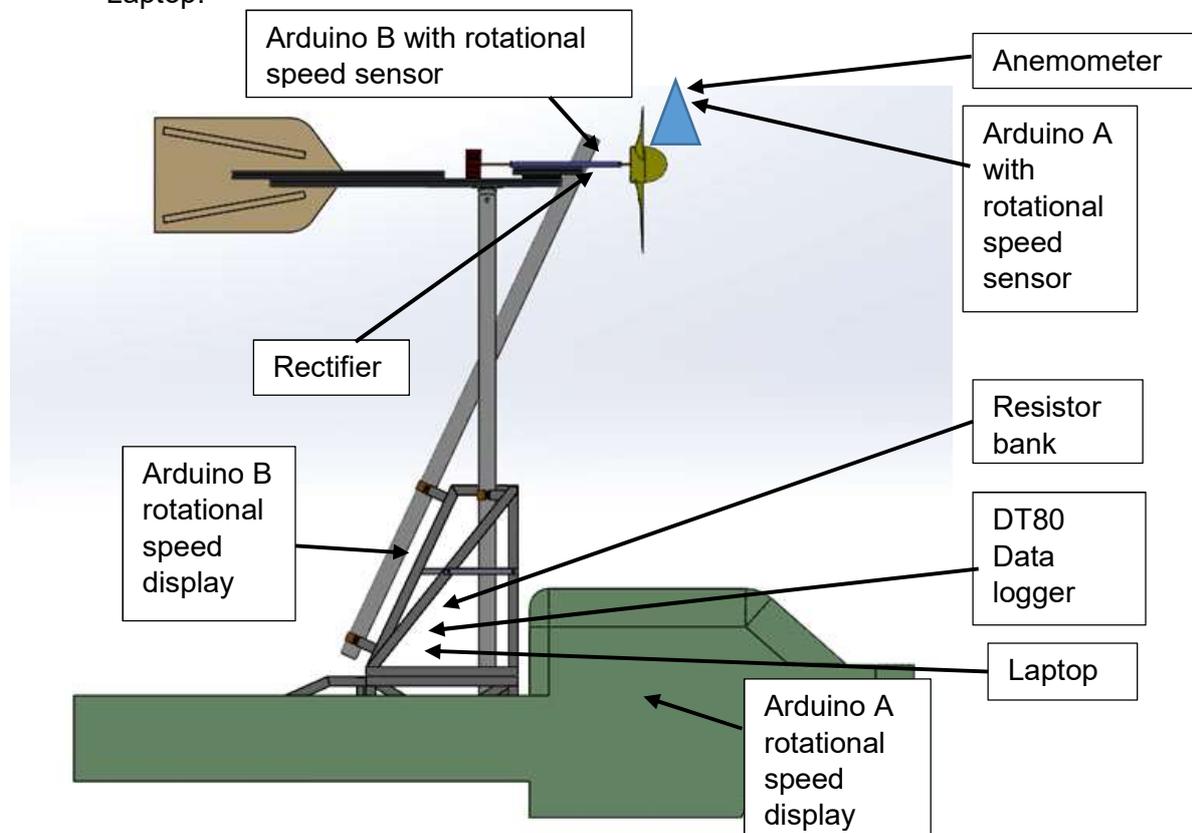


Figure 36. Side view of test rig with instrumentation positioning.



Figure 37. Resister bank.

### 3.4.2 Instrumentation

LM393 infrared sensors were used to measure the shaft rotational speed of the anemometer and the rotor shaft. The LM393 sensors were connected to an Arduino containing the software to measure the rotational speed. The rotational speed of the anemometer and rotor shaft were displayed in real-time on separate liquid crystal displays (LCD's). The rotational speed value for the wind speed anemometer was displayed inside the LDV for the driver to see and to able to control the velocity of the vehicle to maintain the correct test wind speed. Rotor shaft rotational speed was displayed on the test rig for test technician to see. Figure 38 shows the sensor, LCD display and Arduino board used.



Figure 38. LM393 sensor (left), LCD screen (centre) and Arduino Uno (right) (*Electro Peak*, no date, <https://electropeak.com/> [2020])

The rectifier was used to convert the generator 3-phase output into direct current (DC). From the generator, DC voltage was measured across the parallel resistor bank and DC current was measured via the internal shunt of the logging device. The resistor bank in Figure 37 consisted of two 10 Ohm and seven 100 Ohm resistors – all connected in parallel. This electrical load

was used to control the rotational speed of the rotor during the 6 m/s wind speed test. All measured data was captured and recorded using a DT 80 data logger.

### 3.4.3 Instrument calibration

Calibration of the instruments used during the field test was done at CPUT's fluid mechanics laboratory. The field test anemometer was tested inside a wind tunnel and connected to the rotational speed sensor and LCD display. The wind speed inside the tunnel was measured by a digital pitot tube anemometer (Extech) and the rotational speed of the field anemometer was recorded. This was done for a range of different wind speeds. Wind speed versus rotational speed was plotted to find the relationship shown in Figure 39.

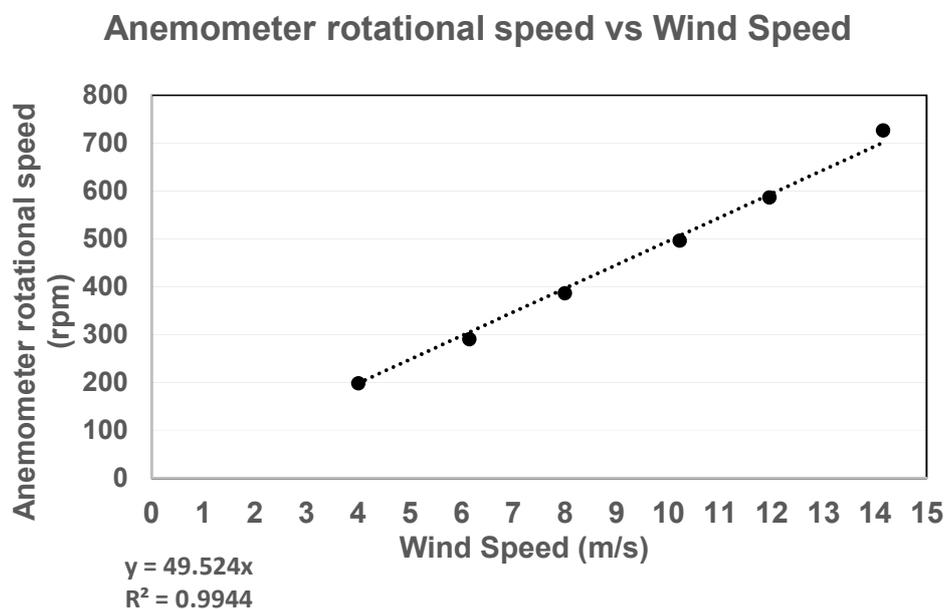


Figure 39. Anemometer calibration graph with rotational speed versus wind speed.

The equation  $y = 49.524x$  of the linear trend line was used to determine the rotational speed related to the test wind speed of 6 m/s which was 297 rpm.

The calibration of the rotor shaft rotational speed followed a similar approach. The rotor was rotated at various constant speeds and the shaft rotational speed was measured with a digital tachometer. The readings from the digital tachometer were plotted versus the rotational speed readings from the LM393 sensor on the rotor shaft shown in Figure 40.

### Tachometer rotational speed vs LM393 rotational speed for rotor shaft

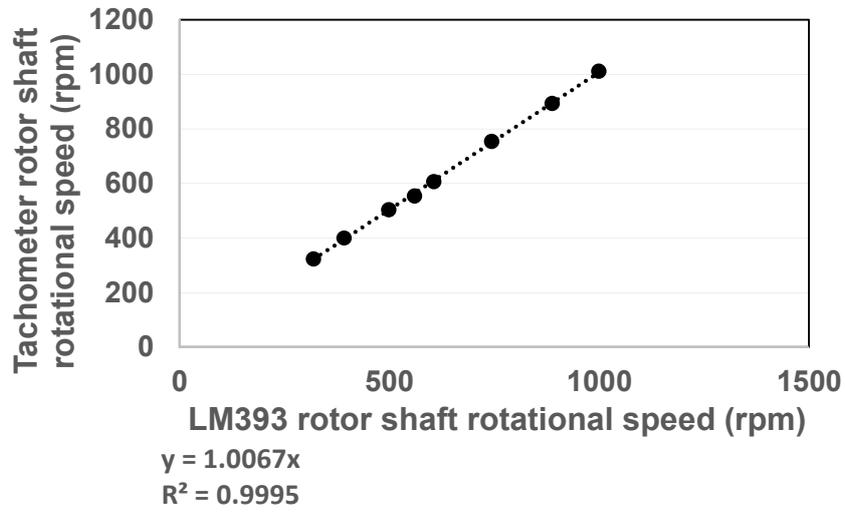


Figure 40. Rotor shaft rotational speed calibration graph.

The linear trend line equation  $y = 1.0067x$  was used to determine the correct rotational speed of the rotor compared to the output of the LM393 sensor on the rotor shaft.

## 4. Chapter Four: Results

### 4.1 CFD-Post results

Simulation results were interpreted in Post CFD. The main focus was to have CFD simulation results of power vs rotational speed that could be compared with the physical test and compare the STD versus the ADP rotor. Results from Post CFD were used to visualise the axial velocity profile and determine the actual induction factor for the rotors.

#### 4.1.1 Axial velocity contours

The axial velocity contours on a plane 15 mm upstream of the plane of rotation of the rotor was compared between the STD and ADP rotors. Figure 41 displays the axial velocity contours of one annulus across the 120° angle of rotor simulated. The axial velocity contours across the 120° rotational periodic section were found by adding the annulus sections across the span of the whole blade shown in Figure 42.

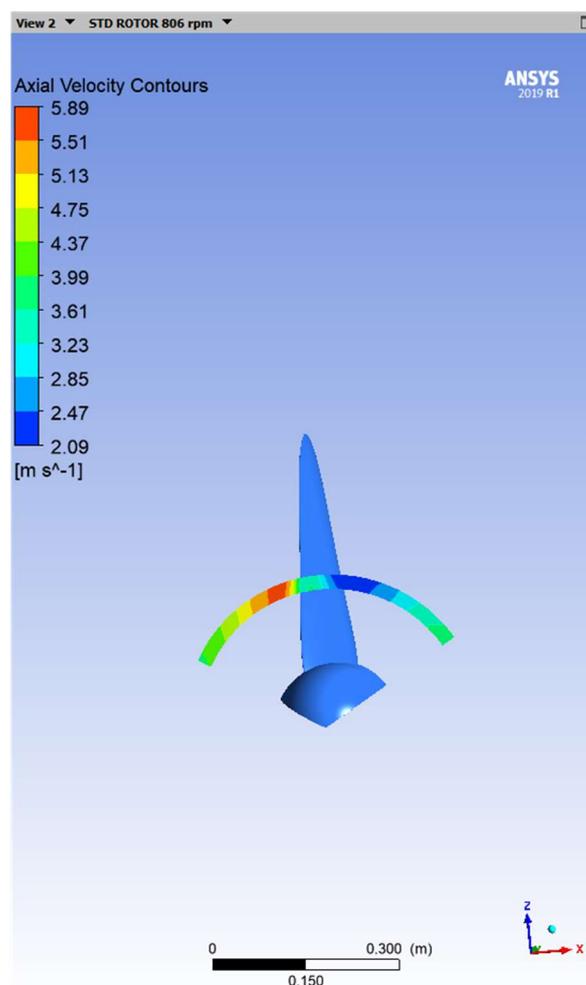


Figure 41. Sample of axial velocity profile on one annulus cross the rotor.

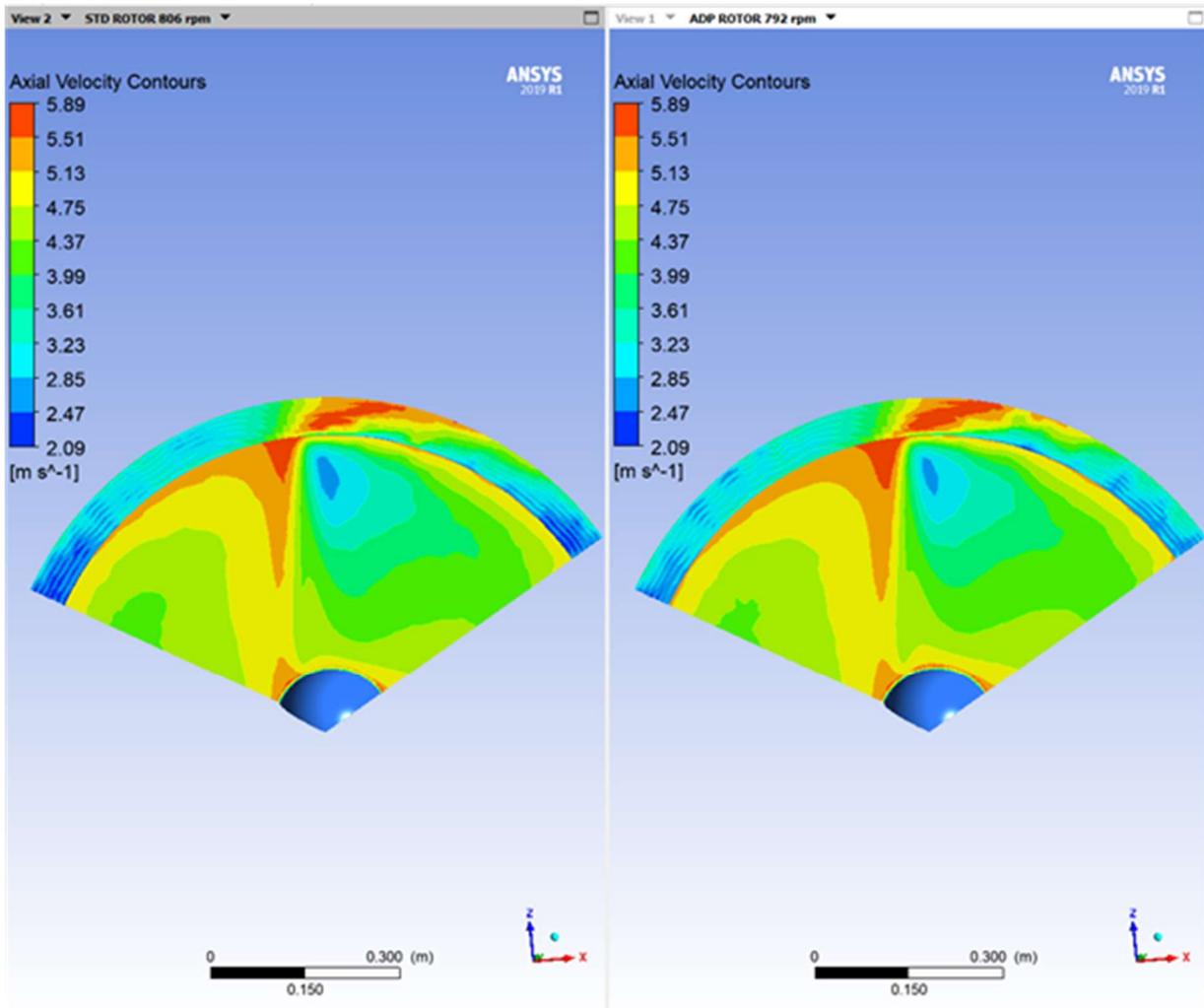


Figure 42. Axial velocity contours of rotational periodic section of rotor STD on left and ADP on right. Although the axial velocity contours for STD and ADP looked very similar, the average axial velocity results per individual annulus show some important differences. The average axial velocity per annulus were tabulated for both STD and ADP rotors. This enabled the determination of the axial induction factor per annulus (Equation 24).

$$a = (V_o - U_{ax}) / V_o \quad (24)$$

$a$  – Axial induction factor

$V_o$  – Wind speed

$U_{ax}$  - Average axial fluid velocity

The annulus sections in post CFD were sized to correspond with the blade element local radius location used in the BEMM design of the blade. The axial induction factor per blade element or section could be compared between the STD and ADP rotors. Figure 43 shows the graphical representation at respective peak power outputs. Note that annuli were analysed two-at-a-time near mid-span of the blade.

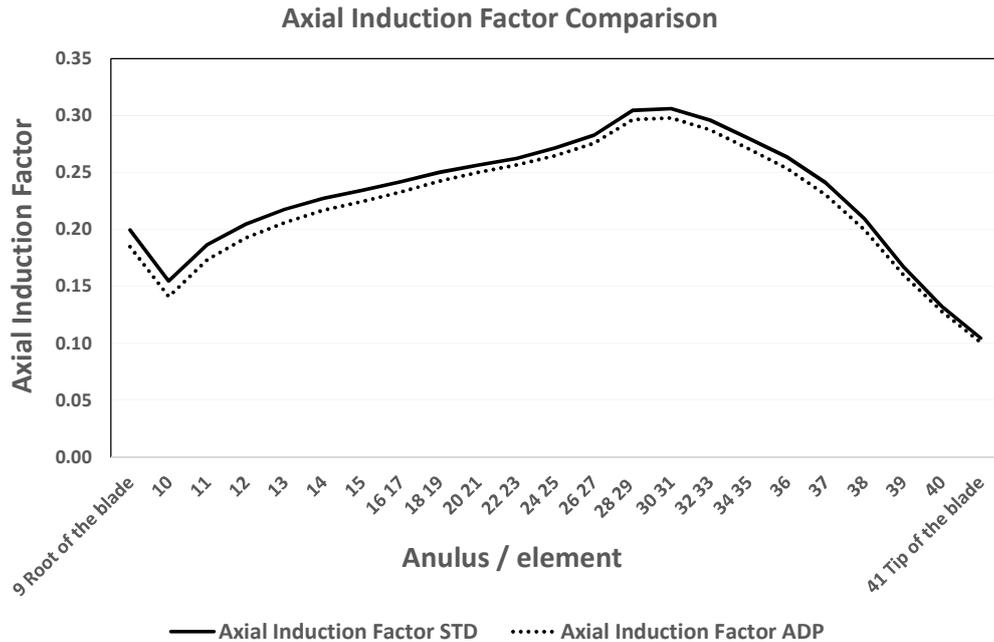


Figure 43. Graphical representation of axial induction factor for STD and ADP rotors.

When interpreting the results, we should note that the axial induction is proportional to the inverse of axial velocity. The shape of the curve across the blade revealed that wall friction on the hub decreased the axial velocity at the root with a sudden acceleration at the adjacent element 10. There was a gradual reduction of axial velocity from element 10 to element 33 which was influenced by radial velocity. An increase of axial velocity was observed from element 34 to the tip. The axial velocity magnitude change is also evident in the axial velocity contours in Figure 42. The difference between the STD and ADP curves indicated that the ADP rotor had slightly higher axial velocity across the blade. Figure 43 also shows that the ADP rotor had higher axial flow in the near-hub region when compared to the STD rotor.

#### 4.1.2 Power generated

The power generated by the STD and ADP rotors was calculated using the torque output values of the flow simulation using equation (22). The results of the rotational speed incremental inputs plotted against the associated power outputs for the STD rotor are shown in Figure 44.

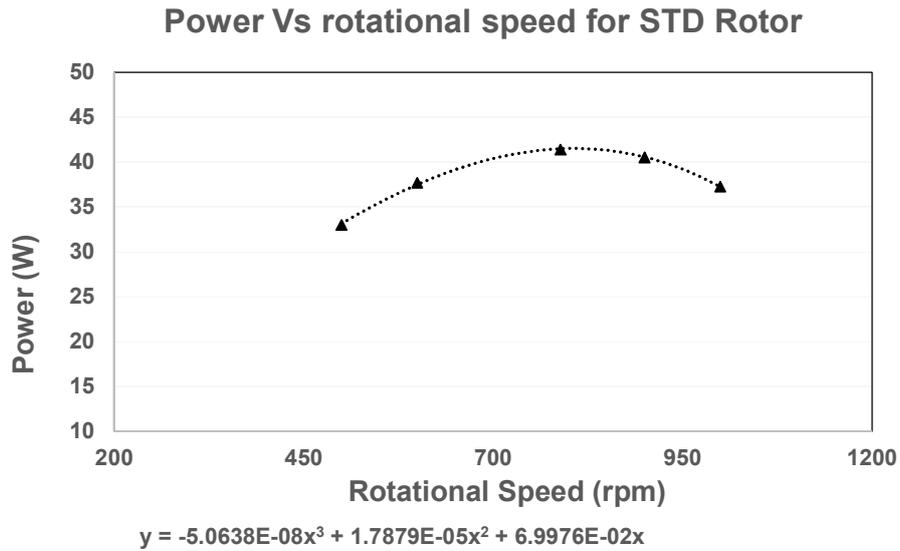


Figure 44. Rotational speed versus power scatter plot for STD rotor.

The equation of the polynomial was used to determine the rotational speed corresponding to the peak power output. The rotational speed for maximum power output of 41.50 W for the STD rotor was 806.51 rpm.

Similarly, the ADP rotor incremental rotational speed versus power is shown in Figure 45 and was used to determine at what rotational speed the peak power occurred.

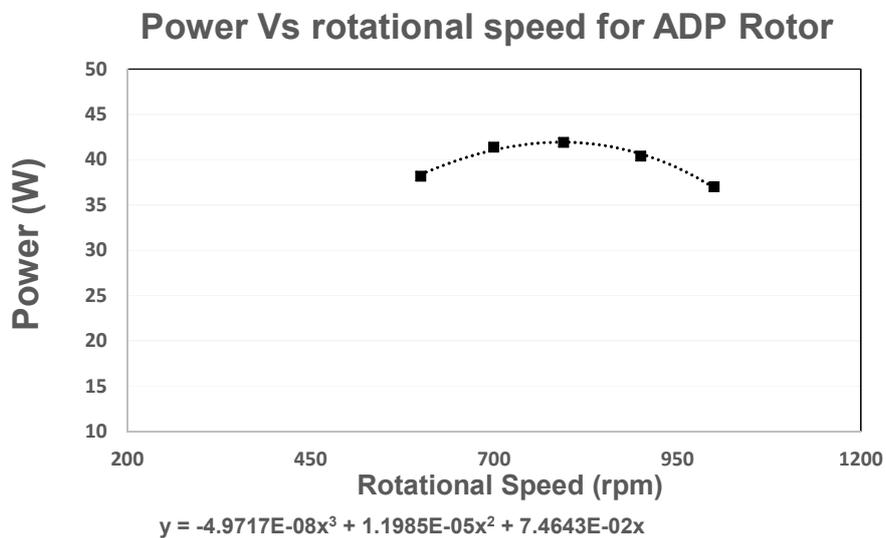


Figure 45. Rotational speed versus power scatter plot for ADP rotor.

Again, the equation of the polynomial was used to determine the rotational speed value corresponding with peak power output. The rotational speed value for peak power output of 41.94 W for the ADP rotor was 792.33 rpm.

The outcome of simulations was mainly focussed on the power generated to compare the performance increase of the ADP rotor versus the STD rotor. The polynomial models for the STD and ADP rotors predicted a performance increase of 1.06 % at the respective peak performance rotational speeds of 806.51 rpm for the STD and 792.33 rpm for the ADP.

Results for power generated are tabulated in Table 9 where the STD rotor generated 41.50 W and the ADP rotor 41.94 W at the optimum rotational speed determined in this section which was a 1.06 % increase in performance.

Table 9. Power generated by STD and ADP rotors.

<b>Power generated (W)</b>	
<b>STD</b>	<b>ADP</b>
41.50	41.94

### **4.1.3 Interpretation of results**

Overall axial velocity contours and averaged axial velocity per annulus results together provide a better understanding of why the subtle differences in chord and twist resulted in the ADP rotor outperforming the STD rotor. The tabulated results of the axial induction factor, derived from axial velocity contours for the ADP rotor, were slightly lower than the STD rotor – indicating an overall higher axial flow velocity through the ADP rotor. The higher axial velocity increases relative velocity, Reynolds number and lift/drag ratio - thereby increasing rotor output. The shape of the axial induction graph indicates that wall friction at the hub reduces the axial velocity at the root of the blade followed by a sudden increase of axial velocity until the element 10. This was followed by a gradual decrease in axial velocity to element 33 – due to higher radial velocity as a result of centrifugal force and displacement of air flowing around the relatively large hub. There was a steep increase of axial velocity from element 34 to the blade tip which coincides with the reduction of blade chord (and local solidity) to avoid excessive tip losses. The increase of performance of the ADP rotor was 1.06 % using the polynomial mathematical prediction models in section 4.1.2.

Simulated power curves versus rotational speed for both rotors using the best fit polynomial functions from section 4.1.2 were super imposed to visualise the performance as shown in Figure 46.

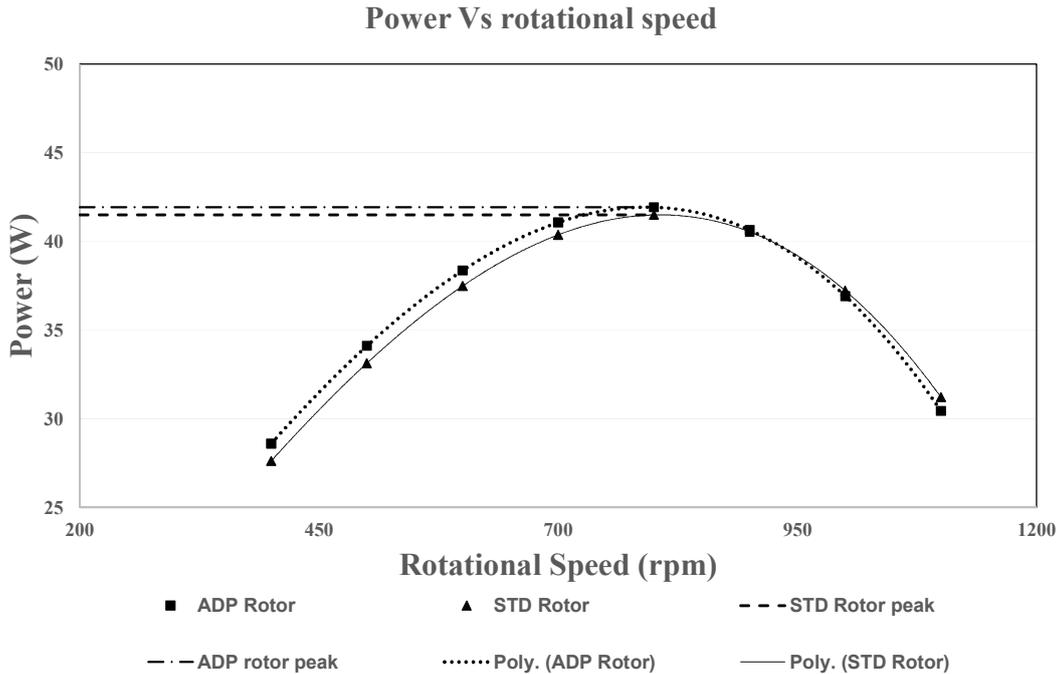


Figure 46. Super imposed Power versus Rotational speed for STD and ADP rotors.

The superimposed performance curves indicate that the ADP rotor has an increased performance at lower rotational speeds as well as at the respective peak performance rotational speeds. At higher rotational speeds the STD rotor performed slightly better. The ADP rotor peak performance of 41.94 W occurred at 792.33 rpm and the STD rotor peak performance was 41.50 W at 806.51 rpm. This was a 1.06 % increase of peak performance for the ADP rotor.

## 4.2 Vehicle-top mounted testing results

Vehicle-top testing was done on 17 September 2020 in the Overstrand area. The weather conditions were favourable with negligible wind and a temperature of 20 degrees Celsius. Testing was conducted using the wind turbine vehicle-top test rig mounted on a trailer. The test setup is shown in Figure 47 to Figure 49 . The section of road used for testing was on the R44. The section was a smooth straight tarmac road 2 kilometres long. The section of road is shown in Figure 50.



Figure 47. Trailer with complete test rig.

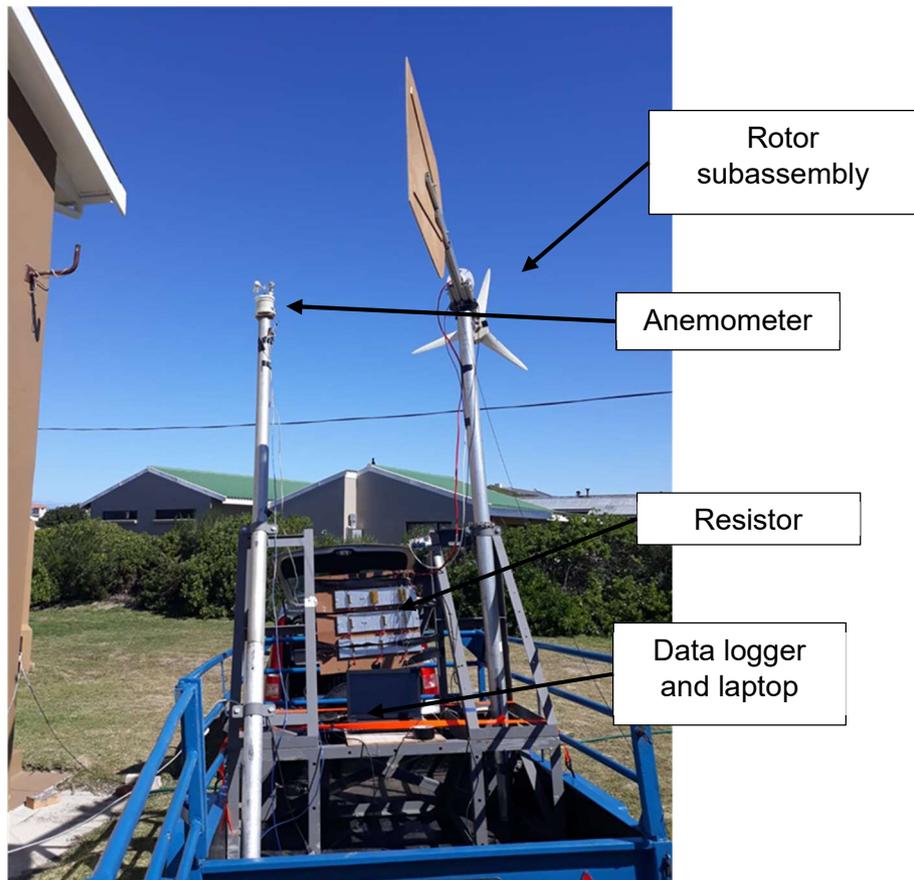


Figure 48. Back view of test rig on trailer.

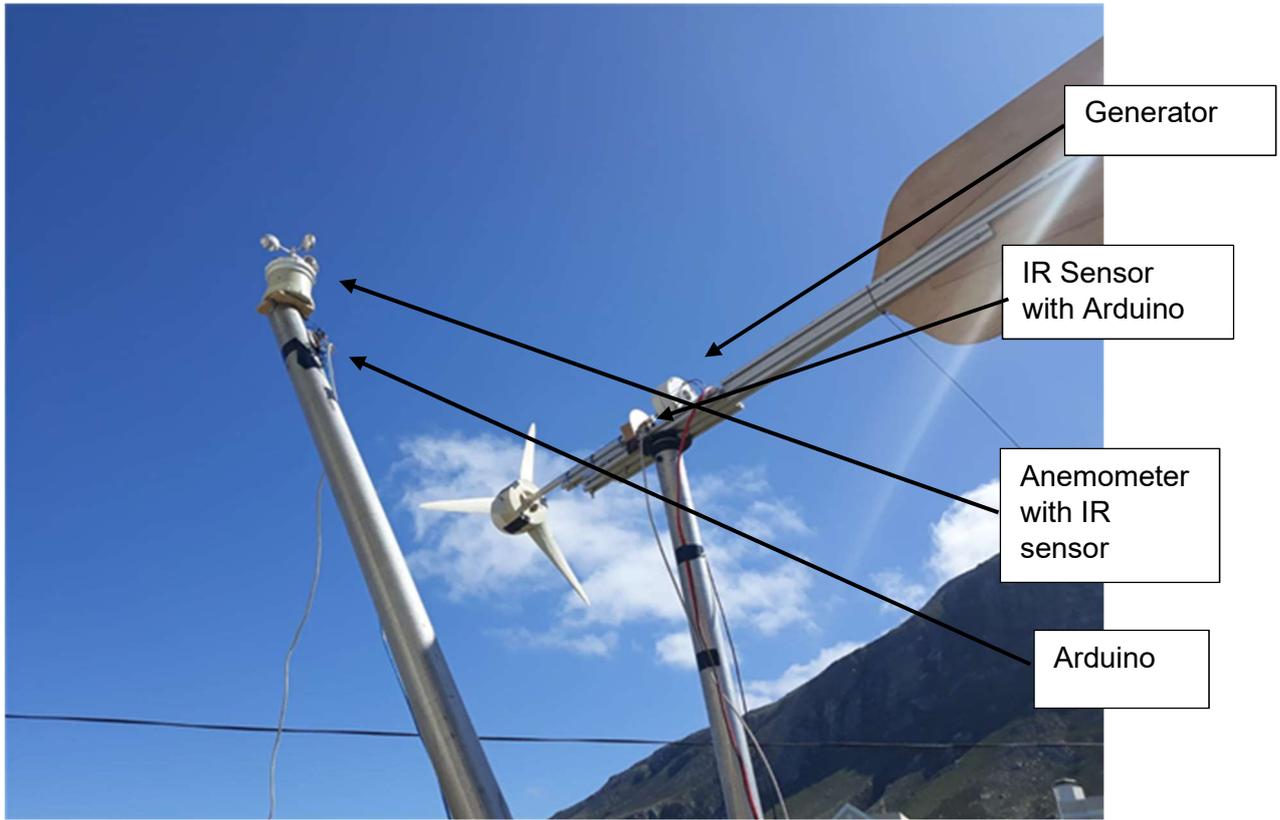


Figure 49. Anemometer on left and rotor subassembly on right.

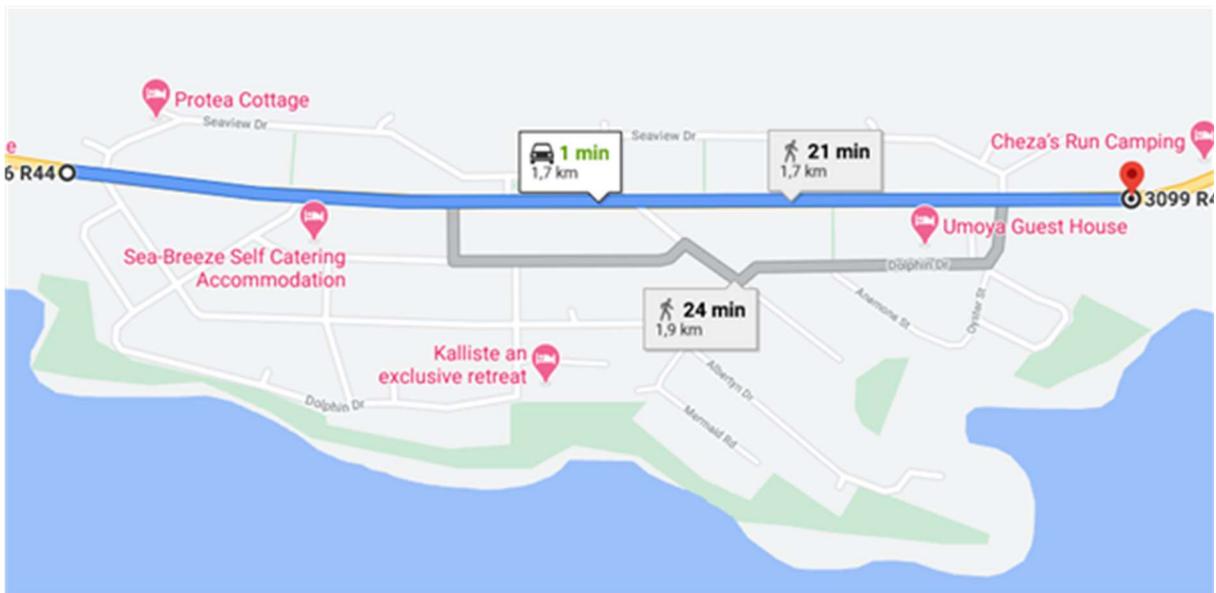


Figure 50. Section of road used on the R44, Betty's Bay. (2713-3466 R44, Betty's Bay, 7141 to 3099 R44, Betty's Bay, 7141 - Google Maps, nd, [2020])

During testing the relative wind speed was maintained within the range of 5.9 m/s and 6.1 m/s. The rotor rotational speed was controlled by adjusting electrical load on the resistor bank. Four streams of data were recorded during testing namely:

1. Rotational speed of the anemometer shaft relating to wind speed.
2. Rotational speed of the rotor shaft.
3. The voltage measurement across the positive and negative output terminal of the rectifier.
4. Measurement of the resistor values during testing.

The resistor bank was used to control the rotational speed of the rotor by changing the load from 200 ohms, 100 ohms, 50 ohms, 33.3 ohms, 20 ohms and 10 ohms. This meant that different rotational speeds of the rotor within the wind speed range of 5.9 m/s and 6.1 m/s could be recorded. This method was done for both the STD and ADP rotors.

Raw data recorded during testing was filtered to ensure that only the data within the 5.9 to 6.1 m/s wind speed range with related rotor rotational speed and voltage were used. All time stamps of the three data streams were synchronised. Data within the wind speed range at variable rotor rotational speeds with faulty readings were omitted from data sets. Faulty readings included acceleration / deceleration of rotor shaft rotational speed and low or non-recorded voltage reading. When faulty readings were identified all data relating to the faulty data time stamp were omitted across the data streams.

#### 4.2.1 Power generated

The power generated by the STD and ADP rotors was calculated using the voltage readings and resistor bank values at each rotational speed. Equation 25 was used to calculate generated power.

$$P_o = \frac{v_v^2}{r_r} \quad (25)$$

$P_o$  – Power output

$v_v$  – Measured voltage

$r_r$  – Measured resistance

Power generated was calculated for each data point and plotted against rotor rotational speed for the STD and ADP rotor. A third degree best-fit polynomial line was fitted to the data points for better visual representation of the field test results. Power versus the rotational speed for the STD rotor is shown in Figure 51.

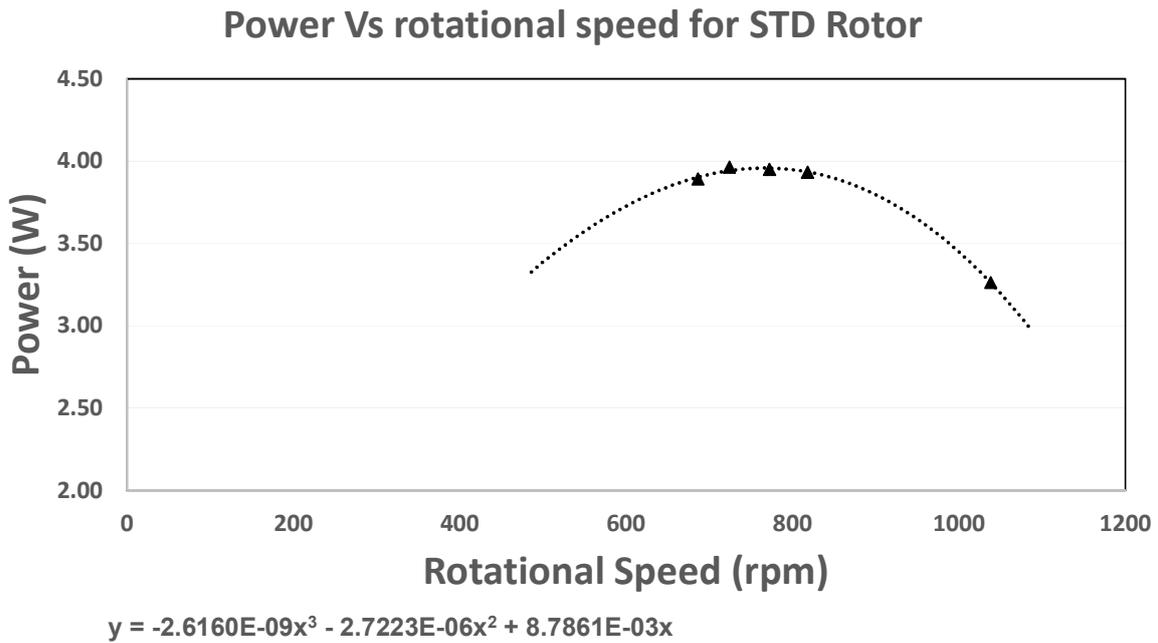


Figure 51. Power versus rotational speed for STD rotor.

The equation of the polynomial was used to determine the rotational speed value where the peak power output was for field testing. The rotational speed value for maximum power for the STD rotor was 766.61 rpm. The power generated at this maximum rotational speed was 3.96 W. Deviation range of raw data used for the STD rotor performance curve are shown in Table 10.

Table 10. Range of deviation for STD rotor field test.

<b>Range of deviation for STD rotor field test</b>			
<b>Rotational speed (rpm)</b>	<b>Power generated Used data (watts)</b>	<b>Minimum (watts)</b>	<b>Maximum (watts)</b>
1038	3.26	3.25	3.27
818	3.93	3.92	3.94
772	3.95	3.94	3.96
724	3.96	3.95	3.97
686	3.89	3.88	3.90

The same method was applied to the ADP rotor plotting the power versus the rotational speed shown in Figure 52.

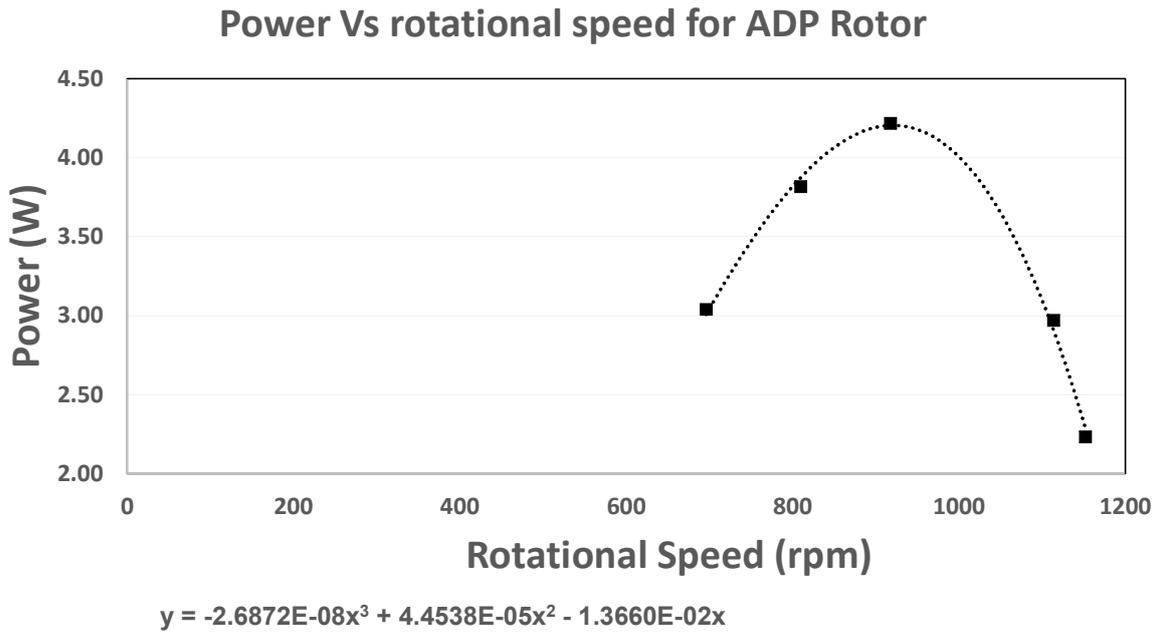


Figure 52. Power versus rotational speed for ADP rotor.

Using the polynomial equation for the ADP rotor the maximum rotational speed for peak power output was 920.94 rpm and the peak power at this rotation speed was 4.20 W. Deviation range of data for ADP rotor field test are shown in Table 11.

Table 11. Range of deviation for ADP rotor field test.

<b>Range of deviation for ADP rotor field test</b>			
<b>Rotational speed (rpm)</b>	<b>Power generated Used data (watts)</b>	<b>Minimum (watts)</b>	<b>Maximum (watts)</b>
1152	2.23	2.18	2.28
1114	2.97	2.92	3.02
918	4.22	4.17	4.27
810	3.82	3.77	3.87
696	3.04	2.99	3.09

The performance increase of the ADP rotor versus the STD rotor at the respective peak performance outputs was 6.06 % for the field test which was higher than the predicted 1.06 % for simulations.

#### **4.2.2 Comparative physical results**

To better understand and to compare the physical test results of the STD versus the ADP rotors their performance curves were superimposed and are shown in Figure 53.

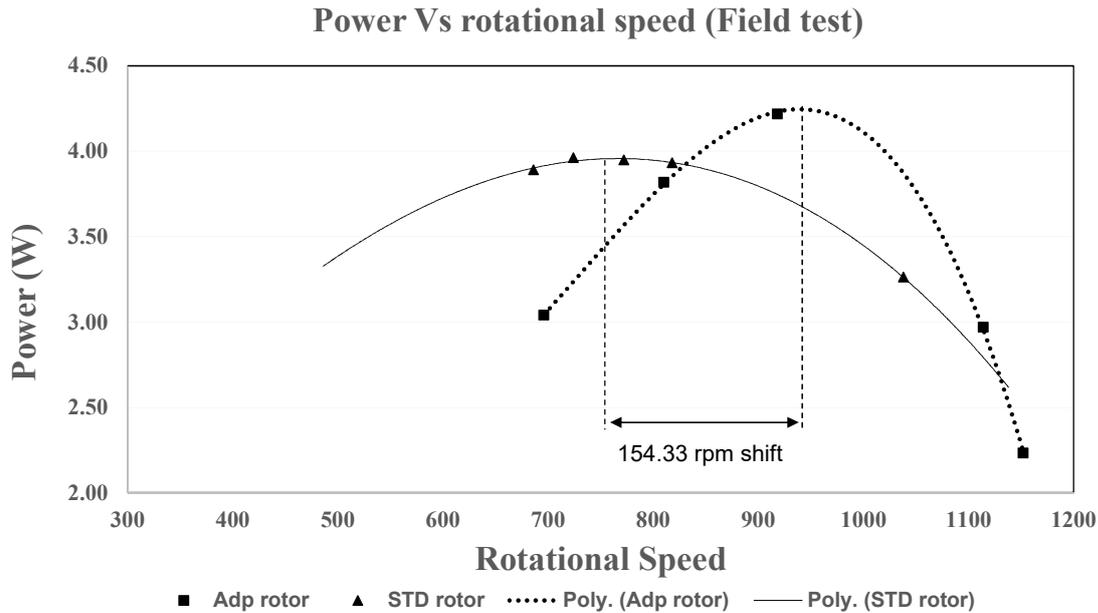


Figure 53. STD and ADP rotor performance curves super imposed.

Unlike the simulation prediction the STD rotor performed better at lower rotational speeds. The ADP rotor produced a higher peak power and this occurred at a higher rotational speed. It was noted that there was a difference in the projected and measured peak power rotational speeds (154.33 rpm) This is likely due to the turbulence model used being better matched to one of the blade geometries than the other for different speed regimes and the influence of flow over the vehicle. The peak power output for the STD rotor was 3.96 W at 766.61 rpm compared to the 4.20 W of the ADP rotor at 920.94 rpm - which was a 6.06% increase of power output.

### 4.2.3 Interpretation of results

Field tests were conducted at a different temperature to the simulations - which influenced the density or the working fluid. To overcome this difference of the working fluid and to allow comparison of simulation results with physical test results, the power vs rotational speed curves for simulation and field test were converted to power coefficient versus rotational speed. Equation (23) was used to convert each power data point to power coefficient at respective rotational speeds. Air density used during simulation was  $1.225 \text{ kg/m}^3$  and air density at 20 degrees Celsius at sea level was  $1.204 \text{ kg/m}^3$ . Due to losses during the field test (mainly due to the generator) there was a significant difference in  $C_p$  values between simulation and field test results. Therefore, the graphs were plotted with separate y-axis in order to compare the slopes and peak rotational speeds. Figure 54 shows the power coefficient of the STD rotor for the field test and the simulation superimposed.

### $C_p$ Vs rotational speed for STD Simulation and field test

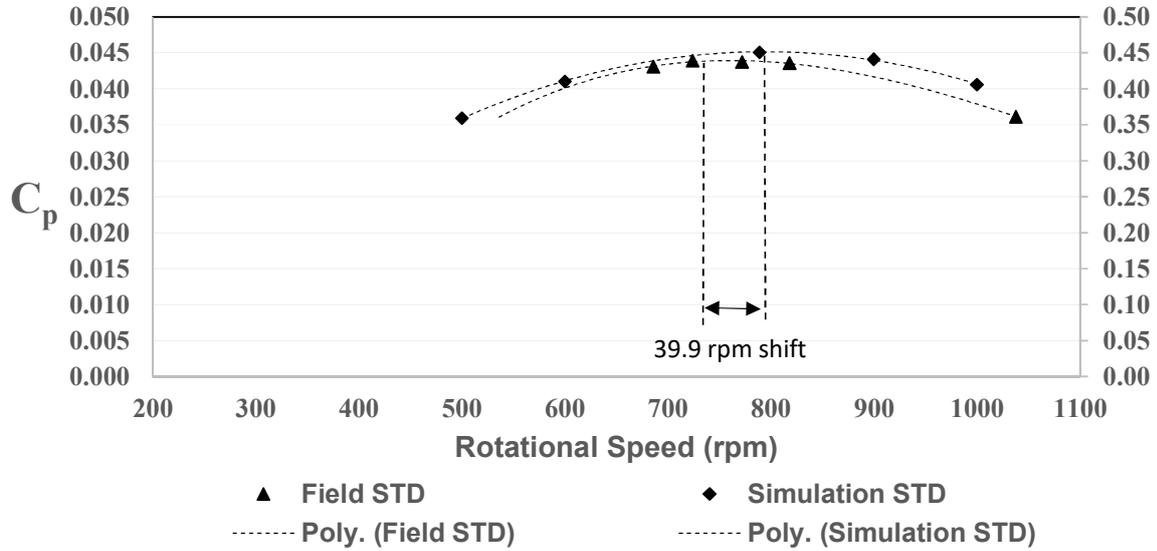


Figure 54.  $C_p$  versus rotational speed for STD rotor simulation and field test.

The power coefficient curves showed that the shape for the field test and simulation was very similar. It was also noticed that the peak performance rotational speed shifted with the simulation at 806.51 rpm and the field test that occurred at 766.61 rpm. It was noted that the peak performance rotational speed differed by 39.9 rpm between the CFD and field test results. There were significant differences between field and CFD  $C_p$  values probably due to the inefficiency of the overrated generator used during field testing. The expected power output from CFD was in the lower power range of the 400 W rated generator. Expected efficiency for 10% generator load for this generator was in the range of 10% as can be seen from the typical generator efficiency curve in Figure 55.

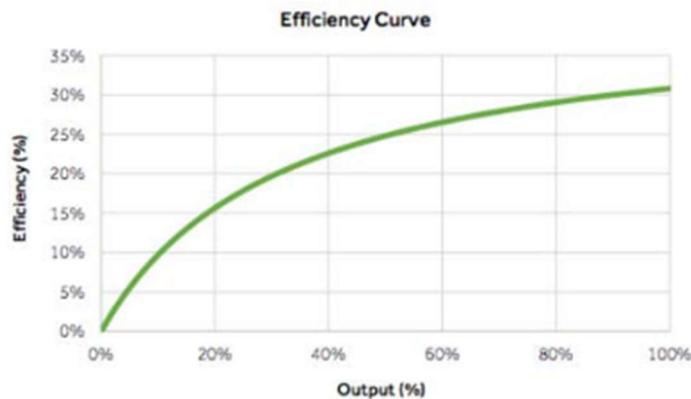


Figure 55. Typical generator efficiency versus load percentage. (Wheeler and Southward, 2017)

The power coefficient versus rotational speed curve for the ADP rotor are shown in Figure 56.

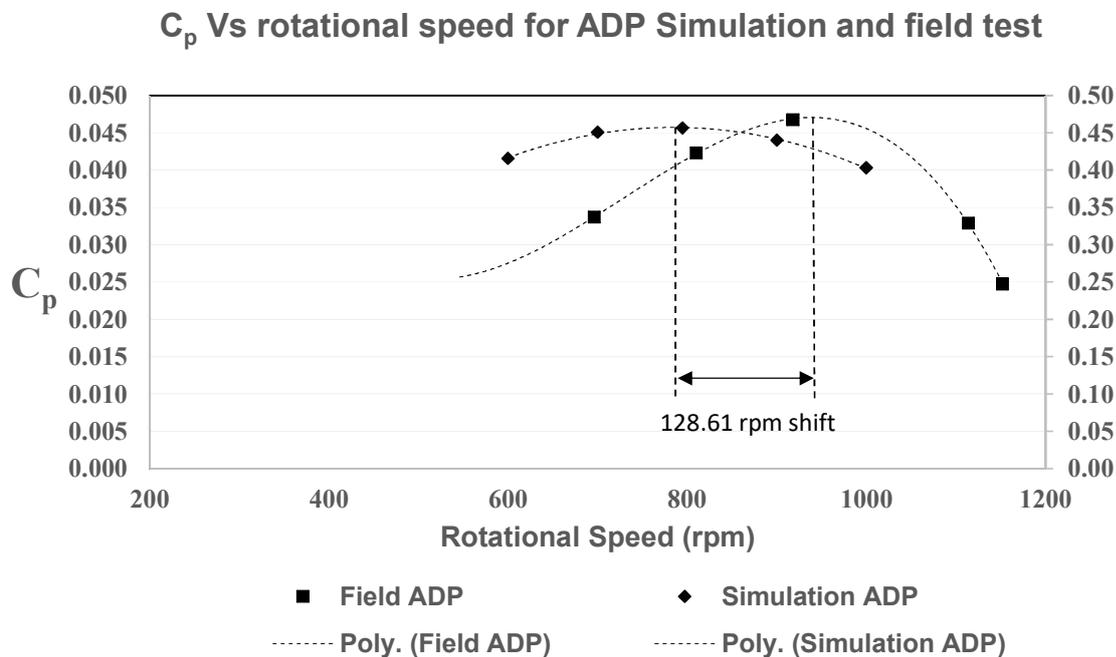


Figure 56.  $C_p$  versus rotational speed for ADP rotor simulation and field test.

The peak rotational speed for the ADP simulation was 792.33 rpm and during the field test it occurred at 920.94 rpm.

As with the STD comparison, the 128.61 rpm shift for the ADP could be explained by the same factors. Field test results also revealed lower  $C_p$  values at lower rotational speeds compared to the simulation.

The generator, mechanical and electrical losses on the test rig experienced during the field test for both the STD and ADP rotor were constant across both tests as no changes were made to the test rig mechanical, instrumental or electrical systems during the field test.

Both the STD and ADP rotors had a shift of peak performance rotational speeds compared to the simulation results. From this we can see that the CFD projected peak performance rotational speed might be significantly different to the actual peak performance rotational speed. This practically means that one can look at using CFD to improve rotor performance characteristics but not to design for a particular rotational speed for peak performance as this is not well predicted by CFD and needs to be determined by field testing or other empirical relations that may be developed by a manufacturer over time for particular wind turbine configurations.

The simulation and field test both showed a performance increase of the ADP rotor compared to the STD rotor. Predicted performance increase from simulation was lower than actual performance increase measured during field testing for the ADP rotor. Table 12 is a summary of simulation and field test results.

Table 12. Simulation and field test results and performance increase.

	<b>Simulation results</b>	
	<b>Peak rotational speed (rpm)</b>	<b>Predicted output (watts)</b>
STD rotor	806.51	41.50
ADP rotor	792.33	41.94
Simulation performance increase		1.06%
	<b>Field test results</b>	
	<b>Peak rotational speed (rpm)</b>	<b>Actual output (watts)</b>
STD rotor	766.61	3.96
ADP rotor	920.94	4.20
Field test performance increase		6.06%

Simulation power output was higher than the physical test power output due to the absence of flow interference and losses during simulation. The CFD simulation allowed an investigation of the axial velocity and induction across the STD and ADP blades and this showed a consistently higher axial velocity through the rotor, as well as a higher axial flow velocity in the hub region of the ADP rotor when compared to the STD rotor.

The main focus of this research was to simulate and test the performance of the ADP rotor versus the STD rotor at half the design wind speed. Simulations and physical tests both revealed an increased performance from the ADP rotor at peak power.

Power outputs from the STD and the ADP rotors during physical testing were within close range showing that both rotors would have experienced similar test rig losses during testing.

## **5. Chapter Five: Conclusion and recommendations**

### **5.1 Conclusion**

This research focussed on the performance of an adapted BEMM designed rotor, compared to a rotor designed using the conventional BEMM. Further research outputs were the solid modelling, manufacturing, simulation and physical testing of both the STD and ADP rotors. Procedures for the solid modelling and CFD simulation were included.

#### **5.1.1 Simulation**

Simulation results indicated that at half design wind speed of 6 m/s the ADP rotor had a higher peak performance than that of the conventional BEMM designed rotor. The simulation results for each rotor's peak performance rotational speed, the ADP rotor outperformed the STD rotor by 1.06 %. This performance increase occurred at respective peak performance rotational speed of 806.51 rpm for the STD and 792.33 rpm for the ADP rotor. During simulation of the rotors no flow interference, losses and vibration were included and the power output result were higher than the physical power output results where all these interference and losses were present. Axial flow velocity patterns and axial induction profile across the blades was visualised from simulation results and provided insight into the reasons for the performance improvement of the ADP blade. The axial induction factor across the blade of the ADP rotor showed how the ADP rotor had a consistently lower axial induction over the span of the blade. The axial flow velocity immediately upstream of the rotor showed a higher axial velocity in the near-hub region of the ADP rotor. The simulation visualizations suggest that higher flows in the near-hub region and more beneficial axial induction across the span of the blade (due to more effective blade design) were the reason for the increased performance of the ADP blade.

#### **5.1.2 Field test**

The vehicle-top test rig option was chosen over wind tunnel testing mainly due to funding limitations and the lack of an adequately sized wind tunnel in South Africa which can be used without any blockage factor correction.

Field testing was done on 17 September 2020 and as simulation predicted, the ADP rotor outperformed the STD rotor. Physical test output power was lower than expected simulation results. The expected power output from CFD was in the lower power range of the 400-watt rated generator used during field testing causing poor generator efficiency. Although we could not measure the absolute power accurately the relative power for the STD and ADP could still be compared. Further losses experienced during testing included mechanical, electrical, vibration and noise. These losses were the same for the STD and ADP rotor during field testing as the output power results for both rotors were similar and these losses were likely as a result

of the effect of the test rig on performance. The field test result revealed a shift of peak performance rotational speeds for both rotors compared to the simulation results with a maximum shift of 128.61 rpm for the ADP rotor.

Field test results indicated that the ADP rotor outperformed the STD rotor with 6.06 % at respective peak performance rotational speeds of 766.61 rpm for the STD and 920.94 rpm for the ADP rotor. Comparison of simulation and physical test performance curves showed that during simulation and physical results the ADP outperformed the STD at peak power rotational speeds.

This research focussed on comparative performance of two rotor designs and excluded any market related product comparison. Simulation results and physical test results provided evidence that the adapted BEMM approach for designing HAWT rotor blades for rotors with a 20% hub ratio increases the rotor power output at half the design wind speed. The simulation and field test results had acceptable outcome for this comparative study.

## **5.2 Recommendations**

### **5.2.1 Solid modelling and simulation**

It is recommended that a solid modelling software package be used for modelling of the rotors that has the capacity to export the final model into ANSYS as well as the capacity for the model to be used in manufacturing software.

Care must be taken during the modelling of the rotors to ensure there is adequate space between the rotor and rotating domain boundaries for full flow development during simulation.

Mesh independence is important for ensuring accurate and consistent simulation results. It is recommended that mesh independence residual values should take into consideration the accuracy of measurement during physical testing.

### **5.2.2 Vehicle-top test rig**

During physical testing, losses were evident. It is unlikely that mechanical losses on bearings could be significantly improved. Measured power output results were at the low range of the 400-watt rated generator used. This caused poor generator efficiency and it is recommended that generator sizing receives careful attention in future testing. Funding limitations and the availability of a correct sized generators meant that a properly matched generator was not available for this study and we had to make use of the available 400-watt rated generator which produced much lower power than what a properly matched smaller generator would have and this means that a properly matched generator should really be used for future work.

Recommendation for the test rig also include the possible improvement of vibration and shock loss absorption which is transferred from the wheels during testing and to reduce wind fluctuation for future testing.

### **5.2.3 Future rotor research**

Future research for small, large hub ratio HAWTs could include comparison of vehicle-top test rig results to wind tunnel test results – thereby confirming the feasibility of vehicle-top test rig testing.

We have found that the CFD projected peak performance rotational speed cannot be used as an indicator because the measured peak performance rotational speed differs by as much as 128.61 rpm and this should influence the research methodology going forward. It might be possible to develop empirical equations to adjust the peak power rotational speed from the CFD prediction to the actual speed for particular wind turbine designs (STD and ADP rotors).

The improved power output of the ADP rotor from this study should provide motivation for further improvement of the adapted BEMM used in the design of the ADP rotor.

## 6. References

- 2713-3466 R44, Betty's Bay, 7141 to 3099 R44, Betty's Bay, 7141 - Google Maps (no date). Available at: <https://www.google.com/maps/dir/-34.35736,18.9509342/-34.3577392,18.9696896/@-34.3581184,18.9525928,16z> (Accessed: 18 September 2020).
- ANSYS: Customer Training Manual (2010) 'Methodology Introduction to ANSYS FLUENT', pp. 1–17.
- Antonelli, M. *et al.* (2013) 'Subdivision surfaces integrated in a CAD system', *CAD Computer Aided Design*. Elsevier Ltd, 45(11), pp. 1294–1305. doi: 10.1016/j.cad.2013.06.007.
- Bouhelal, A. *et al.* (2018) 'Numerical investigation of turbulent flow around a recent horizontal axis wind Turbine using low and high Reynolds models', *Journal of Applied Fluid Mechanics*, 11(1), pp. 151–164. doi: 10.29252/jafm.11.01.28074.
- Chen, T. Y. and Liou, L. R. (2011) 'Blockage corrections in wind tunnel tests of small horizontal-axis wind turbines', *Experimental Thermal and Fluid Science*. Elsevier Inc., 35(3), pp. 565–569. doi: 10.1016/j.expthermflusci.2010.12.005.
- Cong, W. and Song, S. P. (2014) '3D modeling of wind turbine blade based on solidworks', in *Applied Mechanics and Materials*. Truns Tech Publications, pp. 123–127. doi: 10.4028/www.scientific.net/AMM.595.123.
- Council of Scientific and Industrial Research, *n.d.* <https://www.csir.co.za/> (no date). Available at: <https://www.nal.res.in/en/facilities/1-5m-low-speed-wind-tunnel> (Accessed: 30 April 2019).
- CSIR (2018) 'CSIR, 2018. Email correpondance'.
- Dawoud, B., Amer, E. and Gross, D. (2007) 'Performance analysis of CCHP and CHP systems operating following the thermal and electric load', *International journal of energy research*, 31(August 2007), pp. 135–147. doi: 10.1002/er.
- Det Norske Veritas, *n.d.* <http://www.dnvgl.com> [2019] (no date) *bladed*.
- Duffy, M. (2009) 'Small Wind Turbines Mounted to Existing Structures Aerospace Master ' s Thesis Proposal Michael Duffy', pp. 1–23. Available at: [https://www.researchgate.net/figure/1-Images-of-two-micro-wind-turbine-sites-that-were-monitored-during-the-Warwick-Wind\\_fig1\\_237265433](https://www.researchgate.net/figure/1-Images-of-two-micro-wind-turbine-sites-that-were-monitored-during-the-Warwick-Wind_fig1_237265433) (Accessed: 6 May 2020).
- Electro Peak* (no date). Available at: <https://electropeak.com> (Accessed: 1 September 2020).
- Hansen, M. O. L. (2008) 'AERODYNAMICS OF WIND TURBINES Hearth Scan', *London Sterling*.
- International Energy Agency (2019) *Offshore Wind Outlook 2019 – Analysis - IEA*. Available at: <https://www.iea.org/reports/offshore-wind-outlook-2019> (Accessed: 6 May 2020).
- Jonkman, J. M. *et al.* (2015) *AeroDyn v15 User's Guide and Theory Manual, National Renewable Energy Laboratory 15013 Denver West Parkway Golden*.
- Kaya, M. N. *et al.* (2018) 'Aerodynamic performance of a horizontal axis wind turbine with forward and backward swept blades', *Journal of Wind Engineering and Industrial Aerodynamics*. Elsevier Ltd, 176(March), pp. 166–173. doi: 10.1016/j.jweia.2018.03.023.
- Khlaifat, N. *et al.* (2020) 'Optimization of a small wind turbine for a rural area: A case study of Deniliquin, New South Wales, Australia', *Energies*, 13(9). doi: 10.3390/en13092292.
- Mara, B. K. *et al.* (2014) 'Development and validation of a CFD model using ANSYS CFX for aerodynamics simulation of Magnus wind rotor blades', (November). doi:

10.1109/HNICEM.2014.7016231.

Marten, D. (2012) 'QBlade Guidelines', p. 37. doi: 10.13140/RG.2.1.3819.8882.

McGowan J, Rogers J, M. A. (2009) *Wind Energy Explained - Theory, design and application, 2nd edition*. John Wiley & Sons Ltd.,.

Moriarty, P. J. and Hansen, A. C. (2005) 'AeroDyn Theory Manual, NREL/TP-500-36881, Golden, Colorado: National Renewable Energy Laboratory', (December).

Namiranian, A. (2011) '3D Simulation of a 5MW Wind Turbine'.

*National Aeronautics and Space Administration.n.d., Open return wind tunnel.* <https://www.grc.nasa.gov/www/k-12/airplane/tunoret.html> (no date). Available at: <https://www.grc.nasa.gov/www/k-12/airplane/tunoret.html> (Accessed: 3 May 2019).

Oaks, W. and Paoletti, S. (2000) 'Polyhedral mesh generation', *Proceedings of the 9th International Meshing RoundTable*, (January 2000), pp. 57–66.

Refan, M. and Hangan, H. (2012) 'Aerodynamic performance of a small horizontal axis wind turbine', *Journal of Solar Energy Engineering, Transactions of the ASME*, 134(2), pp. 1–7. doi: 10.1115/1.4005751.

Sant, T. (2007) *Improving BEM-based Aerodynamic Models in Wind Turbine Design Codes1*.

SimScale (2020) *What are the Navier-Stokes Equations?*, *SimWiki*. Available at: <https://www.comsol.de/multiphysics/navier-stokes-equations> (Accessed: 11 May 2020).

*SMART BLADE - Blade Aerodynamics & Design* (no date). Available at: <https://www.smart-blade.com/blade-design-1> (Accessed: 3 May 2019).

Song, Q. (2012) *Design, fabrication, and testing of a new small wind turbine blade*. Unpublished Master Thesis, University of Guelph, Canada.

*South African Wind Energy Association.n.d.Stats and Facts.* <https://sawea.org.za> [2019] (no date). Available at: <https://sawea.org.za/stats-and-facts-sawea/> (Accessed: 16 August 2020).

Tande, J. J. (2011) *CFD Study of a 10 MW Offshore Horizontal Axis Wind Turbine Blade*.

Wei Xie Wei (2017) 'An Innovative Umbrella-Type Rotor of Horizontal Axis Wind Turbine to Regulate Power and Reduce Wind Thrust, Key Laboratory for Advanced Materials Processing Technology of MOE, Department of Mechanical Engineering, Tsinghua University, Beijing, China 8', 91, pp. 399–404.

Wheeler, K. R. and Southward, S. C. (2017) 'Efficient Operation of Diesel Generator Sets in Remote Environments', *Virginia Polytechnic Institute and State University*. Available at: <https://vtechworks.lib.vt.edu/handle/10919/78374>.

World Wind Energy Association (2019) *World Wind Energy Association*. Available at: <http://wwindea.org/blog/2018/02/12/2017-statistics/> (Accessed: 16 August 2020).

## 7. Appendices

### 7.1 Solid modelling procedure

This procedure for solid modelling of the wind turbine rotor is specific to this project but may be of assistance to future students who engage in similar research and could also be useful for future training.

The solid modelling followed the following steps:

1. Import of airfoil coordinates into Solid works as splines.
2. Creation of solid blade with imported splines.
3. Import of the hub frontal curve.
4. Creation of the solid hub.
5. Modelling of the complete rotor with three blades and hub; and
6. Creation of fluid and rotating domains for ANSYS simulation.

#### 7.1.1 Overview and starting point

The blade shape was created by connecting multiple airfoils (one for each element) with a smooth extrusion to make a solid body that followed the shape of the airfoils as closely as possible. Figure 57 illustrates the airfoils that define the blade shape.

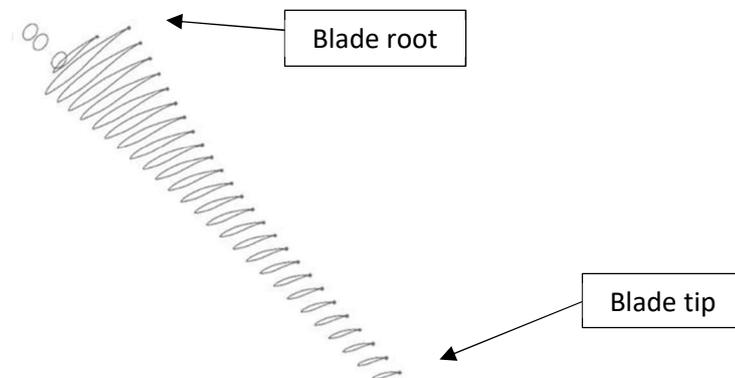


Figure 57. Blade airfoils (Kaya et al., 2018:167).

The airfoils were defined in three dimensions (x, y and z coordinates). It was important for the airfoil profiles or splines to be closed - meaning that the first set of coordinates had to be exactly the same value as the last set. Figure 58 is a sample of airfoil coordinates in excel. Note that the various spline profiles were numbered from 40.5 at tip of blade then 40, 39 and so on as the profiles move closer to the root of the blade. This was because the blade (in this study) was divided into 40 elements and the airfoil was designed at the centre of each element. This was why the outer edge of the tip element has been labelled 40.5.

Tip 40.5 $r_{tip} = 0.47000$			Element 40 $r_e = 0.46413$			39 $r_e = 0.45238$			38 $r_e = 0.44063$		
x	y	z	x	y	z	x	y	z	x	y	z
0.00225581	0.00012030	0.46999459	0.00507879	0.00033507	0.46409721	0.00903696	0.00093414	0.45228473	0.01181742	0.00147611	0.44046650
0.00225706	0.00013362	0.46999458	0.00508046	0.00035602	0.46409719	0.00903833	0.00096318	0.45228470	0.01181837	0.00151228	0.44046648
0.00225652	0.00014700	0.46999458	0.00507771	0.00037686	0.46409722	0.00903129	0.00099140	0.45228484	0.01180638	0.00154643	0.44046680
0.00225419	0.00016018	0.46999459	0.00507067	0.00039666	0.46409730	0.00901643	0.00101639	0.45228514	0.01178303	0.00157407	0.44046747
0.00225013	0.00017293	0.46999461	0.00505965	0.00041455	0.46409742	0.00899502	0.00103605	0.45228556	0.01175138	0.00159159	0.44046827
0.00224440	0.00018503	0.46999464	0.00504513	0.00042975	0.46409758	0.00896885	0.00104872	0.45228608	0.01170107	0.00160599	0.44046961
0.00223710	0.00019625	0.46999468	0.00502775	0.00044157	0.46409777	0.00883811	0.00108723	0.45228866	0.01130917	0.00172329	0.44047984
0.00222838	0.00020640	0.46999472	0.00500829	0.00044950	0.46409798	0.00848851	0.00118544	0.45229535	0.01085481	0.00184403	0.44049128
0.00221837	0.00021529	0.46999476	0.00489268	0.00048056	0.46409921	0.00809174	0.00128813	0.45230262	0.01033930	0.00196971	0.44050368
0.00220727	0.00022277	0.46999482	0.00463861	0.00054997	0.46410182	0.00765157	0.00139507	0.45231029	0.00976754	0.00210009	0.44051677
0.00219526	0.00022870	0.46999487	0.00436143	0.00062177	0.46410451	0.00717155	0.00150498	0.45231815	0.00914411	0.00223359	0.44053011
0.00218258	0.00023297	0.46999493	0.00406330	0.00069512	0.46410721	0.00665543	0.00161653	0.45232604	0.00847391	0.00236855	0.44054351
0.00206481	0.00026197	0.46999546	0.00374649	0.00076902	0.46410988	0.00610717	0.00172811	0.45233377	0.00776208	0.00250297	0.44055667
0.00190304	0.00030246	0.46999615	0.00341336	0.00084238	0.46411245	0.00553086	0.00183797	0.45234119	0.00701399	0.00263464	0.44056917
0.00173447	0.00034222	0.46999680	0.00306634	0.00091386	0.46411487	0.00493078	0.00194391	0.45234813	0.00623517	0.00276080	0.44058088
0.00156032	0.00038041	0.46999741	0.00270802	0.00098179	0.46411710	0.00431141	0.00204321	0.45235445	0.00543149	0.00287800	0.44059157
0.00138115	0.00041593	0.46999797	0.00233957	0.00104399	0.46411910	0.00367492	0.00213215	0.45236007	0.00460583	0.00298149	0.44060097
0.00119738	0.00044843	0.46999847	0.00196190	0.00109974	0.46412085	0.00302288	0.00220955	0.45236490	0.00376025	0.00306976	0.44060897
0.00101012	0.00047768	0.46999891	0.00157729	0.00114863	0.46412232	0.00235925	0.00227483	0.45236885	0.00289986	0.00314210	0.44061548
0.00082008	0.00050327	0.46999928	0.00118720	0.00118989	0.46412348	0.00168655	0.00232671	0.45237186	0.00202799	0.00319694	0.44062037
0.00062802	0.00052520	0.46999958	0.00079321	0.00122354	0.46412432	0.00100752	0.00236532	0.45237388	0.00114816	0.00323449	0.44062350
0.00043510	0.00054321	0.46999980	0.00039766	0.00124912	0.46412483	0.00032621	0.00238998	0.45237488	0.00026563	0.00325393	0.44062497
0.00024216	0.00055713	0.46999994	0.00000233	0.00126634	0.46412500	-0.00035433	0.00240027	0.45237486	-0.00061564	0.00325479	0.44062457
0.00005024	0.00056703	0.47000000	-0.00039069	0.00127542	0.46412484	-0.00103049	0.00239669	0.45237383	-0.00149099	0.00323775	0.44062248
-0.00013967	0.00057272	0.46999998	-0.00077937	0.00127598	0.46412435	-0.00169876	0.00237868	0.45237181	-0.00235585	0.00320219	0.44061870
-0.00032672	0.00057425	0.46999989	-0.00116192	0.00126820	0.46412355	-0.00235610	0.00234661	0.45236886	-0.00320630	0.00314862	0.44061337
-0.00050981	0.00057170	0.46999972	-0.00153617	0.00125232	0.46412246	-0.00299877	0.00230104	0.45236506	-0.00403750	0.00307785	0.44060650

Figure 58. Sample of airfoil coordinates in excel.

## 7.1.2 Importing airfoil coordinates into Solid Works as splines

In order to import the spline profiles created in excel into solid works a format change was necessary. Solid works only imports text files of 3D spline profiles. Each profile element for example 40.5 or 39 needed to have its own text file. The procedure to do this was as follows:

- Highlight the x, y and z coordinates in excel of the profile to be changed to text file.
- Copy the coordinates to a new note pad file. Only the coordinates without headings and with the x coordinate in the first column, y in second and z in third; and
- This needed to be done for all airfoil profiles individually.

Sample of the element airfoil profile text file is in Figure 59.

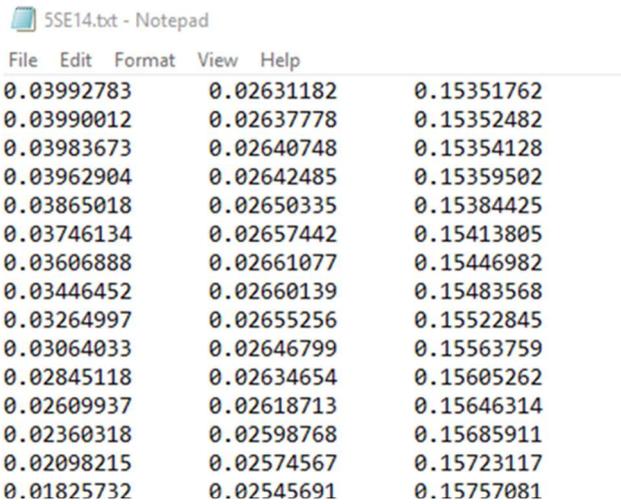


Figure 59. Sample of airfoil coordinates in note pad.

Once all the text files were created and ready to be imported into Solid works, the Solid works unit of measure must be changed to the same unit measure used in the airfoil coordinates. In other words, if the coordinates were in mm, solid works must be set to mm. Once Solid works is set to the correct measure unit select the **curves** button under features and scroll to **Curve through xyz points** and select as shown in Figure 60

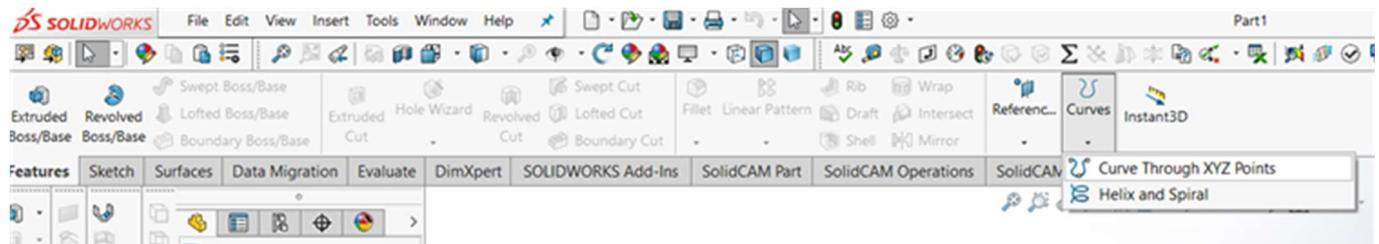


Figure 60. Curves though xyz points.

This will open the curve import window. **Browse** for the saved coordinate text file (note pad file) and select **ok** as shown in Figure 61. This must be done for each airfoil profile text file.

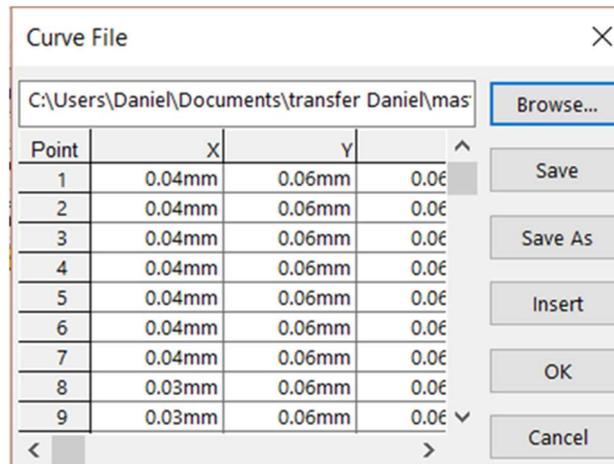


Figure 61. Curves import window.

Once this task is completed the imported splines will display in Solid works as Figure 62 illustrates. Note that in this design, concentrically curved airfoils were used. Straight airfoils can also be used (depending on design objectives).

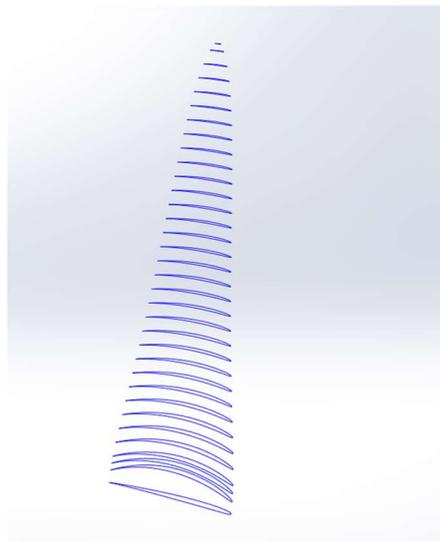


Figure 62. Imported splines.

### 7.1.3 Creating a solid blade with imported splines

Before creating the solid blade, it is important that the curves or splines be in consecutive order in the geometry tree of solid works. If not, the solid blade will be distorted. To create the solid, select all the curves in the tree and once highlighted, select **Boundary Boss**. While the Boundary Boss window is open ensure that all the control points on the splines are at the starting point of the splines. The control points act as a guideline in forming the solid. Figure 63 and Figure 64 shows these steps explained.

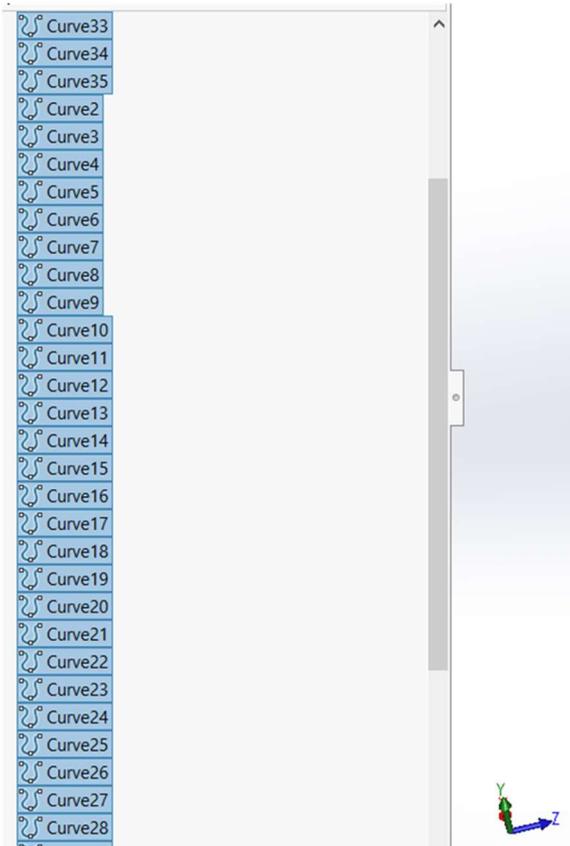


Figure 63. Consecutive splines selected.

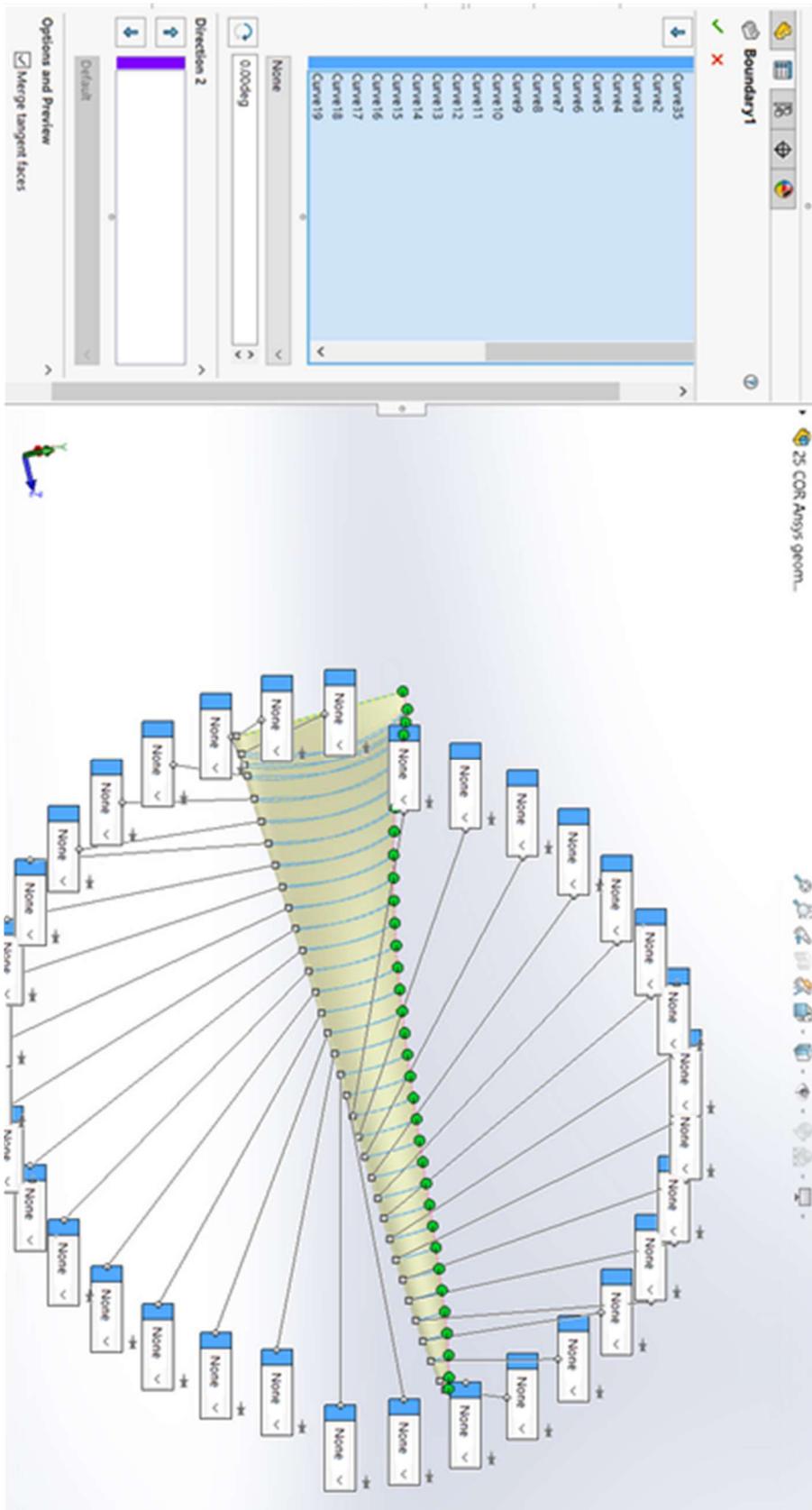


Figure 64. Boundary boss window with green control points aligned.

### 7.1.4 Importing the hub frontal curve

Importing the hub frontal curve follows the same procedure as to import the airfoil profiles. Figure 65 shows the frontal curve imported.

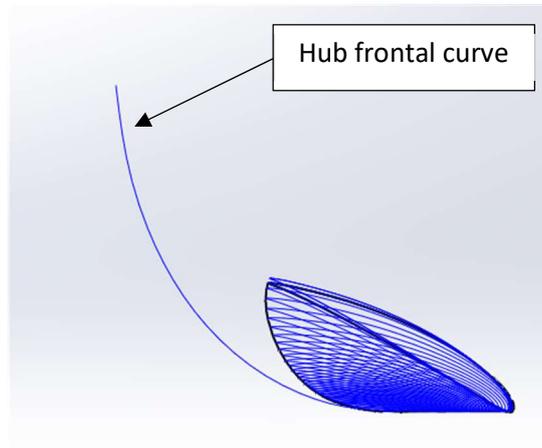


Figure 65. Hub frontal curve imported.

### 7.1.5 Creating the solid hub

Before creating the solid hub, additional hub geometry needs to be added to create the closed sketch which will be used to revolve to a solid as shown in Figure 66.

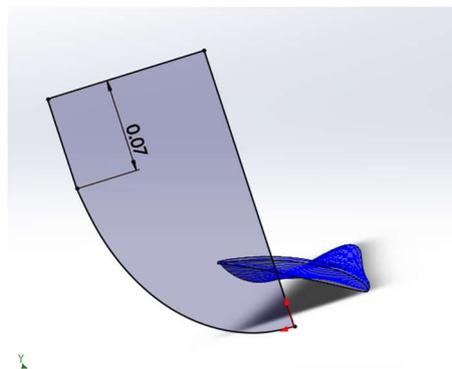


Figure 66. Hub profile.

Now that the hub profile / sketch is created select the hub profile sketch and select **Revolved Boss**.

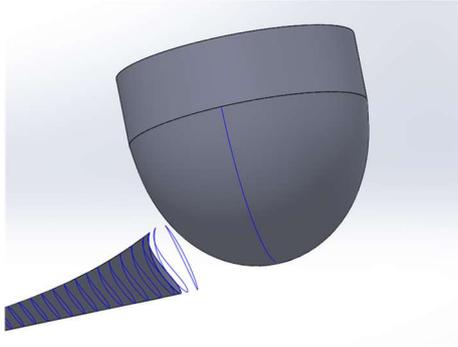


Figure 67. Solid hub.

It can be seen in Figure 67 that the solid hub is not in position and the hub needs to be moved into the correct position using the **Body-Move/Copy** function. The reference geometry is the leading edge of the blade which is the zero coordinate for the frontal plane. Once this is done the complete rotor can be modelled.

### 7.1.6 Modelling the complete rotor with three blades and hub

To model the complete three-bladed rotor, the blades must be **circular patterned** on the hub at 120° intervals. Before this can be done, one blade must be combined with the hub using the **Combine function** in Solid works. If it is not combined Solid works will not allow the blade to be circular patterned. Figure 68 to Figure 70 shows final steps to create final solid rotor model.

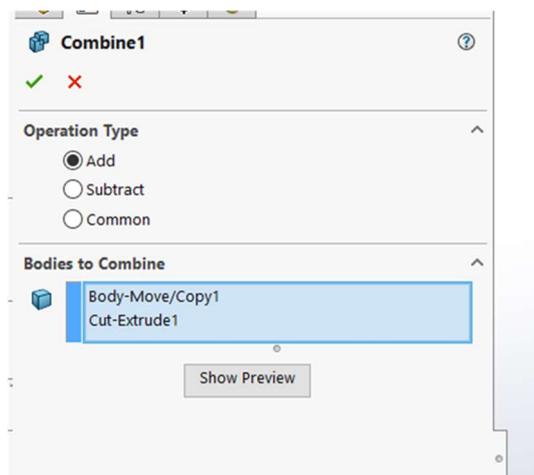


Figure 68. Combine function window.

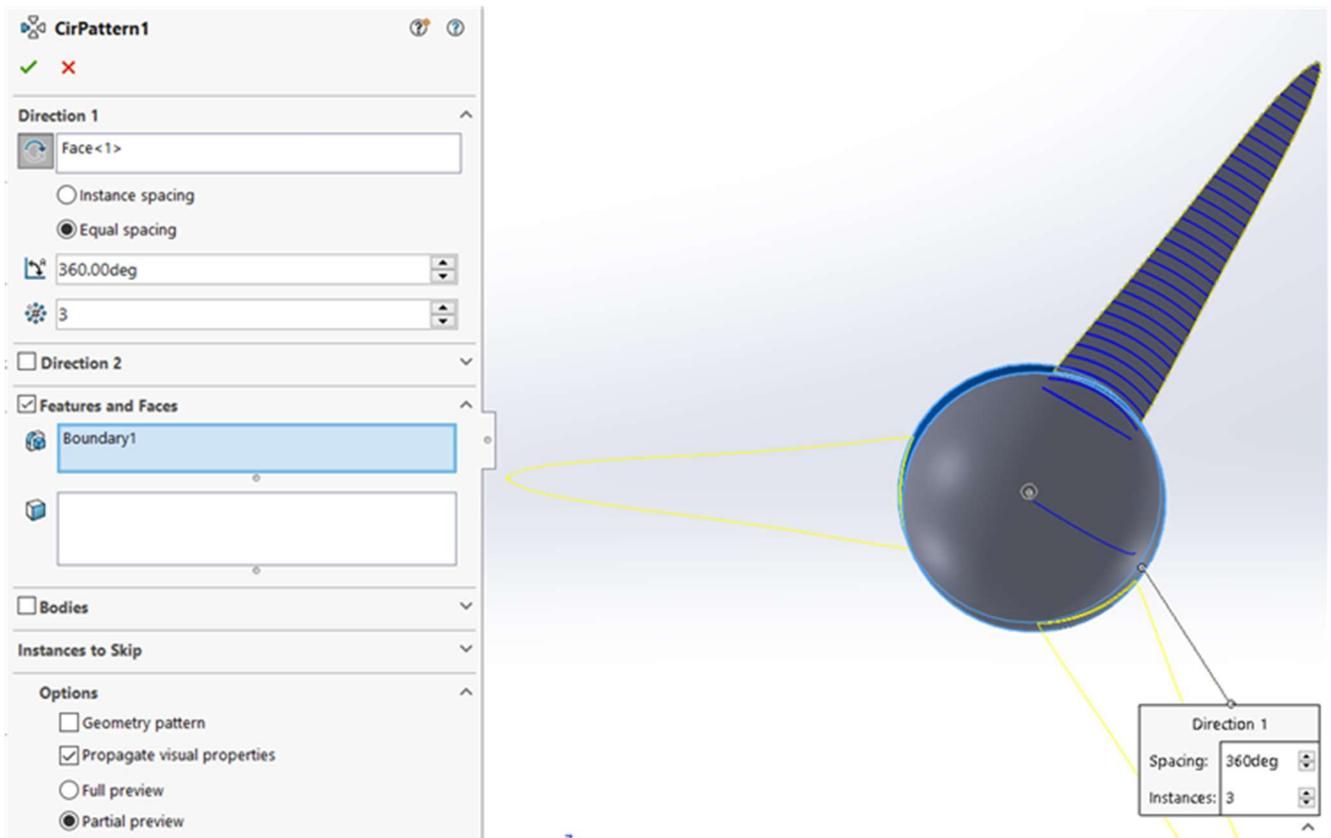


Figure 69. Circular pattern function window.

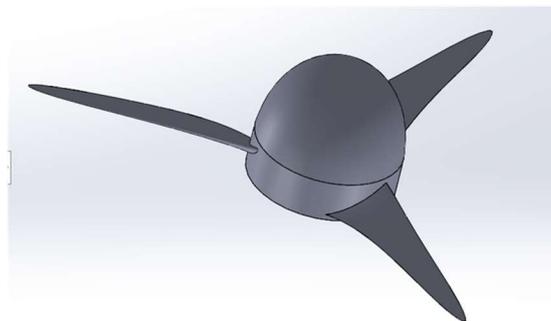


Figure 70. Complete rotor model.

### 7.1.7 Creating fluid and rotating domains for ANSYS simulation

The wind turbine rotor that will be simulated in ANSYS needs to be placed in a disc-shaped domain which will be rotating in the CFD simulation. The rotating domain containing the rotor must be placed inside the overall fluid domain. These domains are created by the **Extruded Boss** function in Solid works. When creating the two domains certain criteria must be followed. There must be adequate space between the rotor and rotating domain surfaces for ANSYS to successfully mesh the geometry in this space. The size and length of the overall fluid domain must also be considered to ensure correct simulation.

The first step in modelling the domains is to create sketches of the domain profiles. See Figure 71 for the sketch of the rotating domain. Then **Boss Extrude** the sketch to the necessary size shown in Figure 72. Note that the check box for merge result is unchecked.

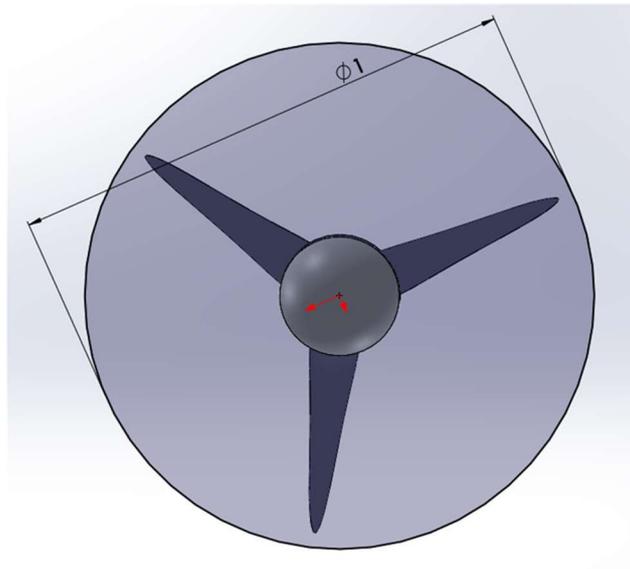


Figure 71. Sketch of rotating domain.

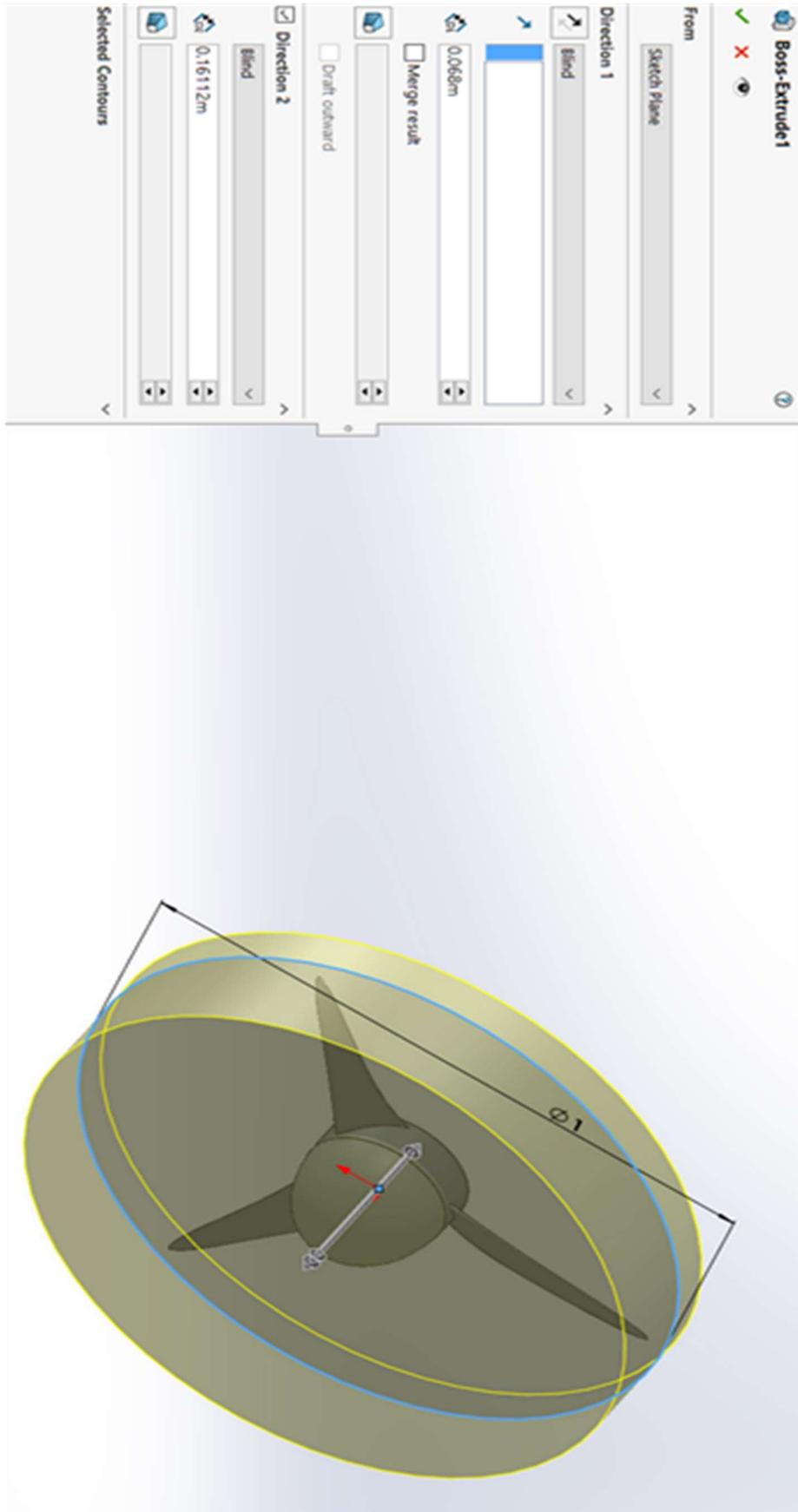


Figure 72. Boss extrudes of rotating domain.

The same must be done for the overall fluid domain. See the final result in Figure 73 and in Figure 74 zoomed in on the rotating disc and in Figure 75 are the final steps in the solid works steps tree.

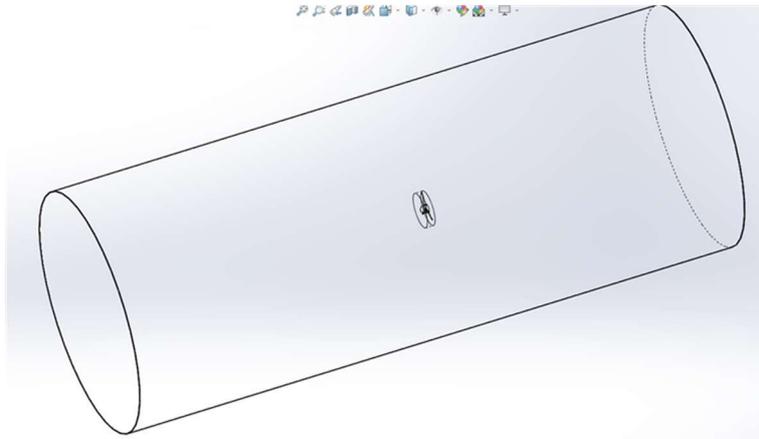


Figure 73. Full geometry for CFD simulation.

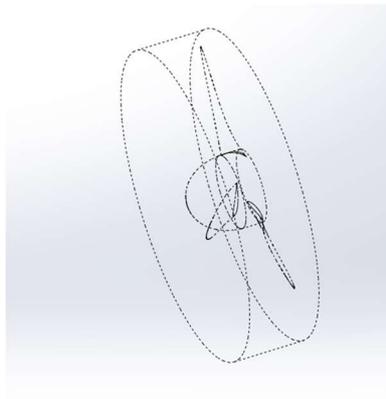


Figure 74. Rotating domain geometry (zoomed in).

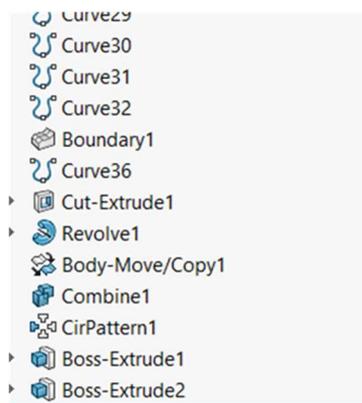


Figure 75. Final step in solid works tree for creating full geometry.

## 7.2 ANSYS Fluent simulation procedure

### 7.2.1 Importing and editing solid model

Open the work bench feature of ANSYS and drag and drop the **geometry** tab onto the project schematic. Right click on the **geometry** tab on the project schematic and select **import geometry** and browse for your Solid works model saved as an \*.IGS file. Figure 76 shows these steps explained.

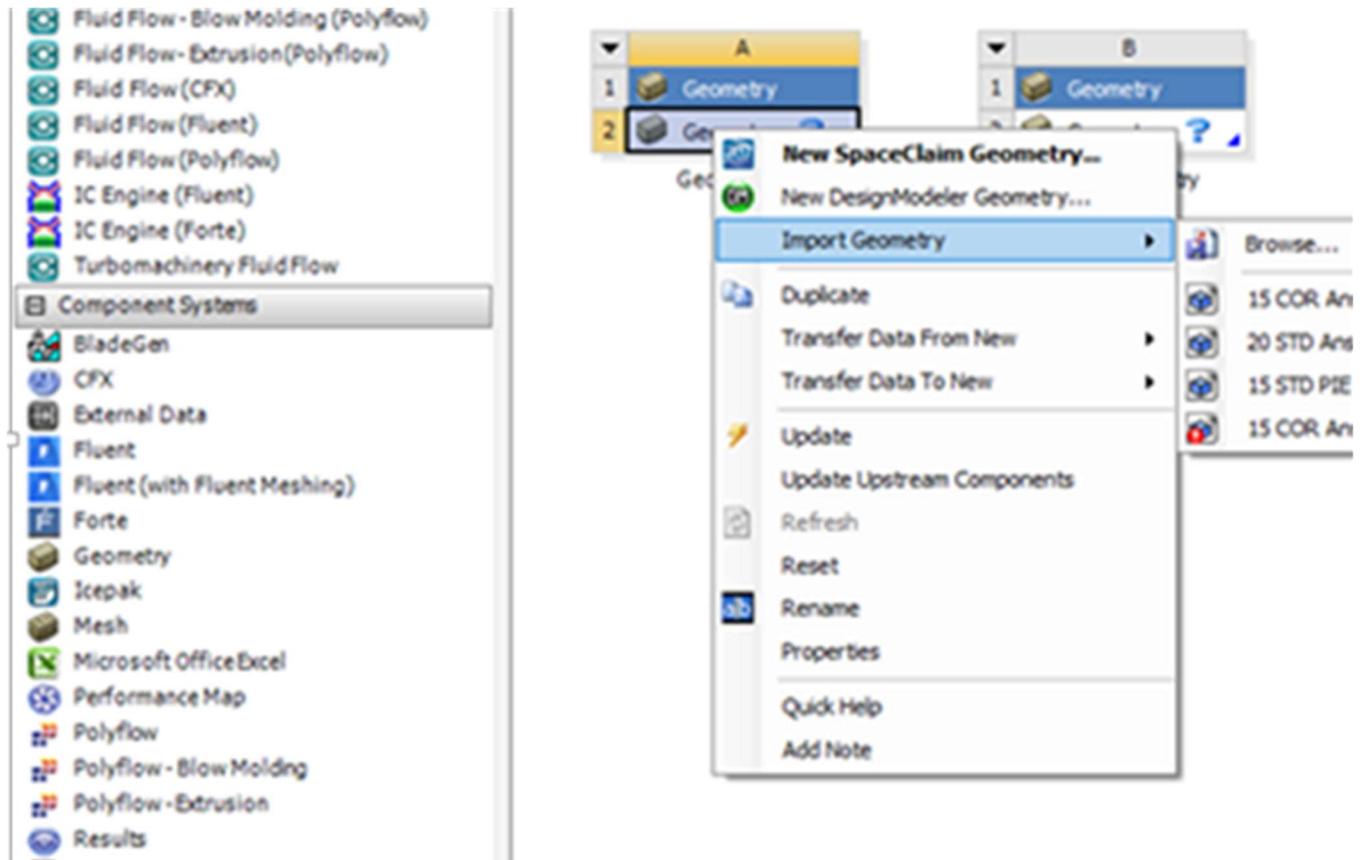


Figure 76. Geometry tab and import geometry steps.

Once imported right select **geometry** again and select **edit geometry** in **DesignModeler**.

This will open the **DesignModeler** as shown in Figure 77.

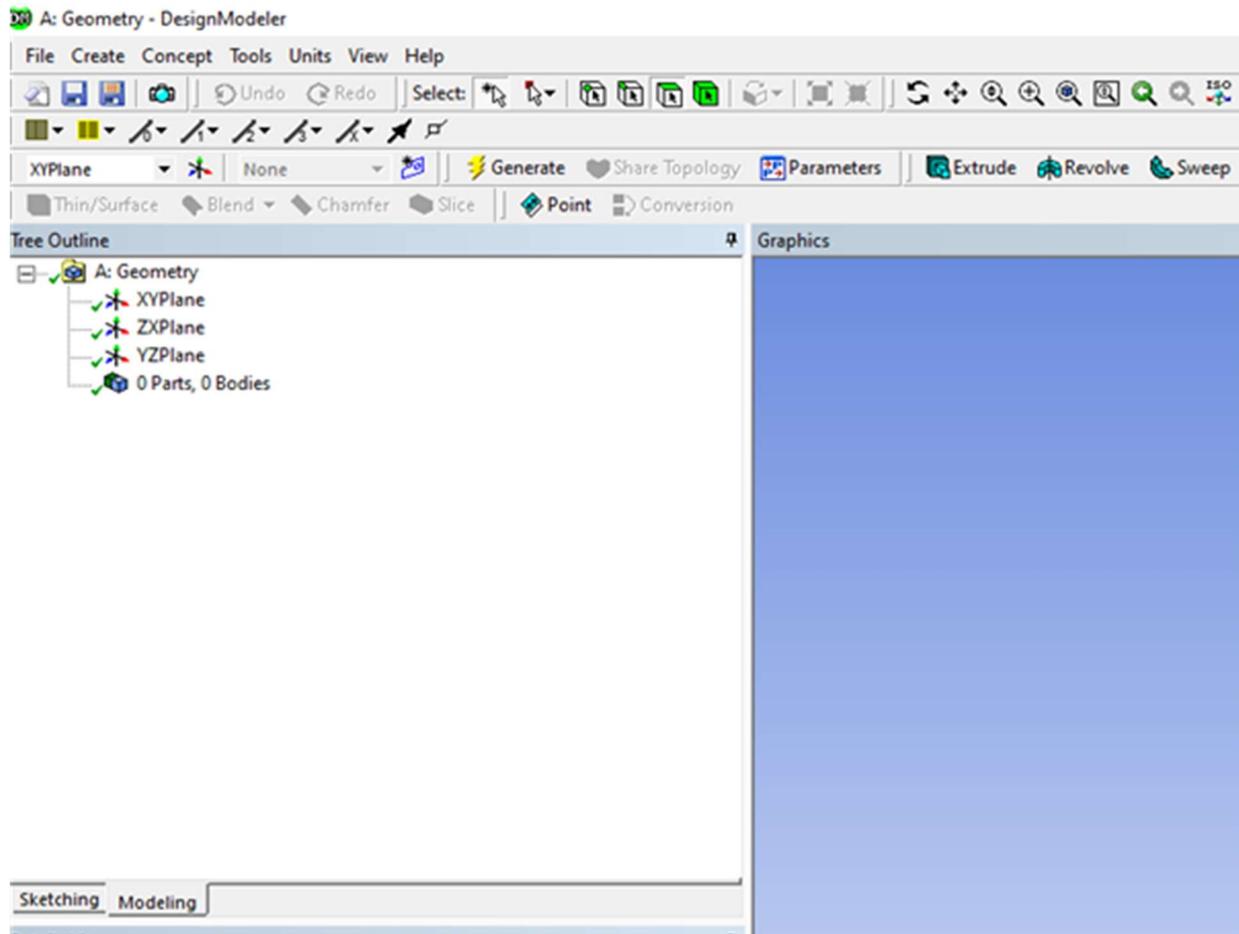


Figure 77. Screenshot of DesignModeler.

When DesignModeler is open select the **generate button**. This will generate the imported geometry. DesignModeler was used to create booleans for the rotor and the rotating domain of the solid model. This was done in order for Fluent to recognise the three entities (rotor, rotating and fluid domain) as separate geometry / entities within the solid model. Following were the methods to create the two booleans:

Boolean 1: Separating the fluid domain from the rotating domain Boolean setting are shown in Figure 78.

- Go to **create** and select **Boolean**;
- In **details view block** select **subtract**;
- Select the fluid domain as **target body**;
- Select rotating domain as **tool body**;
- Select yes for **tool preserver**; and
- Select **generate**

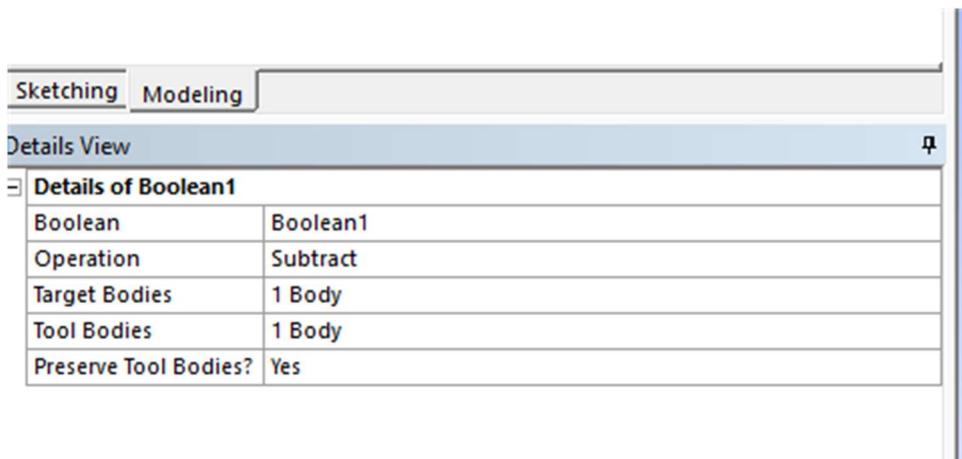


Figure 78. Boolean 1 settings.

Boolean 2: Separating the rotating domain and the rotor with boolean 2 settings in Figure 79.

- Go to **create** and **select Boolean**;
- In **details view block** select **subtract**;
- Select rotating domain as **target body**;
- Select complete rotor as **tool body**;
- Select yes for **tool preserver**; and
- Select **generate**.

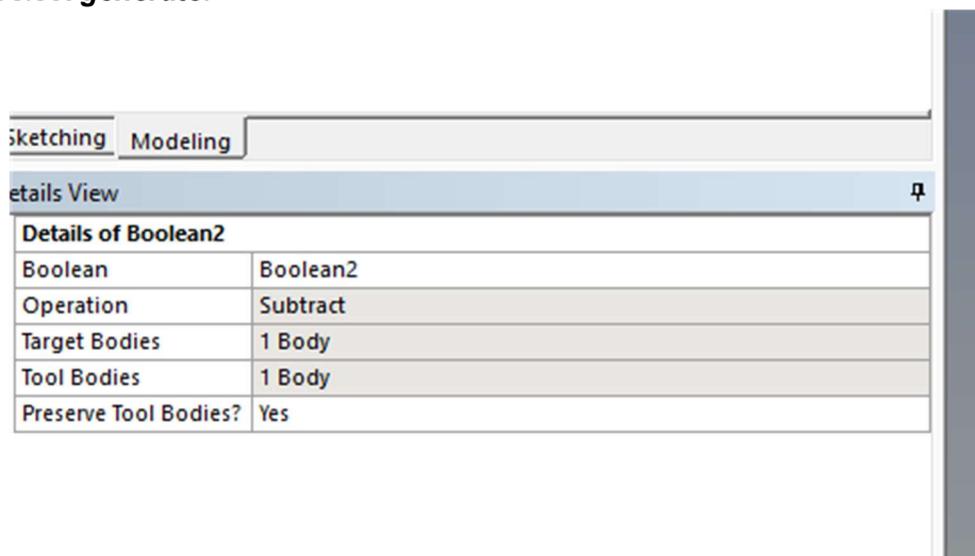


Figure 79. Boolean 2 settings.

After creating the booleans the solid part / bodies that were created had to be renamed as “Outerdomain” and “Innerdisc.” This is done by selecting the solid you want to rename with in the geometry tree, right click and choose **rename**. The result of this is shown Figure 80.

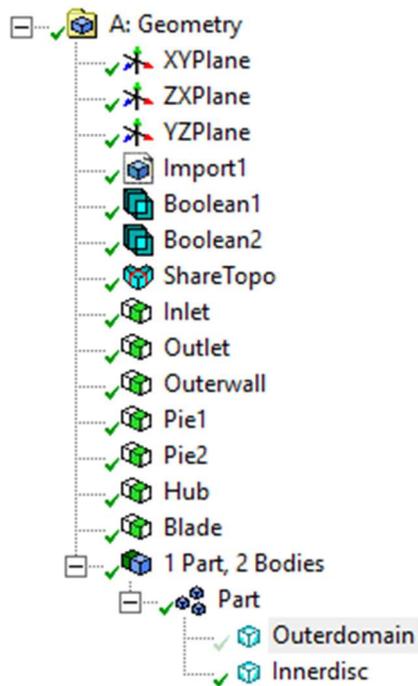


Figure 80. Renamed solid bodies.

## 7.2.2 Naming the rest of the geometry

### Inlet

- Select the inlet boundary with the **face selection tool**; 
- Right click and choose **named selection**, then type “**inlet**”;
- Remember to select the **generate button** after naming each boundary;
- Select **generate**; and
- Shown in Figure 81.

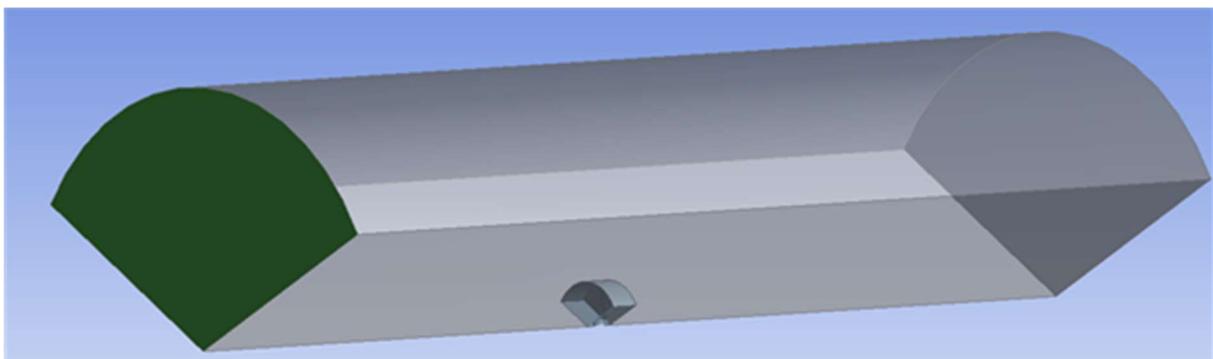


Figure 81. Inlet face.

### Outlet

- Select the outlet boundary with the **face selection tool**; 
- Right click and choose named selection, then type “**outlet**”;
- Select **generate**; and

- Shown in Figure 82.

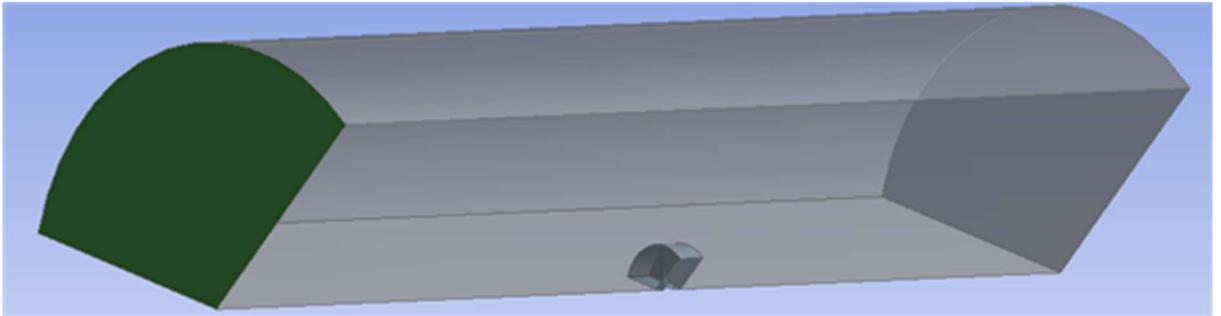


Figure 82. Outlet face.

### Outer wall

- Select the fluid domain outer boundary with the **face selection tool**  you must hold done **ctrl button** to select both surfaces on the outer boundary of the fluid domain;
- Right click and choose **named selection**, then type “**outerwall**”;
- Select **generate**; and
- Shown in Figure 83.

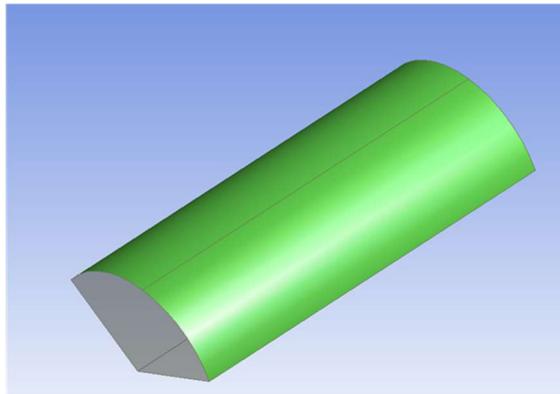


Figure 83. Outer wall face.

### Hub

- Select the all the faces of the hub geometry with the **face selection tool**  you must hold done **ctrl button** to select all surfaces on the hub;
- Right click and choose **named selection**, then type “**Hub**”;
- Select **generate**; and
- Shown in Figure 84.

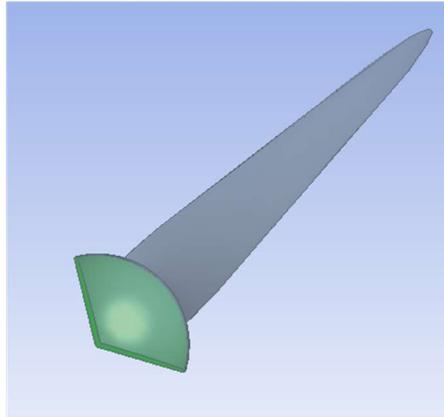


Figure 84. Hub faces selected.

### Blade

- Select the all the faces of the blade geometry with the **face selection tool**  you must hold done **ctrl button** to select all surfaces on the blade;
- Right click and choose **named selection**, then type "**Blade**";
- Select **generate**; and
- Shown in Figure 85.

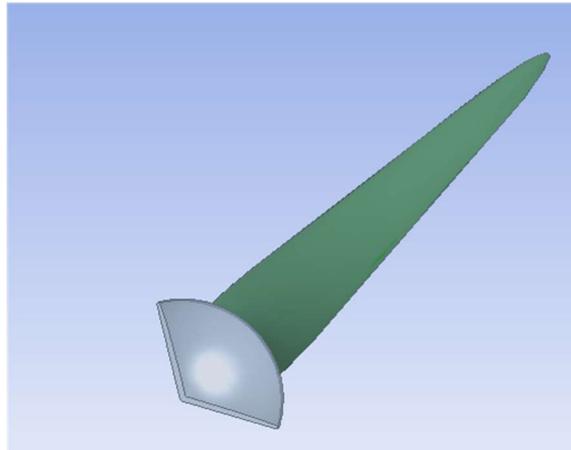


Figure 85. Blade faces selected.

### Periodic segments

- Select the cut away faces on one side of the fluid domain and "innerdisc" with the **face selection tool**  you must hold done ctrl button to select all three surfaces;
- Right click and choose named selection, then type "**pie 1**";
- Select **generate**.
- Shown in Figure 86; and
- Zoomed in section showing "innerdisc" face selection include in Figure 87.

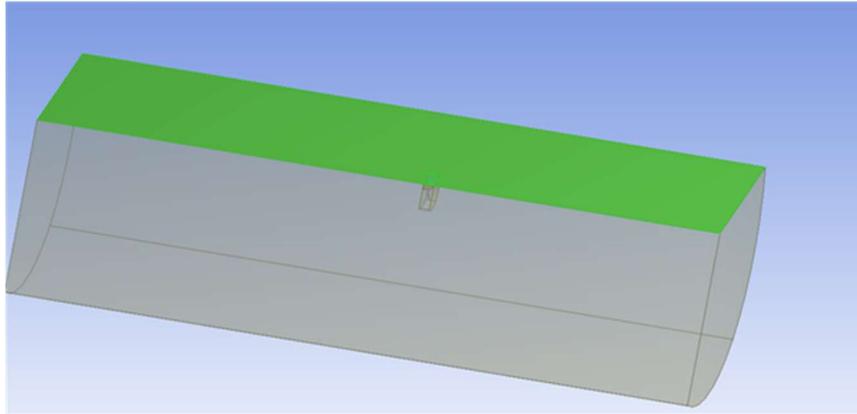


Figure 86. Pie 1 faces selected.

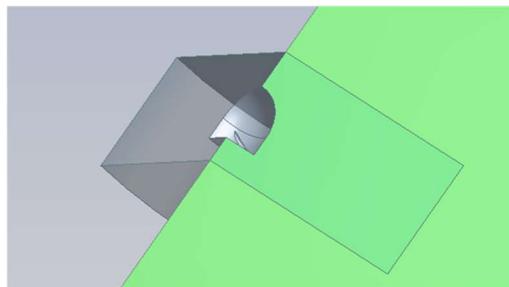


Figure 87. Zoomed in section showing "innerdisc" face included in "Pie 1" selection.

The same must be done for the other cut away plane and name it "**Pie 2**". The geometry tree outline after naming all the geometry should look like Figure 88.

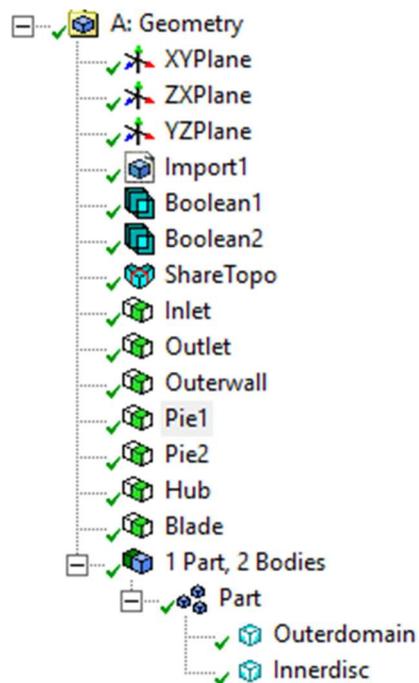
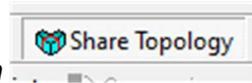


Figure 88. Geometry tree outline after naming all sections.

### 7.2.3 Creating shared topology

Highlight the two solids part under **part/ bodies** you renamed earlier by holding in **ctrl** and selecting them. Once highlighted right click and select **form new part** (make sure the **shared topology method** in the detail view block is set to **automatic**.)



Also select the **share topology button** on the menu and select **generate**. After the topology was shared the geometry tree should look like in Figure 88. Lastly the file had to be saved by going to **file** drop down menu and then **export**. Export your geometry file as **\*.agbd**. This file will be used to import the geometry into fluent.

### 7.2.4 Meshing the solid model

Run Fluent and in the opening dialog box in Figure 89 select **3D, meshing mode** and **serial**. The rest of the options may be left unticked and press **ok**.

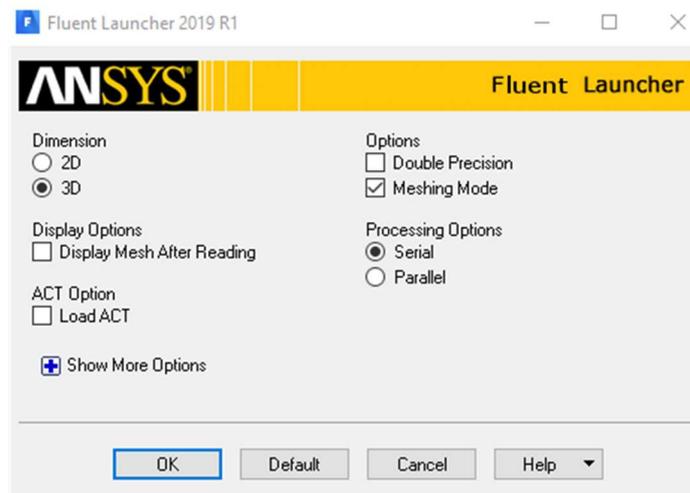


Figure 89. Fluent opening dialog.

In the **workflow tab** open the drop-down menu and select **water tight geometry** shown in Figure 90.

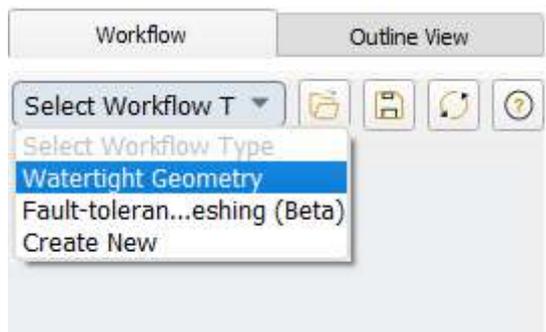


Figure 90. Workflow drop down menu.

When watertight geometry was selected the workflow tree will appear with import geometry on top. Select **import geometry** and import the geometry you created in DesignModeler with \*.agdb file extension as shown in Figure 91.

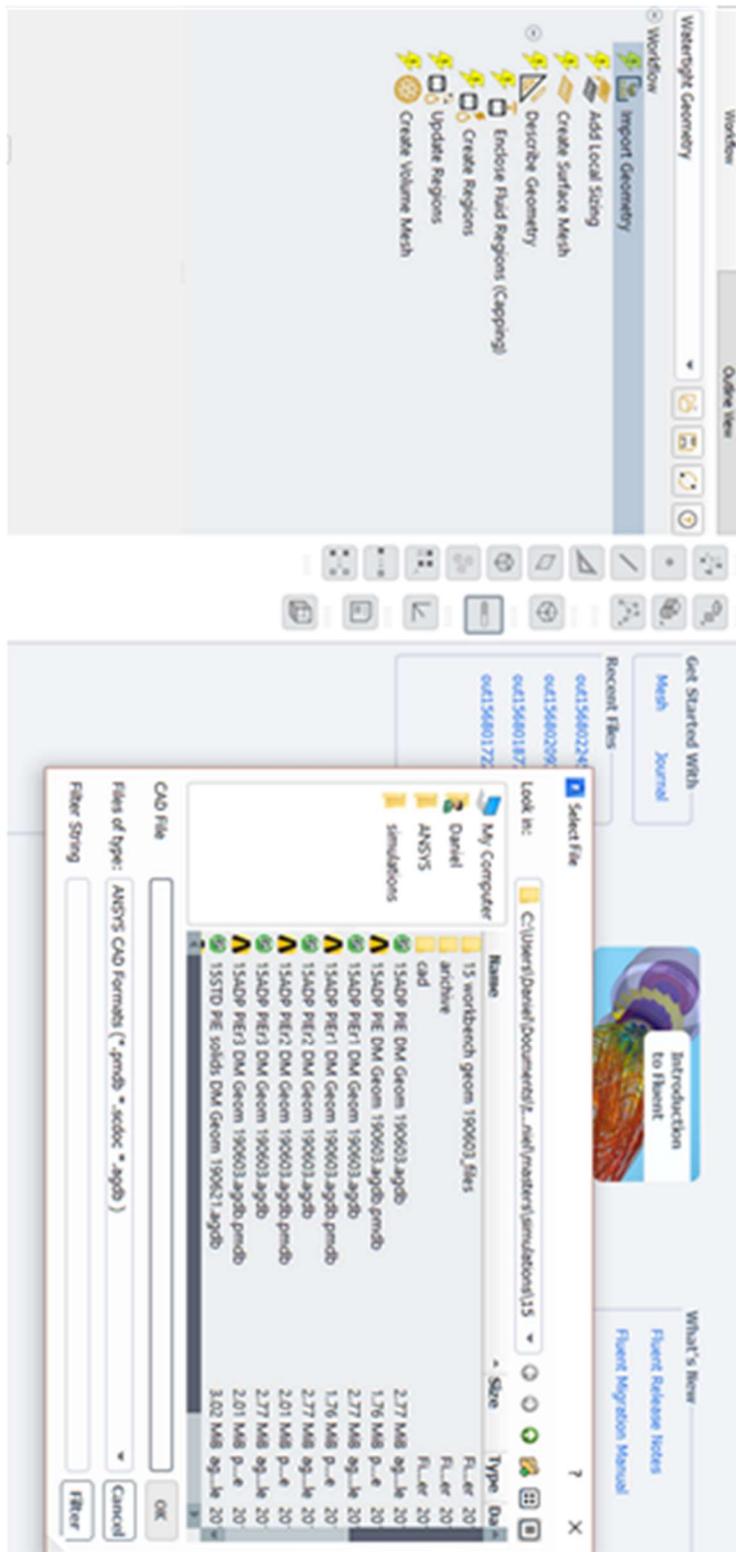


Figure 91. Import geometry step.

Next under **add local sizing** select **yes** for add local sizing and then select the geometry label for local sizing. Geometry labels “bladecellsize” and “hubcellsize” were selected with settings shown in Figure 92 and Figure 93.

Add Local Sizing	
Name	bladecellsize
Growth Rate	1.2
Size Control Type	Face Size
Target Mesh Size	0.42
Select By	label

Figure 92. “Bladecellsize” settings.

Add Local Sizing	
Name	hubcellsize
Growth Rate	1.2
Size Control Type	Face Size
Target Mesh Size	1.29
Select By	label

Figure 93. “Hubcellsize” settings.

Under **create surface mesh** the **min** and **max** size of mesh could be changed. Also, the **curvature normal angle, size functions, growth rate** and **cells per gap** can be set. In Figure 94 is the **create surface mesh** settings.

Create Surface Mesh	
Minimum Size	0.1
Maximum Size	425
Growth Rate	1.2
Size Functions	Curvature & Proximity
Curvature Normal Angle	10
Cells Per Gap	2
Scope Proximity To	edges

Figure 94. Create surface mesh settings.

Once the **surface mesh** generated. Right click on surface mesh and select insert **new task** and then **set up rotational periodic boundaries**. In the **set up rotational periodic boundaries** select method as **manual** and select “pie 2” geometry which you created in **DesignModeler** with settings shown in Figure 95.

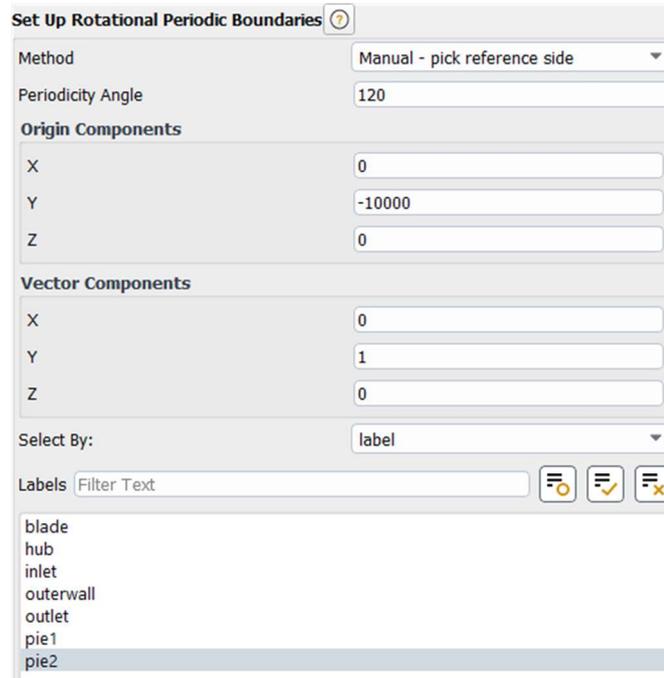


Figure 95. Rotational periodic boundaries settings.

Under **describe geometry** select settings as shown in Figure 96. Note that the **share topology** was not selected. The reason is that the topology share was already selected within **DesignModeler** earlier and does not need to be selected again.

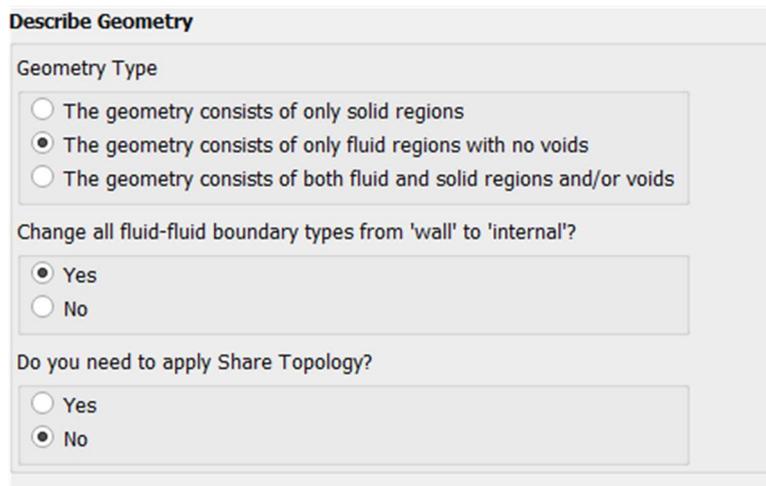


Figure 96. Describe geometry settings.

Under **update boundaries** make “inlet” as **velocity inlet** and “outlet” as **pressure outlet**. Leave “pie 1” and “pie 2” as is and make sure that all geometry which should be solids are selected as wall for boundary type as shown in Figure 97.

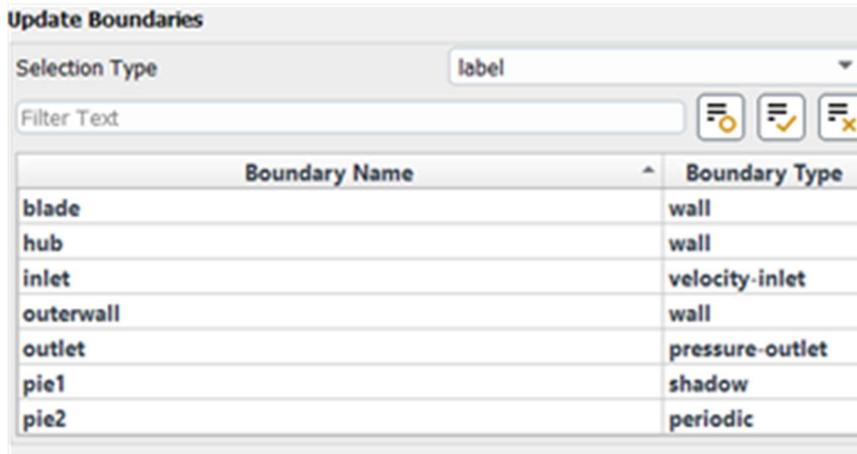


Figure 97. Update boundaries settings.

In Figure 98 the **update regions** setting are shown with both “innerdisc” and “outerdomain” selected as fluid region types.

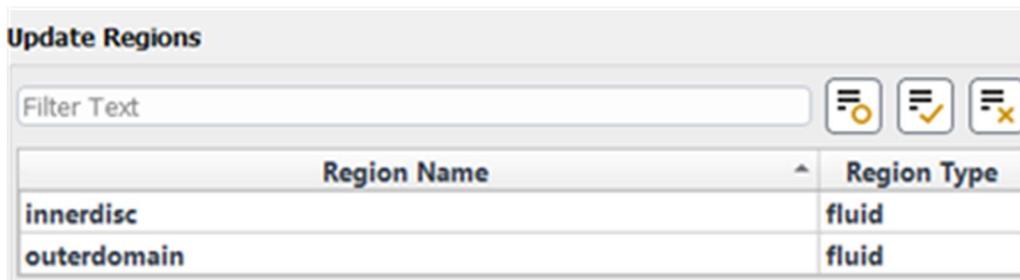


Figure 98. Update regions settings.

Settings for the **create volume mesh** was select as Figure 99 below for this simulation. Settings may however be chosen to suite any simulation demands.

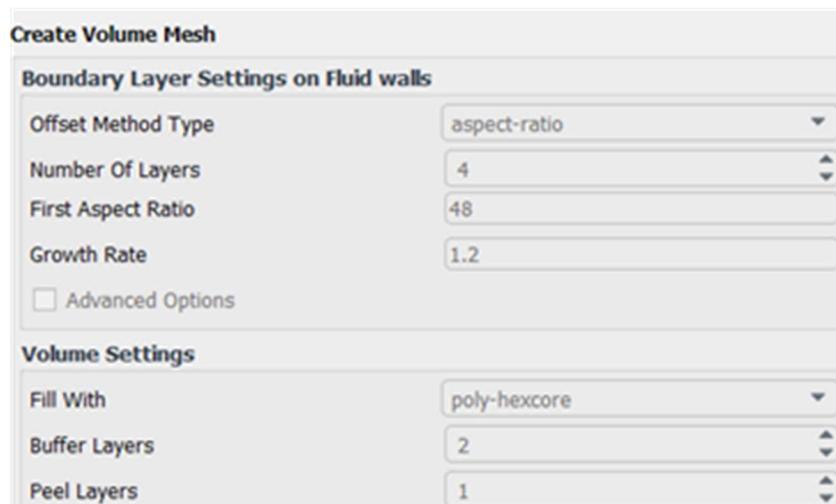


Figure 99. Control volume mesh settings.

After the volume mesh generated the volume mesh can be improved. In order to do this right click on **create volume mesh** and under **insert new task** select **improve volume**

**mesh**. In the **improve volume mesh** enter the **cell quality limit** your model must adhere to. In this procedure the cell quality was entered as 0.19 shown in Figure 100

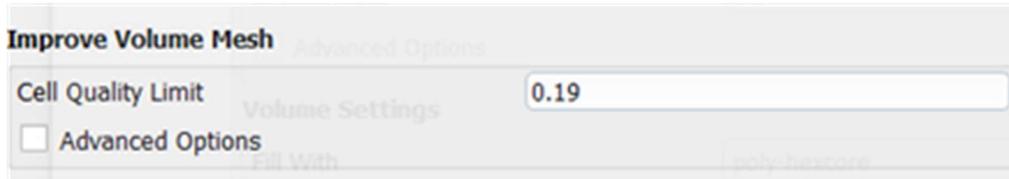


Figure 100. Improve volume mesh settings.

Once the **improve volume mesh** has been created select **save** button to save your mesh settings as a \*.wft file format or under **file** drop down menu select **write**, choose mesh and select to write a mesh file \*.msh file format. Click **switch to solution** to enter the Fluent solver setup.

## 7.2.5 Setup of Fluent solver

Within Fluent the setup for the solution was done in the outline view tree with subheading **setup**, **solution**, **results** and **parameters & customization**. A screen shot of the tree is shown in Figure 101. Once a setting is selected in the tree a new task page will open where settings and input must be added or adjusted.

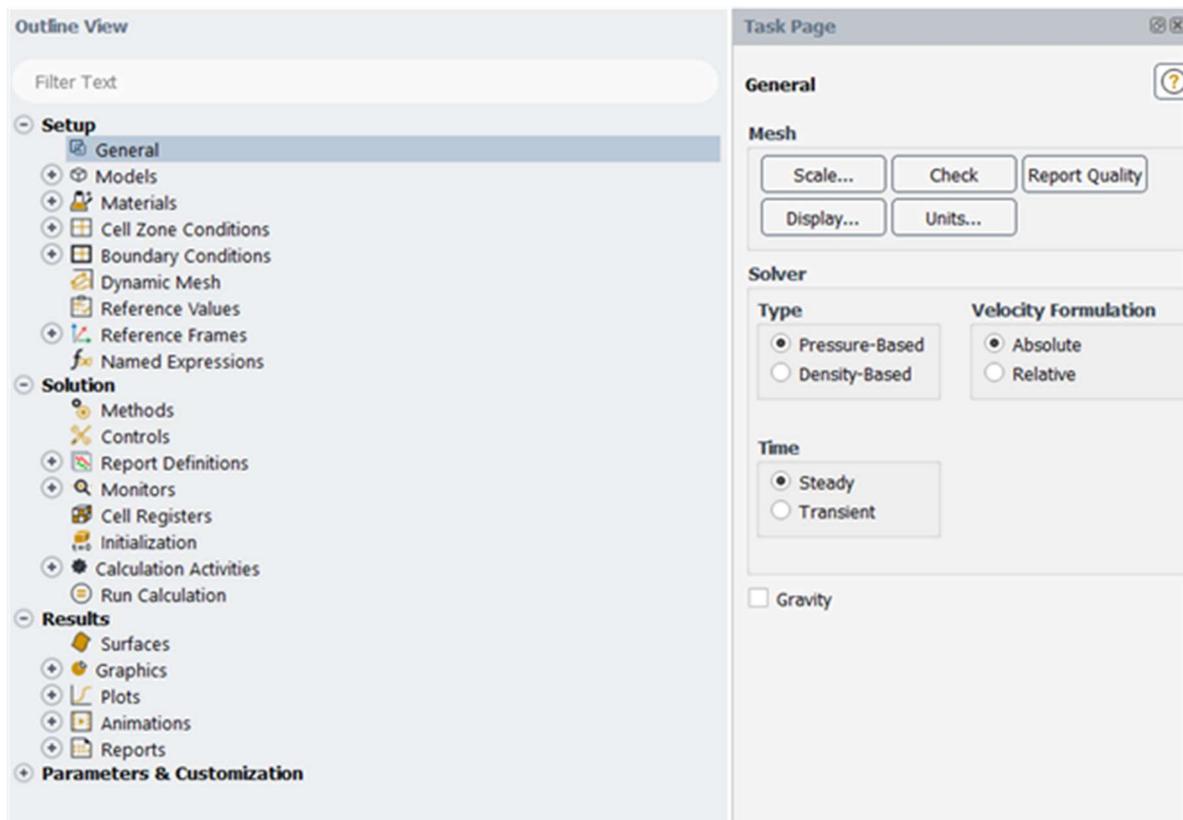


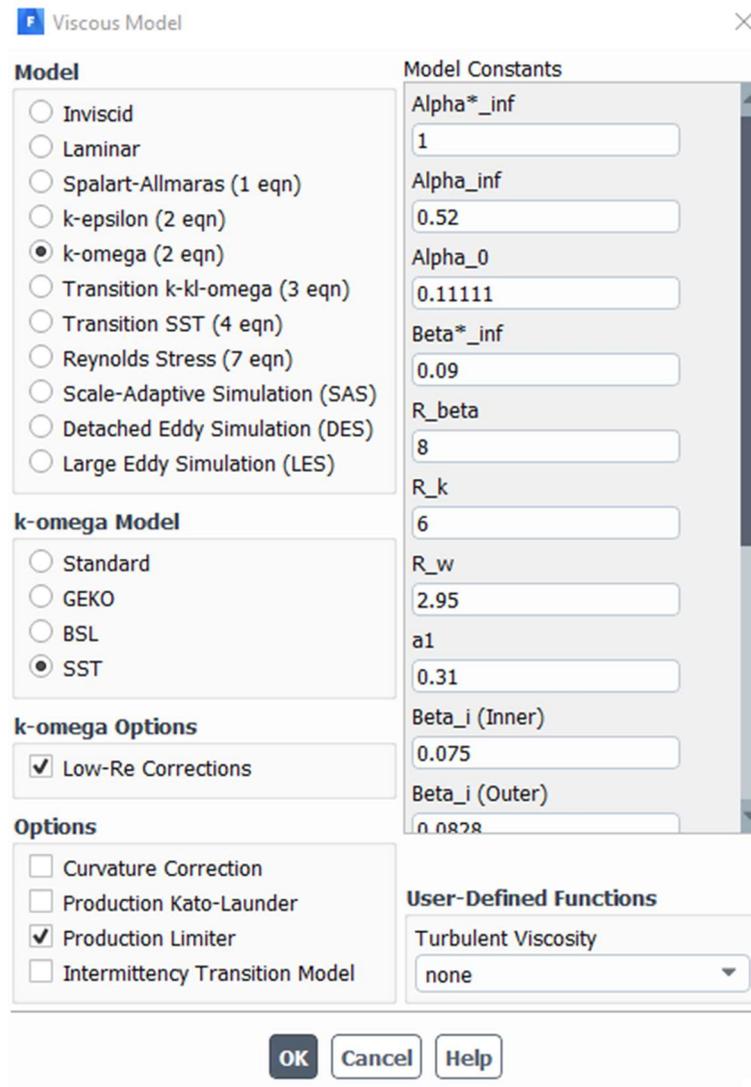
Figure 101. Tree outline with task page view.

## General

Select **pressure-based**, **absolute** and **steady** in the task page as shown in Figure 101.

## Models

Expand the **models** heading and double click on **viscous**. This opens the viscous model window as shown in Figure 102. Settings shown in the window are the viscous model settings used for this simulation. Once all settings are entered select **ok**. Make sure that any other model within the **models** heading is switched to off shown in Figure 103.



The image shows a software dialog box titled "Viscous Model". It is divided into several sections:

- Model:** A list of radio buttons for selecting a model. "k-omega (2 eqn)" is selected.
- k-omega Model:** A list of radio buttons for selecting a sub-model. "SST" is selected.
- k-omega Options:** A checkbox for "Low-Re Corrections" which is checked.
- Options:** A list of checkboxes: "Curvature Correction", "Production Kato-Launder", "Production Limiter" (checked), and "Intermittency Transition Model".
- Model Constants:** A list of input fields with numerical values: Alpha\*\_inf (1), Alpha\_inf (0.52), Alpha\_0 (0.11111), Beta\*\_inf (0.09), R\_beta (8), R\_k (6), R\_w (2.95), a1 (0.31), Beta\_i (Inner) (0.075), and Beta\_i (Outer) (0.0828).
- User-Defined Functions:** A dropdown menu for "Turbulent Viscosity" set to "none".

At the bottom of the dialog are three buttons: "OK", "Cancel", and "Help".

Figure 102. Viscous model window with settings.

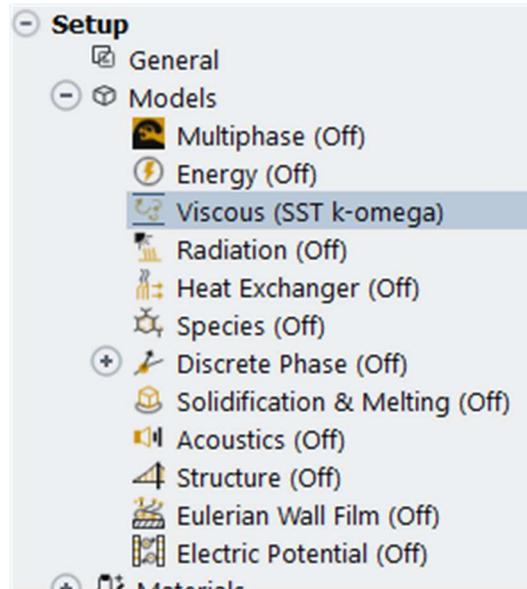


Figure 103. Models heading expanded.

## Materials

Expand **materials** heading and double click on **air** under **fluid**. In the air window enter the density and viscosity for the air (working fluid) being used for simulation. Figure 104 shows the air window with settings selected. No solid setting was required as we did not use it during this simulation.

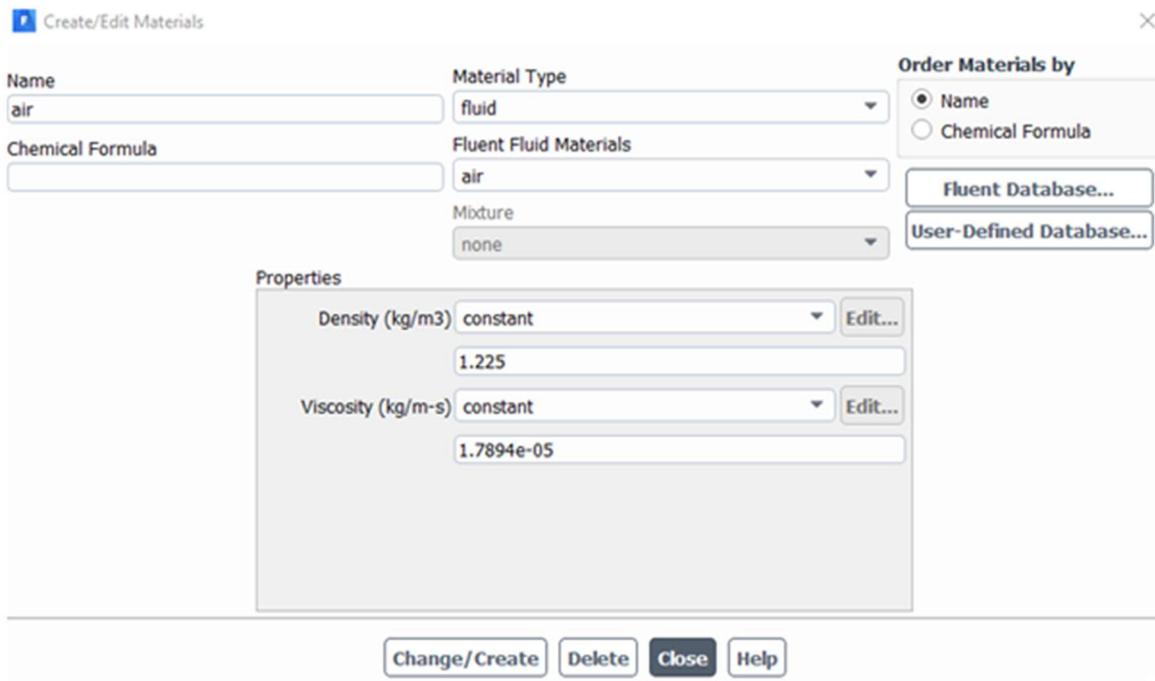


Figure 104. Air window with settings.

## Cell zone conditions

Expand **cell zone conditions** heading and double click on **innerdisc**. The “innerdisc” is the rotating part in the simulation. Once selected the “innerdisc” window opens. Figure 105 show the settings required for the “innerdisc”.

Fluid

Zone Name  
innerdisc

Material Name air Edit...

Frame Motion  3D Fan Zone  Source Terms  
 Mesh Motion  Laminar Zone  Fixed Values  
 Porous Zone

Reference Frame Mesh Motion Porous Zone 3D Fan Zone Embedded LES Reaction Source Terms Fixed Values Multiphase

Relative Specification UDF  
Relative To Cell Zone absolute Zone Motion Function none

Rotation-Axis Origin  
X (m) 0  
Y (m) 0  
Z (m) 0

Rotation-Axis Direction  
X 0  
Y 1  
Z 0

Rotational Velocity  
Speed (rpm) -1104.91  
Copy To Mesh Motion

Translational Velocity  
X (m/s) 0  
Y (m/s) 0  
Z (m/s) 0

OK Cancel Help

Figure 105. “Innerdisc” window with settings.

Similar to the “innerdisc” double click on **outerdomain** to open the settings window and select setting as in Figure 106.

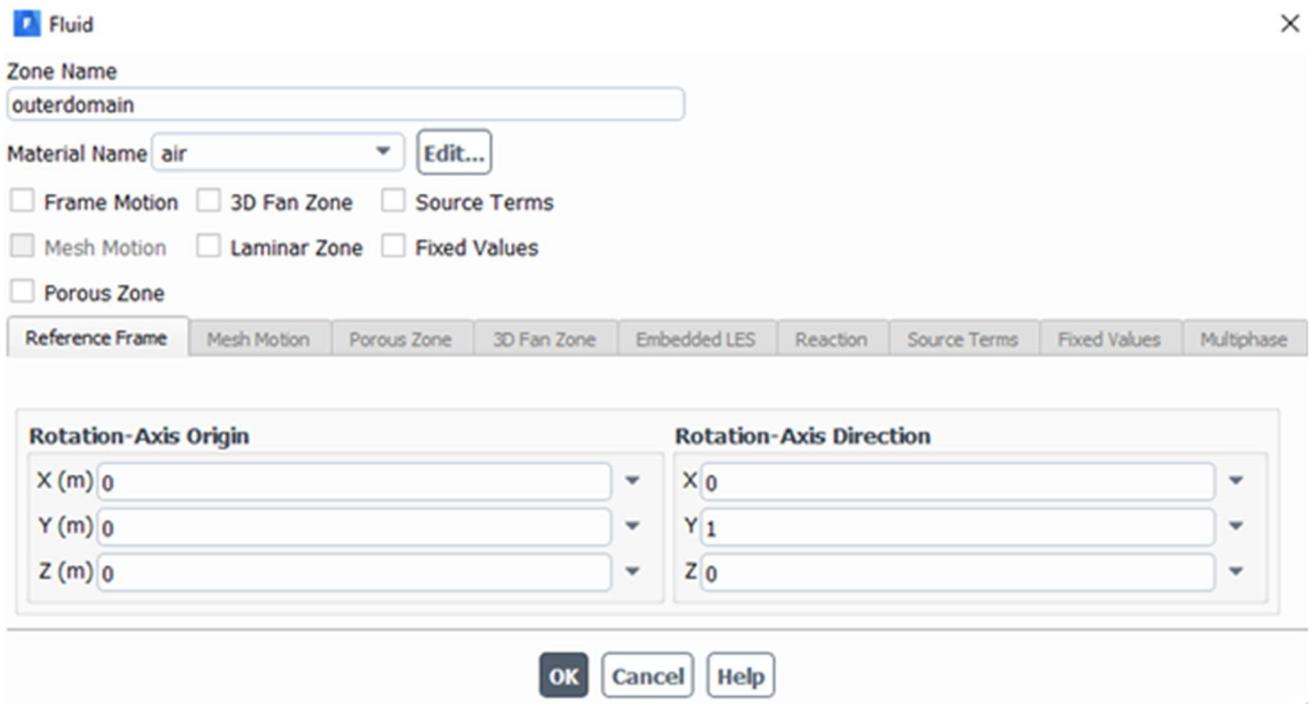


Figure 106. “Outerdomain” window with settings.

## Boundary conditions

After expanding the boundary conditions heading double click on blade. Select setting as shown in the blade window in Figure 107.

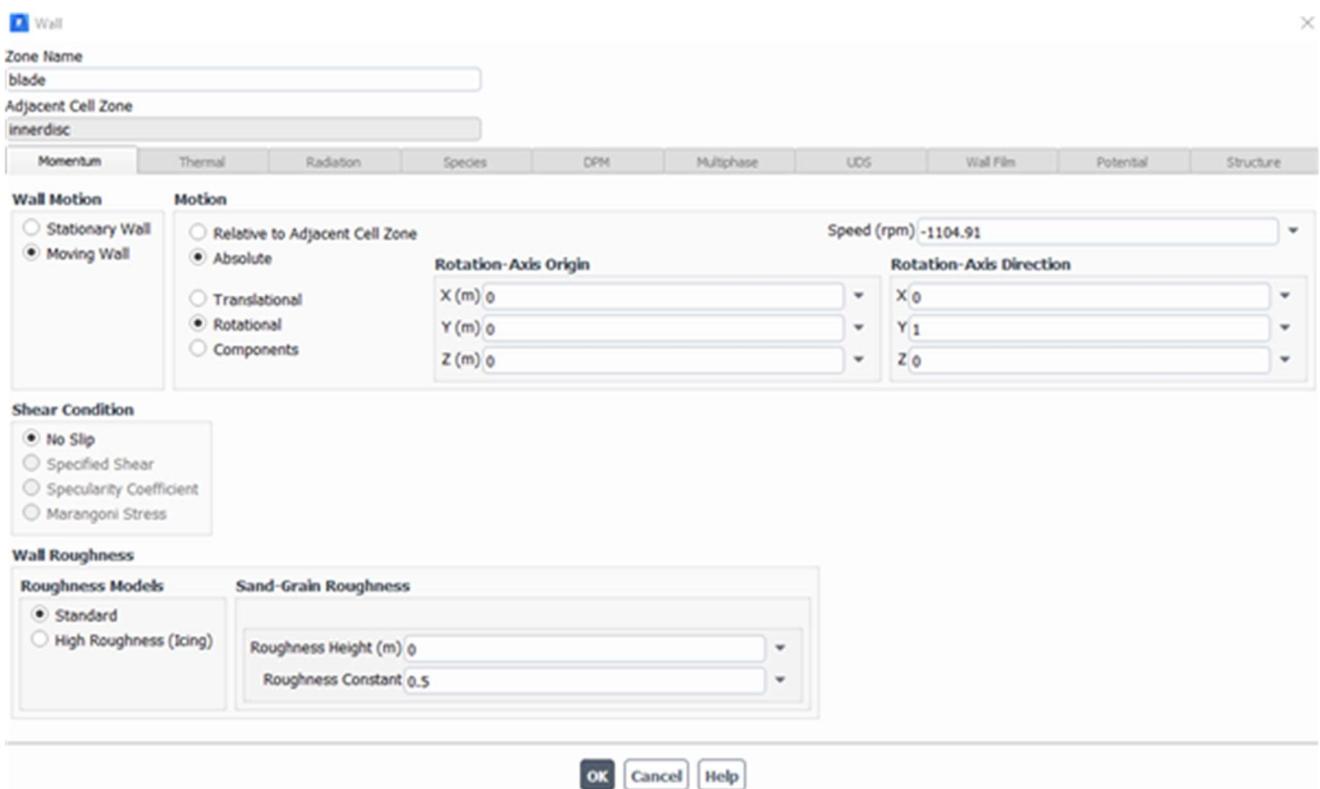


Figure 107. “Blade” window with settings.

Similarly, the settings for the rest of the boundary conditions must be selected as:

- Shown in Figure 108 for the “hub”;
- Shown in Figure 109 for the “inlet”;
- Shown in Figure 110 for the “innerdisc-outerdomain”;
- Shown in Figure 111 for the “interior-innerdisc”;
- Shown in Figure 112 for the “interior-outerdomain”;
- Shown in Figure 113 for the “outerwall”;
- Shown in Figure 114 for the “outlet”;
- Shown in Figure 115 for the “pie 2”;
- Shown in Figure 116 for the “pie 1”.

The screenshot shows the 'Wall' settings window for a boundary condition named 'hub'. The adjacent cell zone is 'innerdisc'. The 'Wall Motion' section is set to 'Moving Wall' with 'Rotational' motion selected. The speed is -1104.91 rpm. The rotation axis origin is at (0, 0, 0) and the direction is (0, 1, 0). The 'Shear Condition' is set to 'No Slip'. The 'Wall Roughness' section is set to 'Standard' with a roughness height of 0 and a roughness constant of 0.5.

Model	Value
Zone Name	hub
Adjacent Cell Zone	innerdisc
Momentum	Active
Thermal	Inactive
Radiation	Inactive
Species	Inactive
DPM	Inactive
Multiphase	Inactive
UDS	Inactive
Wall Film	Inactive
Potential	Inactive
Structure	Inactive
Wall Motion	Moving Wall
Motion	Absolute
Speed (rpm)	-1104.91
Rotation-Axis Origin X (m)	0
Rotation-Axis Origin Y (m)	0
Rotation-Axis Origin Z (m)	0
Rotation-Axis Direction X	0
Rotation-Axis Direction Y	1
Rotation-Axis Direction Z	0
Shear Condition	No Slip
Wall Roughness Model	Standard
Roughness Height (m)	0
Roughness Constant	0.5

Figure 108. “Hub” window with settings.

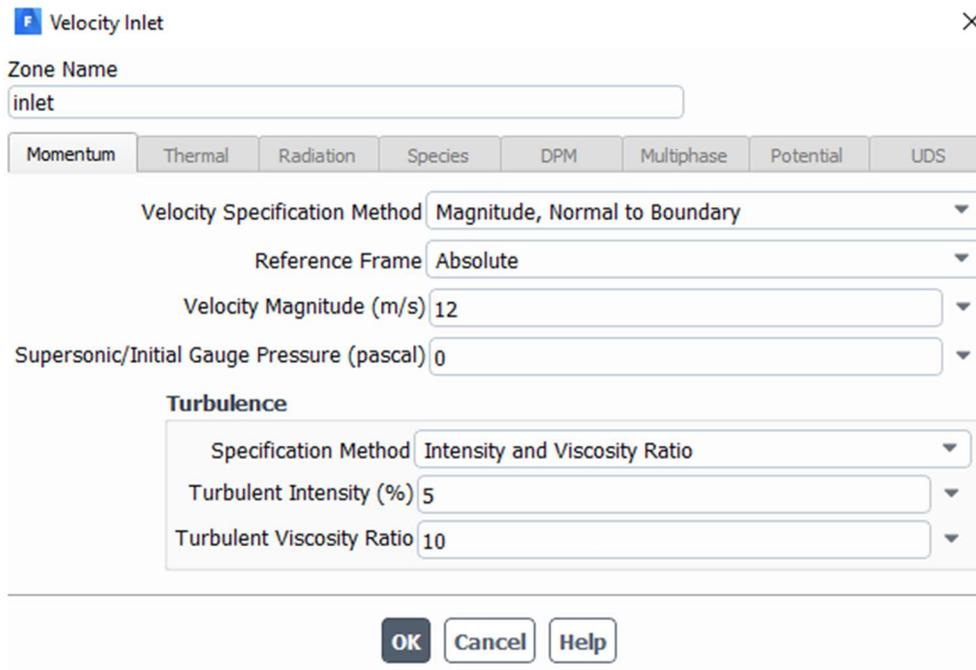


Figure 109. "Inlet" window with settings.

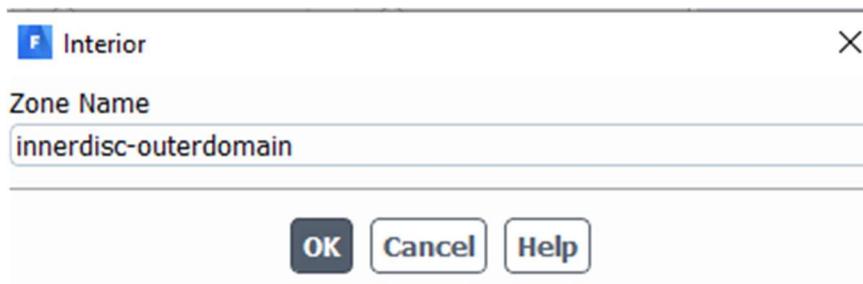


Figure 110. "Innerdisc-outerdomain" window with settings.

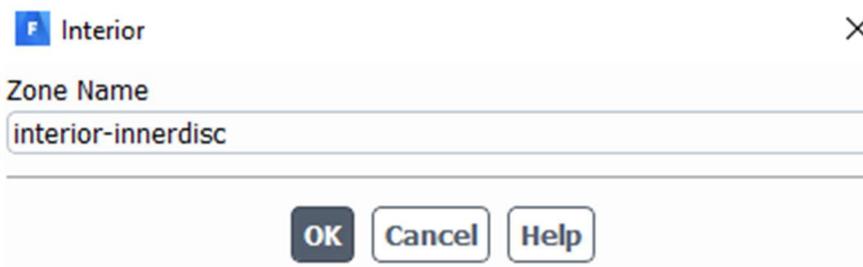


Figure 111. "Interior-innerdisc" window with settings

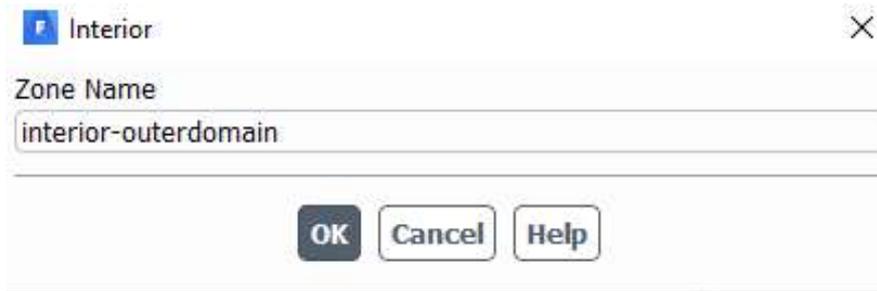


Figure 112. "Interior-outerdomain" window with settings.

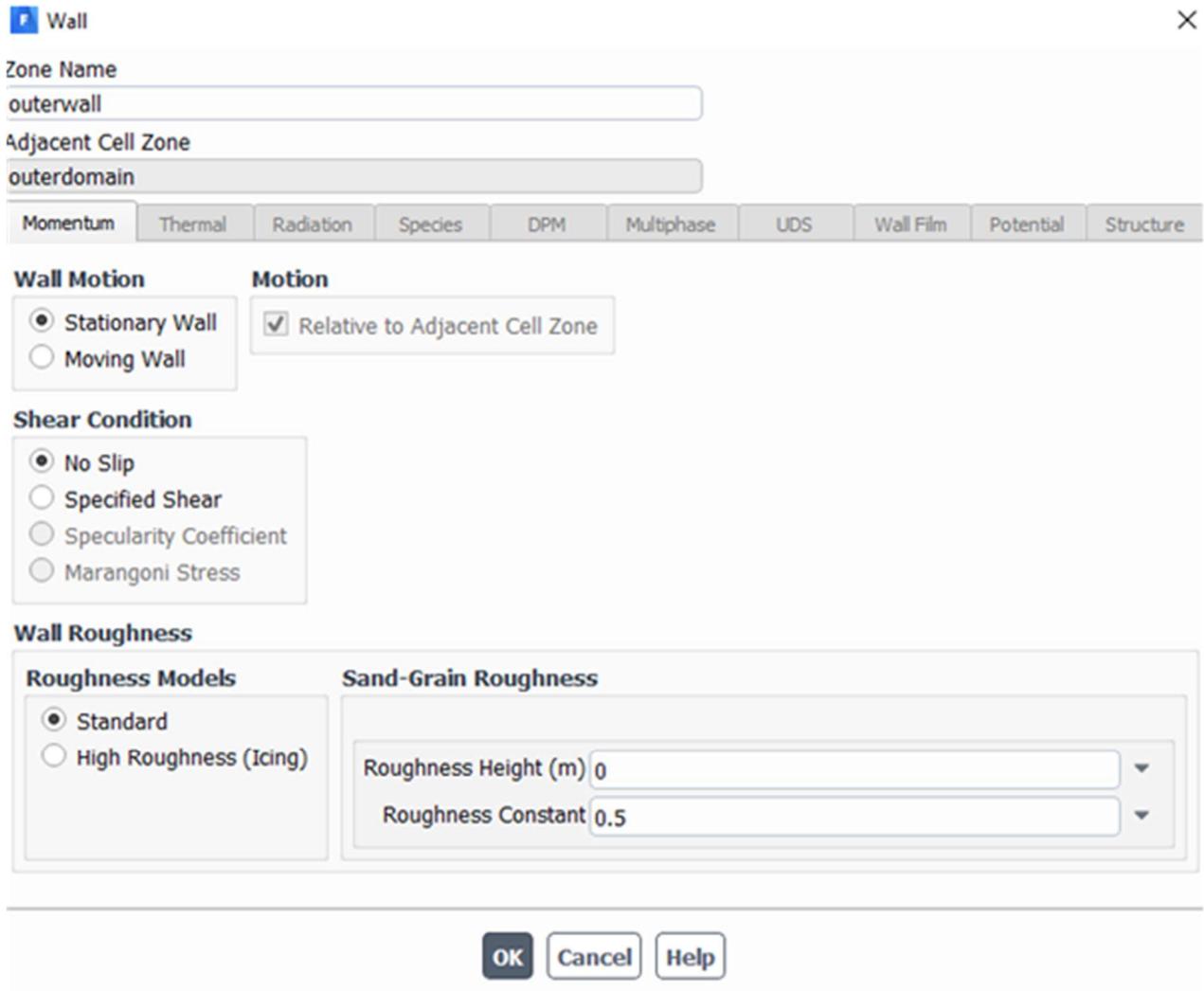


Figure 113. "Outerwall" window with settings.

**F** Pressure Outlet ×

Zone Name  
outlet

Momentum	Thermal	Radiation	Species	DPM	Multiphase	Potential	UDS
----------	---------	-----------	---------	-----	------------	-----------	-----

Backflow Reference Frame ▼ Absolute

Gauge Pressure (pascal) ▼ 0

Pressure Profile Multiplier ▼ 1

Backflow Direction Specification Method ▼ Normal to Boundary

Backflow Pressure Specification ▼ Total Pressure

Radial Equilibrium Pressure Distribution

Average Pressure Specification

Target Mass Flow Rate

**Turbulence**

Specification Method ▼ Intensity and Viscosity Ratio

Backflow Turbulent Intensity (%) ▼ 5

Backflow Turbulent Viscosity Ratio ▼ 10

Figure 114. "Outlet" window with settings.

**F** Periodic ×

Zone Name  
pie2

**Periodic Type**

Translational

Rotational

Figure 115. "Pie 2" window with settings.

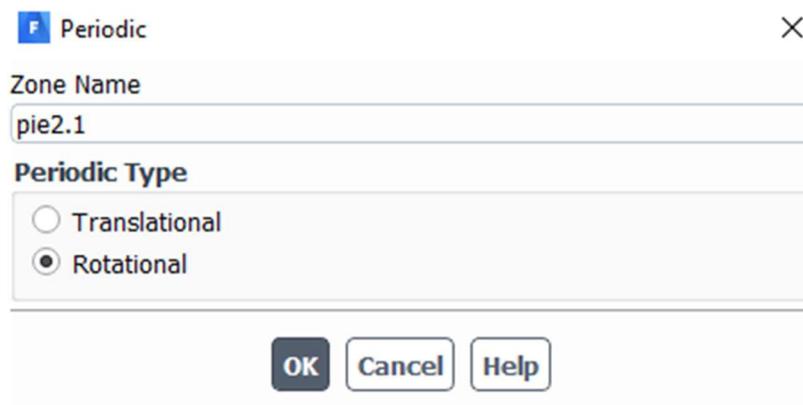


Figure 116. "Pie 1" window with settings.

The rest of the headings under setup namely ***dynamic mesh***, ***reference values*** and ***named expressions*** were not used during this simulation and were left unchanged. The next part was to adjust setting for the solution heading.

### Methods

Double click on the ***methods*** heading under ***solution*** and select the setting as shown in Figure 117 in the task page.

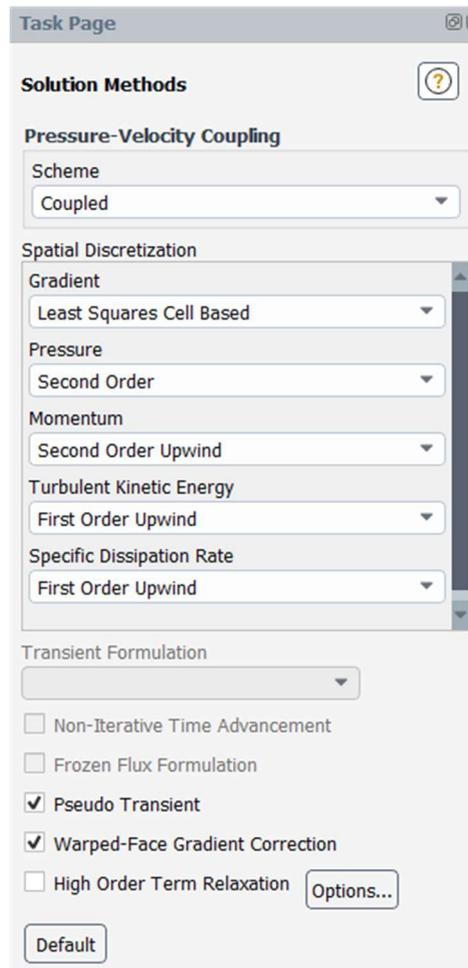


Figure 117. Methods setting in the task page.

## Initialization

Double click the **initialization** heading and choose setting as shown in Figure 118.

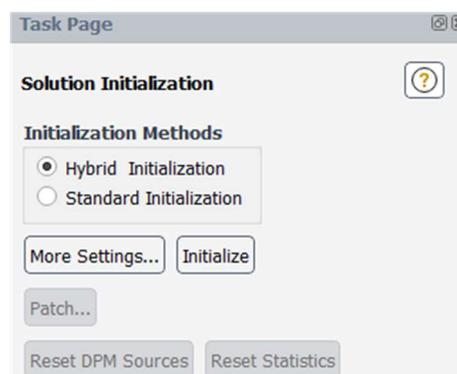


Figure 118. Initialization setting in the task page.

## Run calculation

The simulation for this research were done in stages. First double click on **run calculation** and enter the **pseudo time step** as 1 with 150 **number of iterations** and select **calculate**

within the task page. Once the calculation is complete change the **pseudo time step** to 0.1 with 200 iterations and select **calculate**. The next step is with **pseudo time step** as 0.01 with 500 iteration and the last step with 0.001 **pseudo time step** and 1000 iterations. Figure 119 shows the last **run calculation** step.

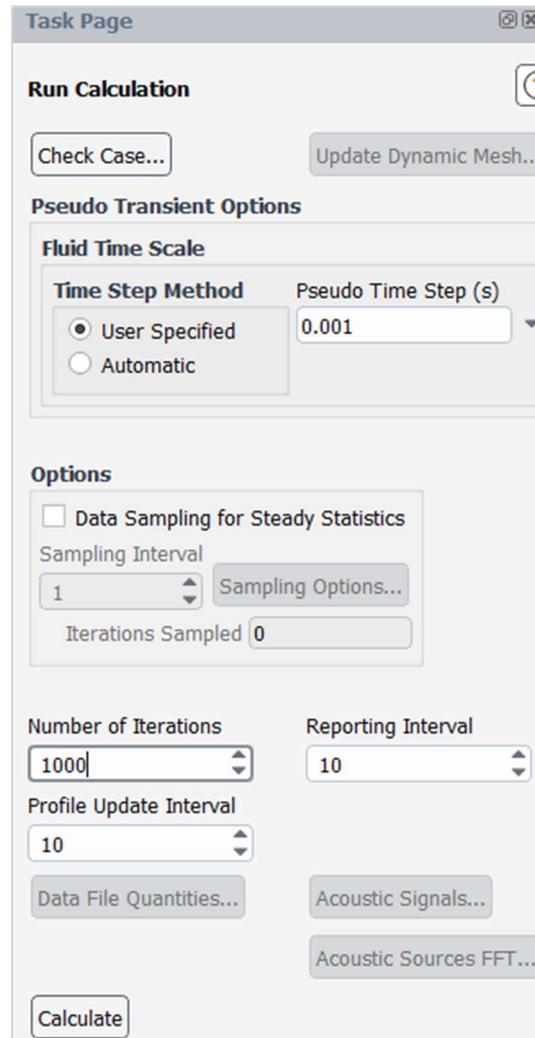


Figure 119. Run calculation last step.

Finally, when the last calculation completed select **export** and **solution data** under the **file** drop down menu. The export window should open shown in Figure 120 with settings required to be used for post CFD results visualisation. Ensure that all cell zones, surfaces and quantities are highlighted. T. file will automatically be saved as \*.cas and \*.cdat file formats. These files are used in post CFD software package.



Figure 120. Export window.